

Temperature dependence of lattice dynamics in quasicrystals

von der Fakultät für Naturwissenschaften der Technischen Universität Chemnitz

genehmigte Dissertation zur Erlangung des akademischen Grades

doctor rerum naturalium

(Dr.rer.nat)

vorgelegt von Dipl.-phys. Hamid El Hor

geboren am 16.03.1968 in Rabat/Marokko

eingereicht am 1 September 2002

Gutachter:

Prof. Dr. R. Holze,	Technischen Universität Chemnitz
Prof. Dr. J.-B. Suck,	Technischen Universität Chemnitz
Prof. Dr. H. Solbrig,	Technischen Universität Chemnitz
Prof. Dr. T. Janssen,	University of Nijmegen
Prof. Dr. K. H. Hoffmann,	Technischen Universität Chemnitz

Tag der Verteidigung: 4/2/2003

Bibliography

Hamid Elhor

Temperature dependence of lattice dynamics in quasicrystals

Technischen Universität Chemnitz, Fakultät für Naturwissenschaften, Dissertation, 2003,
79 pages, 45 figures, 6 tables, 117 references

Abstract

Die Arbeit, die in dieser Dissertation präsentiert wird, wurde durch eine Vielzahl von experimentellen Beobachtungen von Phononen in Quasikristallen motiviert. Die verallgemeinerte vibrationelle Zustandsdichte (GVDOS, generalized vibrational density of states) wurde für viele quasikristalline Phasen gemessen und für einige auch bei verschiedener Temperatur [Suck et al. (1997), Dugain et al. (1997)]. Der Fortschritt, der in der Bestimmung von Näherungen für einige Quasikristalle erreicht wurde war eine legitime Motivation für numerische Untersuchungen der Gitterdynamik auf diesen Strukturen. Es wurden zwei unterschiedliche interatomare Wechselwirkungen verwendet: Das Federmodell und die *ab-initio* Paar Potentiale. Die Untersuchungen erklärten die Form einiger experimenteller GVDOS-Messungen (d-AlNiCo, o-Al₁₃Co₄ und i-ZnMgY) mittels der Berechnung der partiellen vibrationellen Zustandsdichte. Beide, berechnete und gemessene, GVDOS der d-AlNiCo Phase zeigten einen Intensitätsanstieg bei kleinen Energien relativ zum idealen Debye Verhalten. Dieser Anstieg stellte sich als Konsequenz der Existenz von besonderen Moden bei diesen Energien heraus, die *quasi-lokalisierte Moden* genannt werden. Diese Moden scheinen charakteristisch für die Gitterdynamik in den komplexen Al-TM Strukturen zu sein. Um die experimentell beobachtete Frequenzverschiebung aufgrund der Verschiebung der GVDOS durch niedrige Energien zu berechnen, wurde eine neue, auf Monte-Carlo Simulation beruhende, Methode entwickelt. Es wurde gezeigt, daß die quasi-lokalisieren Moden große Frequenzverschiebungen bei kleinen Energien hervorrufen. Letztlich wurde auch die vibrationelle Entropie untersucht und es stellte sich heraus, daß sie bei hohen Temperaturen dazu beiträgt die komplexen Strukturen gegenüber den relativ einfachen zu stabilisieren.

Keywords

Quasicrystals, lattice dynamics, spring model, ab-initio pair potentials, GVDOS, participation-ratio, quasi-localized modes, frequency shift, gröneisen parameter, vibrational entropy.

Dank

Zuerst möchte ich mich ganz herzlich bei dem Herrn Pr. J.-B. Suck und Dr. M. Mihalcovič für ihre freundliche Unterstützung bedanken. Ohne sie wäre diese Arbeit nicht entstanden. Den Mitarbeitern unseres Labors danke ich für das angenehme Arbeitsklima während dieser dreieinhalb Jahren.

Ein ganz besonderes Dank geht an meiner Familie und vor allem an meine Mutter und meinen Vater, denen ich viel verdanke. Diese Arbeit ist meinen Nichten: Sarah, Mona, und F.Zohra, und meinem Neffe Elmahdi gewidmet.

Ich bedanke mich bei Sophie Bajart dafür, dass sie mich in diese Periode ertragen hat.

Ein ganz herzlichen Dank auch an meine Freunde: M. Djermane, A.A. Bennis, K. Tiss, A.H Bekkalli, S. Bekhechi, M. Boucadair, und S. Addioui.

Zu Allen sage ich: Tannemirt (Danke auf Amazigh)

Contents

1	Introduction	1
2	Spring model	7
2.1	Introduction	7
2.2	The harmonic approximation	7
2.3	Two-dimensional models	8
2.4	Three dimensional models	14
2.4.1	Structure	14
2.4.2	Tuning the force constants	17
2.4.3	GVDOS and partial VDOS	20
2.4.4	Local VDOS	21
2.4.5	Character of the modes	25
2.4.6	Specific heat	28
2.5	Conclusion	29
3	Atomic dynamics via realistic pair potentials	33
3.1	Introduction	33
3.2	Structural models	34
3.3	Pair Potentials	36
3.4	Stability	38
3.5	Pure Aluminum limit	38
3.6	Phonon DOS and atomic structure	39
3.6.1	Al ₃ Ni, o-Al ₁₃ Co ₄ , and Al ₉ Co ₂ Ni	39
3.6.2	Al ₅ Co ₂ , and d-ANC	39
3.6.3	Sound velocity and Deby-Waller factors	42
3.6.4	Partial Al and TM phonon DOS.	42
3.6.5	Comparison with experimental GVDOS	43
3.7	Character of the modes	45
3.7.1	The participation ratio	45
3.8	Molecular dynamics simulation	48
3.8.1	Temperature dependence of the DW factor.	48
3.8.2	High-temperature stability and atomic configurations.	49
4	Frequency shifts	53
4.1	Introduction	53
4.2	Monte Carlo approach to the reconstruction of the frequency shifts	54

4.3	Reconstruction of the VDOS and frequency shifts	56
4.4	Frequency shift and Grüneisen parameter from the experimental GDVOS	57
4.5	The Grüneisen parameter for Al_3Ni and $\text{Al}_{13}\text{Co}_4$	58
4.6	The Grüneisen parameter and the character of the modes	60
4.7	Conclusion	61
5	Vibrational entropy	63
5.1	Temperature dependence of the vibrational entropy of d-AlNiCo	63
5.2	Vibrational entropy for o-Al-13Co ₄ , Al ₉ Co ₂ Ni and Al ₃ Ni	65
5.2.1	Introduction	65
5.2.2	Energetics	66
5.2.3	Partial Al ₁₃ Co ₄ occupation	66
5.2.4	Results	66
5.3	Conclusion	68
6	Conclusion	69

Chapter 1

Introduction

What are quasicrystals ? The existence of systems without lattice periodicity showing diffraction patterns with sharp Bragg-peaks have been known for several decades. The first example were the incommensurate phases (IC), which can be described as lattice periodic structures with a periodic modulation. However, the most recently discovered quasicrystals [Shechtman et al(1984)] aroused more excitement because of the non crystallographic group of their diffraction pattern.

Quasicrystals have a well ordered structure that never exactly repeats [Levine and Steinhardt(1986)]. Mixing two or more structural objects like hexagons and pentagons, and showing rotational axes that are forbidden for periodic crystals in 3 dimensional Euclidean space.

Since the discovery of quasicrystals, much efforts have been made for understanding their physical properties. This has encouraged the discovery of many quasicrystalline phases often in the Al based alloys, and lead to a significant progress in the fabrication techniques, which allows us now a better understanding of many quasicrystal properties.

Quasicrystals can be classified depending on their structures [Tsai(1999)]: (i) Three-dimensional quasicrystals: this class contains the icosahedral phases, and exhibits the quasiperiodic order in three dimensions. (ii) Two-dimensional quasicrystals: in this class we find the decagonal, octagonal, and dodecagonal phases. These phases show the quasiperiodic order in two dimensions, while they are ordered periodically along the third direction. (iii) Finally, there are one-dimensional quasicrystals which are formed by a Fibonacci stacking of periodic layers.

Some structural principles of quasicrystals are now well understood. Both the quasiperiodic and the related periodic structures are believed to be built from the same "clusters". Slight changes in the composition will decide whether the structural units, clusters, will order periodically or quasiperiodically.

There are two ways to describe the quasiperiodic structures: (i) the tiling decoration method. (ii)the higher-dimensional approach [Janssen(1986,1988a)], and the most famous example of quasiperiodic tilings with five fold rotational symmetry is the Penrose tiling [Penrose(1974)]. It can be constructed by two types of rhombus: the *fat* rhombus (72° and 108° angles), and the *skinny* rhombus (36° and 144° angles) [Levine and Steinhardt(1986), Pavlovitch and Kleman(1987)]. The areas are in the ratio $\tau:1$ (fat:skinny) as well as the frequency of the rhombus in the tiling, with $\tau = \frac{1+\sqrt{5}}{2} = 1.6180\dots$. To force the quasiperiodicity, matching rules are needed. The Penrose tiling can be used as a quasiperiodic tiling for decagonal structures, while its three-dimensional variation with *prolate* and *oblate* rhombohedra, may serve as quasiperiodic

lattice for icosahedral structures.

On another side, in the higher-dimensional description, the principle is that quasicrystals can be seen as sections through higher dimensional periodic structures [Janssen(1986)]. For three-dimensional quasicrystals, a six-dimensional space (\mathfrak{R}^6) is necessary. The two-dimensional quasicrystals can be embedded in the \mathfrak{R}^5 , and one dimensional quasicrystals in \mathfrak{R}^4 .

A simple example to illustrate the high-dimensional approach is the one-dimensional quasiperiodic Fibonacci sequence, which can be described as a section of a two-dimensional periodic lattice

The Fibonacci sequence can be obtained by using two "units" L and S respectively for "long" and "short", and by using the substitution rules: $L \rightarrow L+S$, and $S \rightarrow L$. Starting with L, we obtain:

	L	S
L	1	0
LS	1	1
LSL	2	1
LSLLS	3	2
LSLLSLSL	5	3
LSLLSLSLLSLLS	8	5
LSLLSLSLLSLLSLSLLSLSL	13	8
	\mathcal{F}_{n+1}	\mathcal{F}_n

with:

$$\mathcal{F}_{n+1} = \mathcal{F}_n + \mathcal{F}_{n-1} \quad (1.1)$$

and,

$$\lim_{n \rightarrow \infty} \frac{\mathcal{F}_{n+1}}{\mathcal{F}_n} = \tau \quad (1.2)$$

Atomic dynamics in quasicrystals The assortment of shapes in quasicrystals structures, leads to an extra kind of excitations called phasons [Socolar et al(1986)] not found in conventional crystals. Phasons, theoretically, rearrange the quasicrystal structures by making individual atoms jumps as much as a few angstroms as the excitation passes [Edagawa and Suzuki(2000)]. Like for phonons, there is a phason elastic field and phason elastic constants. Individual uncorrelated phason jumps, contribute to the entropy and could be responsible for the stabilization of quasicrystals in the random tiling model [Henly(1991)].

Regarding phonons, the existence of acoustic modes was proven experimentally. In principle, one cannot talk about Brillouin zone for quasicrystals since there is no unit cell, but it is still possible to define pseudo Brillouin zones between strongest Bragg peaks [Niizeki (1997)]. As a consequence of the existence of linear dispersion of the acoustic modes at low energies, one would expect a Debye like behavior of the vibrational density of states at low frequencies, while at high frequencies, an infinite number of van Hove singularities is expected.

Several experiments were performed to study lattice dynamics in quasicrystals. The dispersion curves of quasicrystals were measured for single domain crystals of icosahedral and decagonal phases [Quilichini (1997)]. Well defined propagating acoustic modes were observed

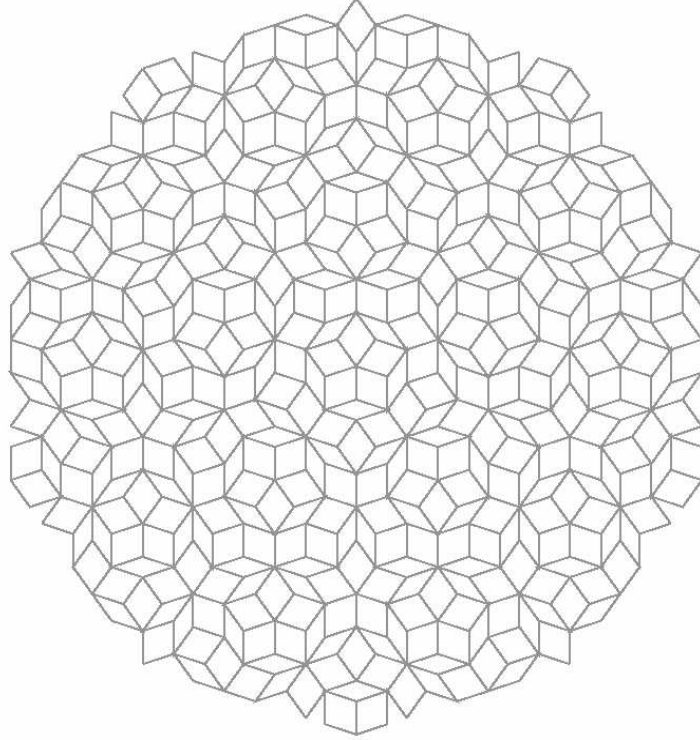


Figure 1.1: example of the Penrose tiling.

by inelastic neutron scattering (INS) close to strong Bragg peaks. For the decagonal case [Dugain et al (1999)], the anisotropy between the modes propagating in the periodic and quasiperiodic directions was found much weaker than the theoretically predicted [Hafner et al(1996)].

The generalized vibrational density of states (**GVDOS**), was measured [Suck (1993a), Mihaljovič et al (1996)] for a number of stable quasicrystals (i-AlPdMn, d-AlNiCo, d-AlCuCo, i-AlCuFe,..) by means of inelastic neutron scattering experiment (**INS**) using the time of flight method. In this method the velocity of the neutron is determined by measuring the “time of flight” of the neutron after scattering over a well known flight path.

The GVDOS is the weighted sum of the elemental partial densities of states g_α

$$G(\omega) = \sum_{\alpha} e^{-2W_{\alpha}} \frac{\sigma_{\alpha} c_{\alpha}}{M_{\alpha}} g_{\alpha}(\omega) \quad (1.3)$$

where M_{α} is the mass, σ_{α} total neutron scattering cross section, c_{α} the concentration of the element α , and $\exp(-2W_{\alpha})$ is the mean Debye-Waller factor:

$$W_{\alpha} = \frac{\hbar^2 |\mathbf{q}|^2}{2M_{\alpha}} (3N_{\alpha} N_{\mathbf{k}})^{-1} \sum_{i, \mathbf{k}} w_{i, \alpha} \frac{n(T, \omega_i(\mathbf{k})) + \frac{1}{2}}{\omega_i(\mathbf{k})} \quad (1.4)$$

where the sum is over all \mathbf{k} -points in the reciprocal space, and over all frequencies. $n(T, \omega)$ is the Bose-Einstein thermal occupation function, \mathbf{q} is a reciprocal point in the Brillouin zone, N_{α} is the total number of sites α , and $N_{\mathbf{k}}$ is the number of the \mathbf{k} -points. $\omega_{i, \alpha}$ is the total squared eigenvector amplitude on the atoms α in the i -th mode:

$$w_{i,\alpha} = \sum_{j=\alpha} u_j u_j^* \quad (1.5)$$

where u_j is the displacement vector of atom j .

This Debye–Waller factor is comparable to the isotropic “crystallographic” DW factors from the diffraction refinements:

$$B_\alpha = 16\pi^2 \frac{W_\alpha}{|\mathbf{q}|^2}, \quad (1.6)$$

where W_α denotes DW factor of the atom α .

The interest in the vibrational properties of quasicrystals has been enhanced by the availability of experimental measurements performed on single grains of stable quasicrystals. Thus a comparison between experimental and numerical results allows a significant check on the validity of the approximations introduced in the phenomenological models.

Results from inelastic neutron scattering measurements showed [Dugain et al (1997), Brand et al (2000)] a deviation from the expected Debye behavior at low frequencies. While at high frequencies, the measured generalized vibrational densities of states were smooth and featureless. This can be partly attribute to increasingly lower experimental resolution, and possibly also to the contribution of multiphonons.

The GVDOS of some stable quasicrystals (d-AlNiCo [Dugain et al (1997)], i-AlPdMn [Suck (1997)], d-AlCuCo [Dugain et al (1997)]) was measured at different temperatures. An understanding of the lattice dynamics at these temperatures may provides us with new insights in the mechanisms of stabilizations of quasicrystals. The results of these experiments show a global shift of the GVDOS to lower frequencies with increasing temperature (Fig. 1.2). This global shift preserves the main features of the GVDOS, while the energy range of the GVDOS decreases. Also an attenuation of the sound velocity was observed. These effects can be understood from the expansion of the crystals with increasing temperature.

In addition, there was recently a sensitive progress in the structure determination of the d-AlNiCo quasicrystal caused by the discovery of stable ternary phases and by the identification of closely related approximants.

The combination of these facts gives enough motivation to investigate the lattice dynamics in some quasicrystals, and this is what is intended here. The present work was motivated by the important quantity of the experimental data available on the vibrational properties of some quasicrystals, mainly in the d-AlNiCo system, and the possibility of using reliable structure models. In chapter II, the experimental GVDOS of some systems (o-Al₁₃Co₄, d-AlNiCo, i-ZnMgY) are used to construct spring models which are then used to investigate some aspect of the lattice dynamics in these systems. chapter III summarize the work reported in [Mihalkovič, Elhor and Suck(2001)] in which realistic pair potentials were used to calculate the atomic dynamics in the Al-TM alloys. In chapter IV, a novel approach is developed to determinate the frequency shift from the changing shape of the GVDOS due to the temperature. Using this method, the Grüneisen parameter was calculated as function of the frequency for d-AlNiCo at different temperatures. In the second part of this chapter, the Grüneisen parameter dependence on the character of the modes was investigated via crystalline phases with increasing structural complexity. Finally, the vibrational entropy is calculated in chapter V and the conclusion summarize the main results obtained in this work.

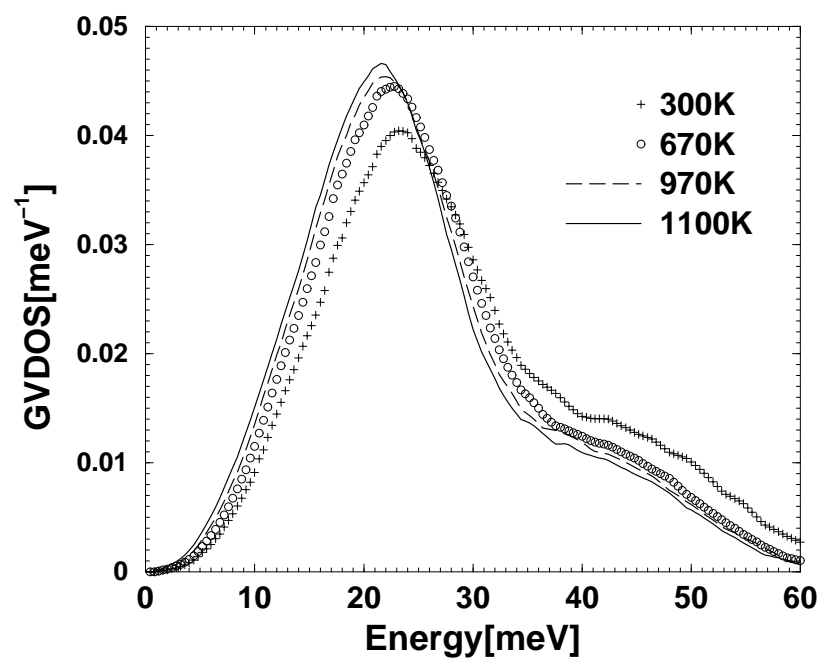


Figure 1.2: The experimental GVDOS of d-AlNiCo measured at 300K, 670K, 970K and 1100K. The GVDOS shifts to the low energies at high temperatures.

Chapter 2

Spring model

2.1 Introduction

There are still many reasons to use spring models as input for the interatomic interactions despite the availability of realistic pair potentials for Al-TM alloys [Philips et al(1994), Moriarty and Widom (1997)]. One of these reasons is the mechanical instability of some atomic models introduced by the use of the pair potentials. This instability is due to uncertain details in the atomic models, and to some extent also due to the lack of the many-body terms in the potential energy and to the shape of the Al-Al pair potential (see next chapter). The spring model does not introduce such instability since all the atoms are supposed to be in their equilibrium positions, and the forces on them to be equal to zero.

In this chapter, experimental GVDOS for o-Al₁₃Co₄, d-AlNiCo [Dugain et al(1997)] and i-ZnMgY [Rouija et al (2002)], were used to fit reliable spring models within the harmonic approximation. These spring models are then used to investigate some aspects of the lattice dynamics in the corresponding systems.

This chapter is organized as follows: first a short introduction to the basis of the harmonic approximation is given, then in § 2.3 a simple spring model is used to study the effect of the introduction of some defects in a 2D quasicrystal approximant. In § 2.4 spring models are constructed for the o-Al₁₃Co₄, d-AlNiCo, Zn₂Mg and μ -ZnMgY systems, and used to investigate in more detail the atomic dynamics in these alloys. Finally in § 2.4.6, the temperature dependence of the vibrational heat capacity is calculated for o-Al₁₃Co₄ and d-AlNiCo models.

2.2 The harmonic approximation

We consider point atomic masses M_i undergoing small amplitude displacements \mathbf{u}_i about their equilibrium positions \mathbf{r}_i . Let us suppose that the potential energy can be expanded in a Taylor series about the equilibrium position [Kittel(1986)], then

$$V(\mathbf{u}_1, \mathbf{u}_2, \mathbf{u}_3, \dots) = V_0 + V_1 + V_2 + \dots \quad (2.1)$$

where V_0, V_1, V_2 etc.. represent terms which contain the derivatives of the potential V and are constant, linear, quadratic, etc.. in the displacements. For motion about the equilibrium position, the linear term V_1 is zero since it represents the sum of all forces and we assume that

the system is in equilibrium. The first term V_0 is constant and does not affect the calculation. If we retain the first term of the remaining part, then

$$V \approx V_2 = \frac{1}{2} \sum_{i,j=1}^N \sum_{\alpha,\beta=1}^3 C_{ij,\alpha\beta} u_{i,\alpha} u_{j,\beta} \quad (2.2)$$

The $C_{ij,\alpha\beta}$ are the second derivative of the potential V given by:

$$C_{ij,\alpha\beta} = \left(\frac{d^2 V}{du_{i,\alpha} du_{j,\beta}} \right) \quad (2.3)$$

Where i and j are labels for atoms, α and β design the Cartesian coordinates of u . The harmonic approximation consist in a truncation of the potential as above. This holds as long as all u 's are small.

Having the potential of the system, one can write the Tylor expansion of the equations of motion for lattice vibrations:

$$\omega^2(\mathbf{k}) u_{j\alpha} = \sum_{j'\alpha'} \frac{u_{j'\alpha'}}{\sqrt{M_j M_{j'}}} \sum_{\mathbf{e}} e^{-i\mathbf{k}\cdot\mathbf{e}} \frac{\partial^2 V_2}{\partial u_{j\alpha} \partial u_{j'\alpha'}}, \quad (2.4)$$

where ω is the frequency, $u_{j\alpha}$ is the α -th component of the displacement and M_j is the mass of an atom j , and N is the number of atoms by unit cell. The second summation is over the translation vectors \mathbf{e} to include the contributions from all atoms within an interaction radius, for a wave vector \mathbf{k} within the first Brillouin zone.

The solution of these equations gives the eigenfrequencies and eigenvectors of the lattice vibrations.

For quasicrystals, it is clear that this approach is useful only if the infinitely extended quasicrystal is replaced by a finite system. In this work we choose the approximant to quasicrystals with periodic boundary conditions. In this case N is the number of atoms of the whole system.

We solve the standard eigenvalue problem represented by Eq. 2.4 using LAPACK library routine ZHEEV for a mesh of \mathbf{k} -points inside the first Brillouin zone, to obtain $3N$ real eigenvalues $\omega_i^2(\mathbf{k})$ (these are positive for stable structures) and for each of these the corresponding normalized eigenvectors $\mathbf{u}_{ij}(\mathbf{k})$ with three complex components for an atom j . The phonon DOS may then be evaluated for any subset of sites α in the structure from the statistics of eigenfrequencies:

$$g_\alpha(\omega) = \frac{1}{3N_\alpha N_{\mathbf{k}}} \sum_{i=\alpha, \mathbf{k}} w_i \delta(\omega_i(\mathbf{k}) - \omega) \quad (2.5)$$

where $w_i = \sum_{j=\alpha} \mathbf{u}_{ij} \mathbf{u}_{ij}^*$ is the total squared eigenvector amplitude on the atoms α in the i -th mode, N_α is the total number of sites α per unit cell, $N_{\mathbf{k}}$ the number of \mathbf{k} -points and δ denotes a resolution function; our choice was to use a Gaussian $(\sigma\sqrt{2\pi})^{-1} \exp(-\frac{1}{2}(\frac{\omega_i(\mathbf{k})-\omega}{\sigma})^2)$,

2.3 Two-dimensional models

Previous studies of two dimensional quasicrystal models (see for example: [Odagaki and Nguyen(1986), Janssen(1988b), Ashraff et al(1990), Los et al(1993a), Liu et al(1992)]) showed that the phonon density of states is almost linear at low frequency indicating a Debye behavior for a 2D system.

These studies highlighted also the spiky character of the DOS, which was suggested to be due to the quasiperiodic order [Janssen(1989)]. Los et al [Los et al(1993a)] showed however that when an octagonal tiling was randomized by allowing a number of phasons jumps, most of the structured character of the DOS disappear. Here we choose to study two simple 2D quasicrystal models. We first generate a *rectangle-triangle* (**RT**) tiling by optimizing a decagonal disc packing in a Penrose tiling. This is achieved by observing few rules: First we put the skinny-rhombi together only in even chains (a chain is made up of skinny rhombi, every two of them sharing one edge). Then we remove the short diagonal distance of the skinny rhombus by removing half of the vertices in each chain. The reason of having even chains in a RT tiling is that for these chains one can optimally pair few skinny rhombi, and have a well packed structure. For odd chains one always has an extra skinny rhombus, which is a *defect volume*. There are two dominant distances in this model: the edge-length of the equilateral triangle, and the longer diagonal of the skinny rhombus. In the first model, all the vertices of the RT tiling are decorated by atoms, while in the second model, pairs of defects are created at the ends of some chains as we can see in Fig. 2.1.

We connected the next neighbors by springs with the same force constants in the two cases. Then we diagonalize the dynamical matrix on a mesh of points in the Brillouin zone. By direct diagonalization of the dynamical matrix we obtained the eigenvalues and the eigenvectors from which we calculated the vibrational density of states (**VDOS**) via Eq. 2.5 and using $\sigma \sim 0.02$ for the Gaussian convolution.

The calculated VDOS of the two models are shown in Fig. 2.2. The Two VDOS are highly structured. For the RT model, there is a *pseudo gap* at 17–20 a.u while for the defect model there are more *pseudo gaps*, and particularly the gap at 22–23 a.u. At low frequencies, the RT VDOS is perfectly linear, and we can fit an exponent $\epsilon \sim 0.06$ and $v_s \sim 0.03$ for ω up to ~ 2.35 a.u in the formula:

$$g(\omega) = v_s \cdot \omega^{(1+\epsilon)} \quad (2.6)$$

where ω is the frequency, g is the VDOS and v_s is the mean sound velocity defined by:

$$\frac{2}{v_s} = \frac{1}{v_t} + \frac{1}{v_l} \quad (2.7)$$

Where v_t and v_l are respectively the transverse and longitudinal sound velocities.

For the defect model there is an excess VDOS at low frequencies. In fact the defect model VDOS is only “linear” up to ~ 1.5 with $\epsilon \sim -0.07$ and $v_s \sim 0.04$. Above this energy, the VDOS increases significantly as shown in Fig. 2.2, but it is surprising that this excess seems to be rather smooth.

In Fig. 2.3 we show the *participation ratio* for the two models. The participation ratio p_i for a mode i can be defined by:

$$P_i = \frac{(\sum_j |\mathbf{u}_{ij}|^2)^2}{N_{at} \sum_j (|\mathbf{u}_{ij}|^2)^2} \quad (2.8)$$

where the index j runs through N_{at} atoms, and \mathbf{u} is the displacement vector. The *participation ratio* distinguishes between modes on the basis of the participation of the atoms in the vibration. When all atoms participate with equal amplitudes in a vibration, the mode is extended and $P \sim 1$. But when only few atoms participate in a vibration, which is for example the case when

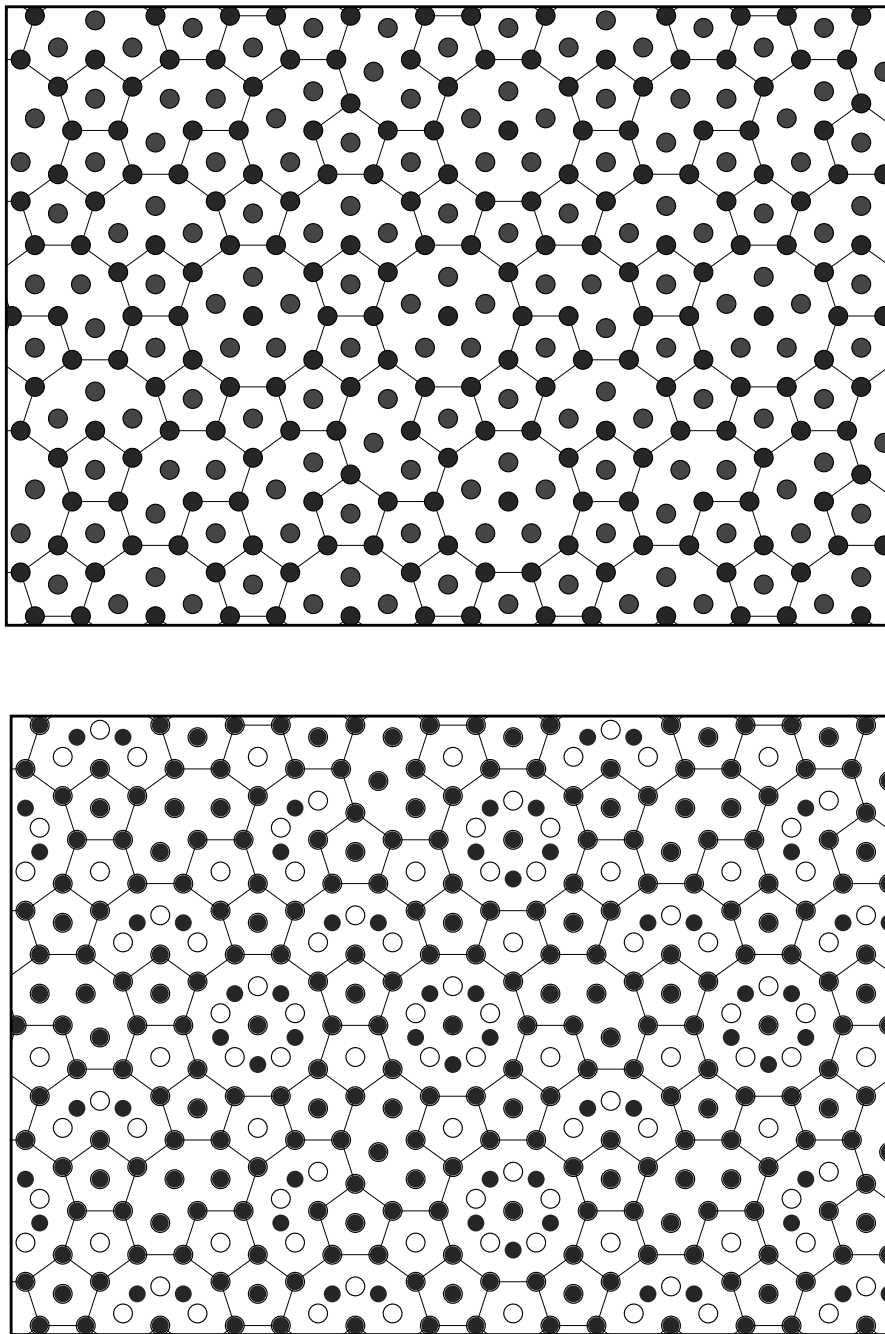


Figure 2.1: (up):The rectangle-triangle (RT) model, a RT tiling decorated by atoms of the same type on all the vertices. (down): The defect model consisting on RT tiling in which some vacancies defects were introduced (black circles show atoms).

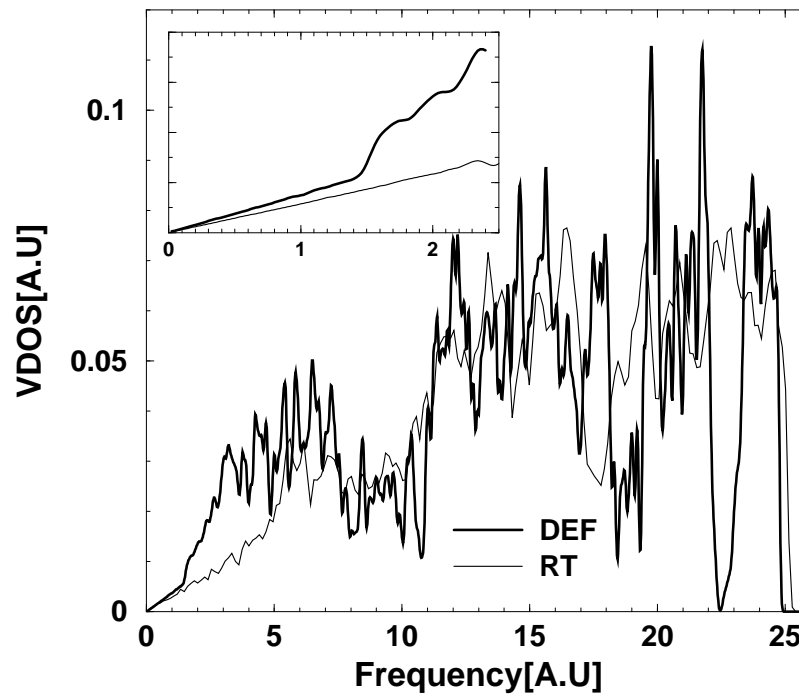


Figure 2.2: The VDOS of the two models: the two VDOS show a band like structure, with a gap for the defect model GVDOS at ~ 22 – 23 a.u. There is an extra intensity in the VDOS for the defect model at low frequencies (window at the top left).

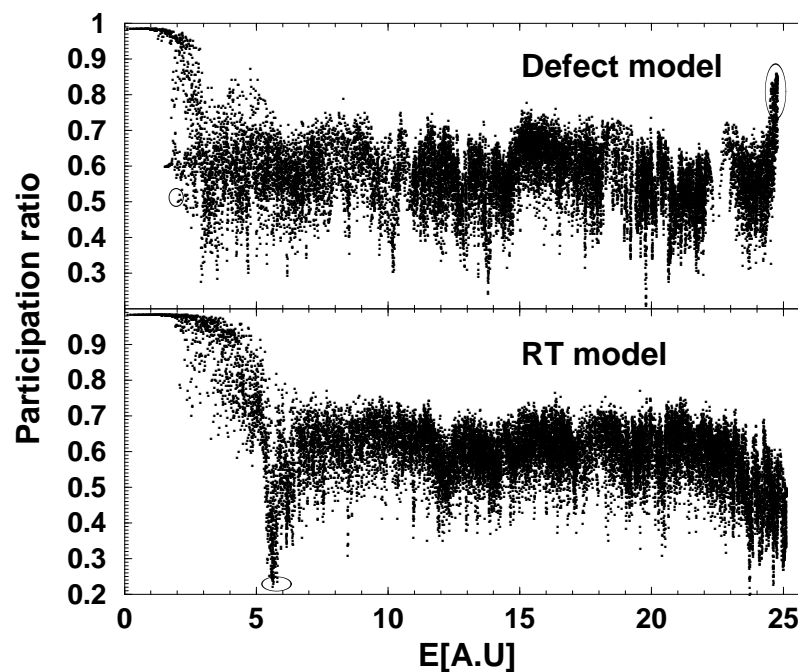


Figure 2.3: The participation ratio of the two models, there are modes with low participation ratio at low energies for the defect model, while we find for this model a group of extended modes at high energy not present for the RT model.

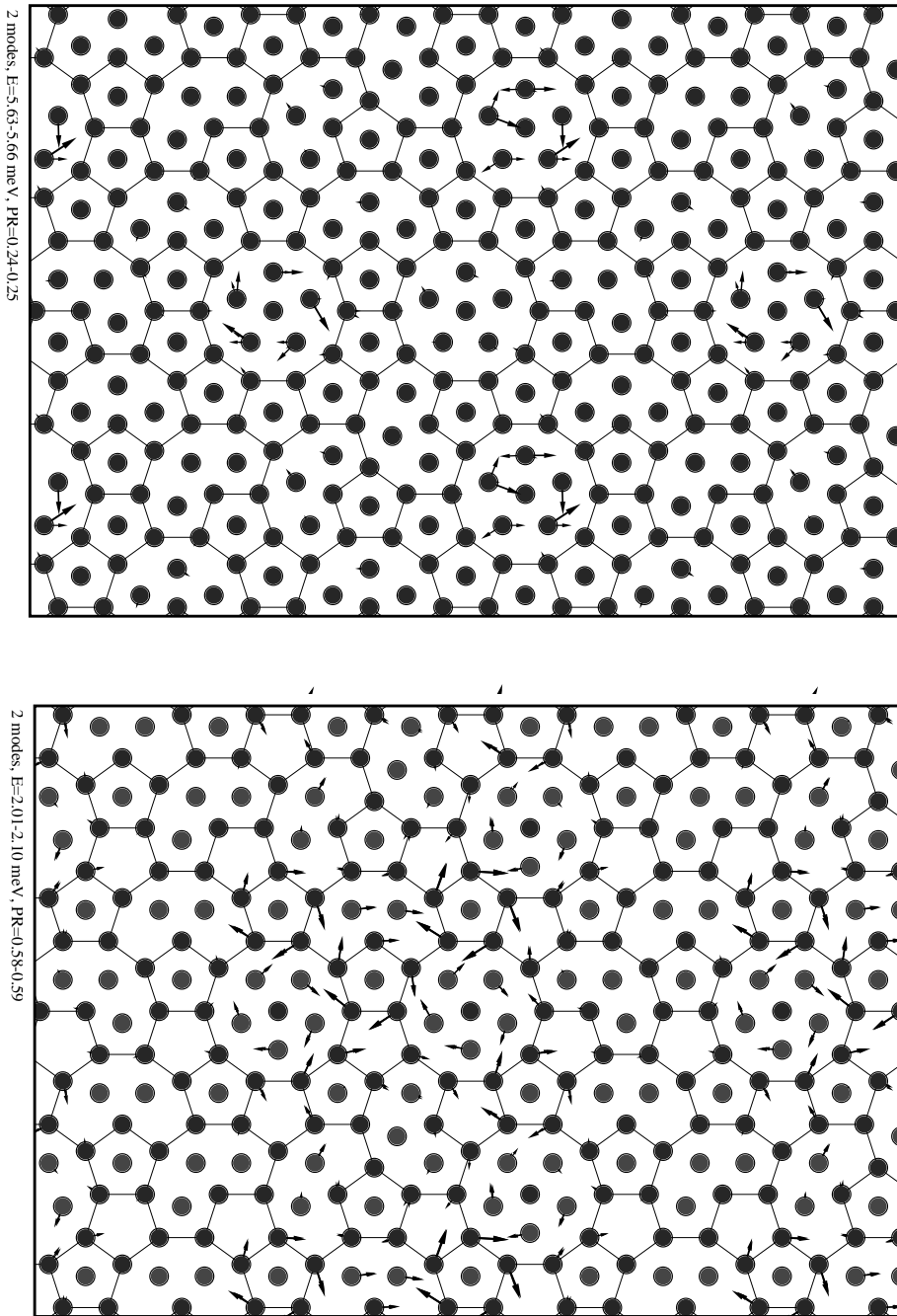


Figure 2.4: top: two low energy modes for the RT model with $E \approx 5.63$ a.u and participation ratio $\approx 0.24-0.24$. Notice the rotations of the pentagons at the center of the decagons (the arrows show eigenvectors). bottom: Low energy mode ($E \approx 2.01$ a.u and the participation ratio ≈ 0.585) for the defect model. The atoms around the empty spaces introduced by the defects tend to fill these spaces. Notice the tendency to rotate the pentagons

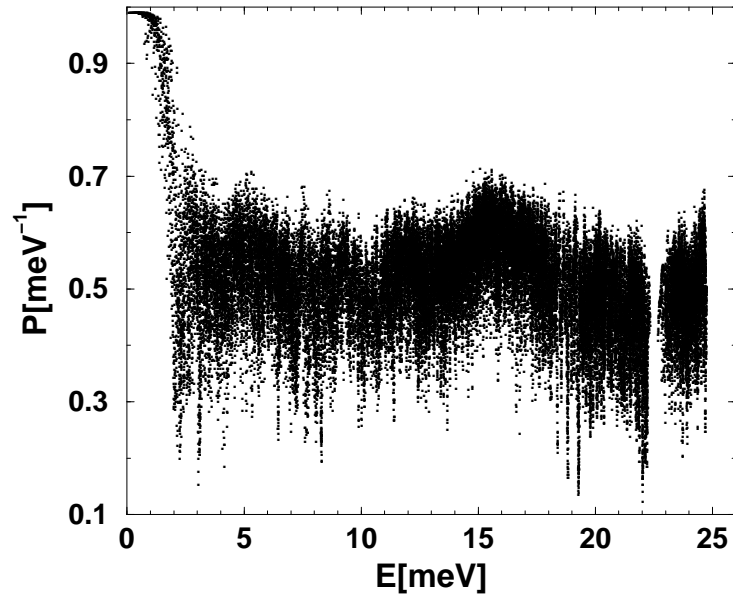


Figure 2.5: The participation ratio of bigger approximant for the defect model. The participation of the extended modes at high energy observed in Fig. 2.3 decreases.

some defects are introduced in a crystal, the modes are localized or quasi-localized and $P \sim (N_{at})^{-1} \sim 0$. At very low frequency (up to ~ 1.45 a.u for the defect model and 2.35 a.u for the RT model), the participation ratio is ~ 1.0 . This behavior is characteristic for the extended modes. This region of frequency coincides with the regions where the DOS is almost linear for the two models which is due to the acoustic modes. There is, however, a group of modes of the defect model at low frequencies (~ 2 a.u) with low participation ratio indicating some *localization* at these frequencies. While for the RT model, a similar group of modes appears at higher frequencies (~ 5 a.u). The plot of the displacement vectors shows (Fig. 2.4) that these vibrations correspond to bending of the pentagons in the center of the decagons. The low energy modes with low participation ratio for the defect model are due to vibrations of atoms around the empty spaces introduced by the defects (Fig. 2.1). At high frequencies, there is a significant distinction between the two participations ratios. While there are localized modes for the RT model at energies > 23 a.u, a group of modes at the same energy range tend to be more extended for the defect model with participation ratio > 0.8 . It is surprising to find such modes at high energy, since these are extended modes which cost a lot of energy. To check the scaling properties of these modes, a calculation was performed with a defect model with more atoms per unit cell (288 atoms). Fig. 2.5 shows that the participation ratio of these modes decreases as the size of the approximant increases, indicating that this phenomenon can be due to a size effect.

Finally in Fig. 2.6 we compare the distributions of the participation ratio ($\mathbf{g}(\mathbf{P})$) of the two models. This distribution has a sharp maximum for the RT model at $P \approx 0.65$, and a wide maximum for the defect model at P between 0.60 and 0.65. This figure shows that the defect model has globally slightly more localized modes.

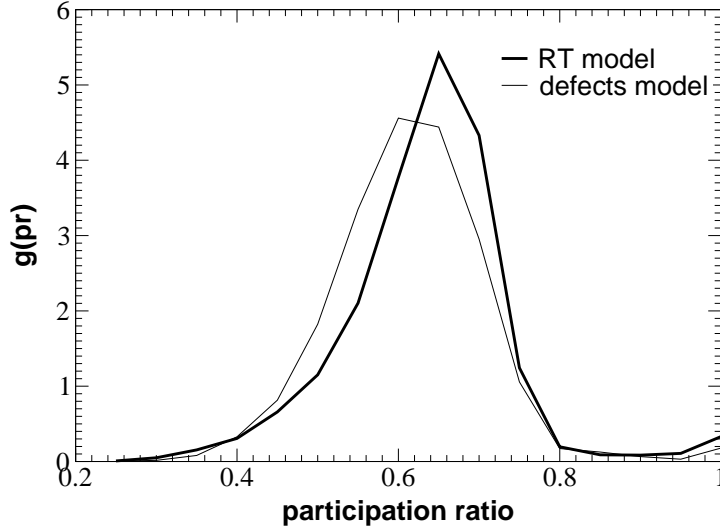


Figure 2.6: The distribution of the participation ratio: there are more localized modes for the RT model, this is due to the high frequency localized modes.

2.4 Three dimensional models

In this section we study four different structures: The orthorhombic $\text{Al}_{13}\text{Co}_4$ phase, the decagonal AlNiCo phase (d-ANC), the μ phase in ZnMgY , and the MgZn_2 -Laves phase.

2.4.1 Structure

Orthorhombic $\text{Al}_{13}\text{Co}_4$ phase

Many complex phases exist in a small range of composition in the $\text{Al}_{1-x}\text{Co}_x$ system for $0.23 \leq x \leq 0.29$. Most of these phases share some of their structural properties, for example the stacking periodicity along the pseudodecagonal axis. Along this axis the o- $\text{Al}_{13}\text{Co}_4$ structure can be described by an arrangements of atoms in a sequence of flat (F) and puckered (P) layers, separated by $\sim 0.2\text{nm}$. The flat layers are also mirror plans. The sequence is FPF'F.... The P' layers are different from the P layers only by the sign of puckering displacement.

We find in the $\text{Al}_{13}\text{Co}_4$ structure structural units consisting of $\text{Al}_{16}\text{Co}_7$ bipyramidal pentagons (PB) (Fig.2.7(right)). The PB occupies 3 layers along the stacking axis. A pentagon with Co atoms and an edge length of 0.47nm and centered by an Al atom forms the equator of the PB which lies in a flat layer. Along the stacking axis, two PB's are joined in a flat layer F'. The presence of short Al-Al bonds in o- $\text{Al}_{13}\text{Co}_4$ and energetic considerations suggest that some of Al sites might not be occupied.

Decagonal $\text{Al}_{70}(\text{NiCo})_{30}$

Our understanding of the decagonal phases has been advanced by the discovery of ternary stable decagonal quasicrystals, and the identification through high resolution electron microscopy (HREM) of closely related approximants [Ranganathan and Chattopadhyay (1989), Idziak and Heiney (1990)].

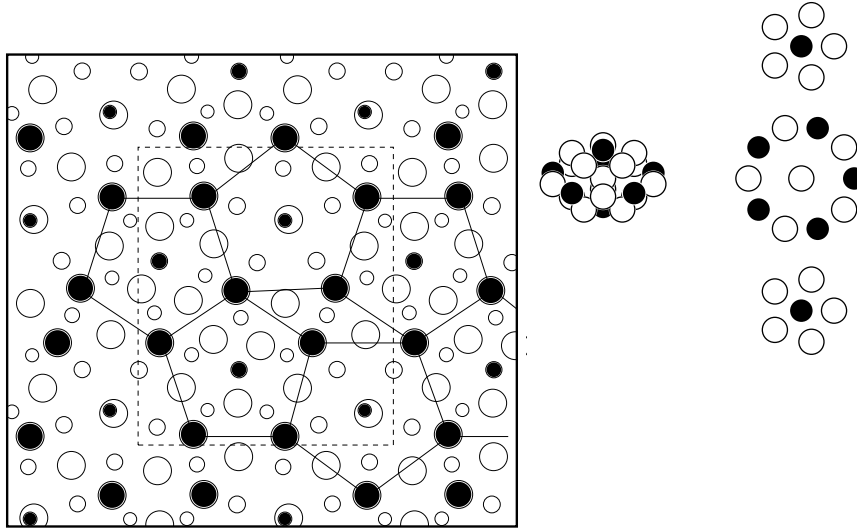


Figure 2.7: (*left*): Structure model for $\text{Al}_{13}\text{Co}_4$, projection on the XY plan with two layers (small circles present the atoms on the lower layer) separated by $\sim 0.4\text{nm}$. (*right*): Pentagonal bipyramidal cluster containing 16 aluminium and 7 Co atoms.

For Al-transition metal (Al-TM) decagonal phases, there appear to be well defined layers in the 10-fold direction with spacing $\sim 0.205\text{ nm}$, while there are different stacking “periods”: 0.4 nm (d-AlNiCo: [Yamamoto et al (1990)] d-AlCuCo: [Steurer and Kuo (1990)]); 0.8 nm (d-AlCo: [Tendeloo et al (1989), He et al (1988)]; d-AlNi: [Li and Kuo (1988)]); 1.2 nm (d-AlMn: [Steurer (1991), Li and Kuo (1991)]; d-AlPdMn: [Beeli et al (1991)]); and 1.6 nm (d-AlPd: [Rabson et al (1991), Yamamoto and Isihara (1988)], and d-AlCuFe: [Ebalard and Spaepen (1990)]). Most of the current models are built using atomic “clusters” with local 10-fold screw symmetry axes.

The HRTEM images of decagonal quasicrystal near $\text{Al}_{70}(\text{CoNi})_{30}$ are characterized by a clear decagonal ring of $\sim 2\text{nm}$ diameter. A corresponding model is the columnar cluster shown in Fig. 2.8a. This model was first proposed by Steurer et al on the basis of an earlier diffraction refinement study [Steurer et al (1993)]. The numbers in the figure label symmetry inequivalent sites. Light-gray circles represent Al, filled circles TM atoms. The size of the circles scales with the z -coordinate perpendicularly to the plane: there are two layers of atoms related by a 10-fold screw symmetry operation. The columnar cluster is built by a translational symmetry operation along the “periodic” z axis, with the $c=0.408\text{ nm}$ period. We adopt a structural model for the quasicrystal approximant, in which the columnar clusters decorate vertices of the tiling of golden rhombi (a golden rhombus is a rhombus the ratio of whose two diagonals is the golden number $\tau = (1 + \sqrt{5})/2$) with acute angles of $\gamma=72^\circ$ and an edge length of $a=1.98\text{ nm}$, in a manner similar to the model proposed by Hiraga et al in [Hiraga et al (1991,1994), Edagawa et al (1992)] on the basis of the HRTEM images as shown in Fig. 2.8b. The choice

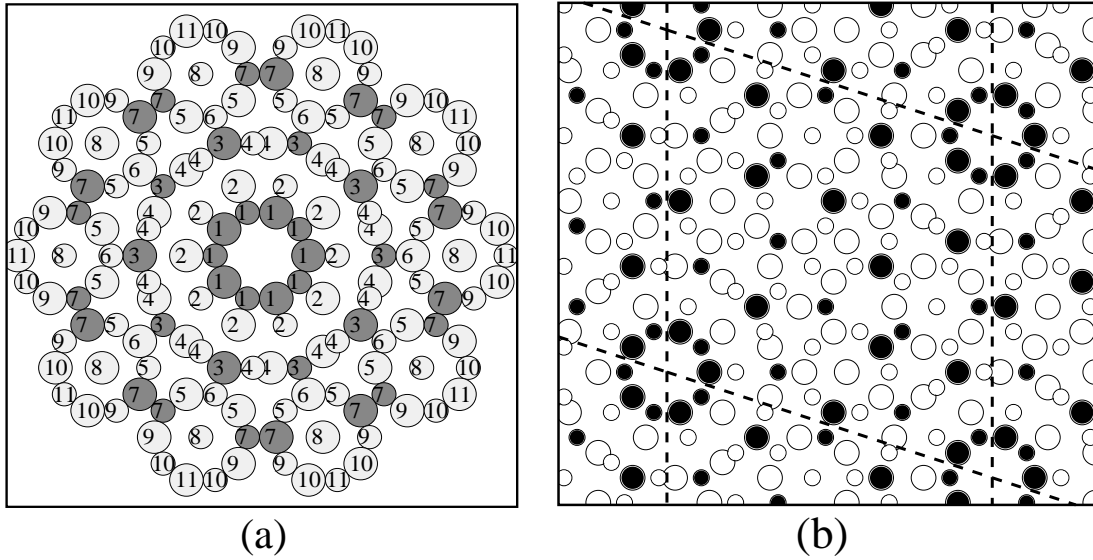


Figure 2.8: Left: model for the 2 nm diameter columnar cluster. The labels design the Wyckoff cites, there are 3 TM inequivalent positions, and 8 Al inequivalent positions. Right: a structural model for the d-AlNiCo phase, this model was produced by decorating the vertices of a golden rhombi with acute angles of $\gamma=72^\circ$ and an edge length of $a=198,0\text{nm}$, by columnar clusters.

of this geometrical arrangement of the columnar clusters was motivated by the requirement of simplicity.

The atomic positions generated by the above decoration rule *cover* all the sites actually occupied by the atoms. There are few short-distance conflicts between the atoms in the outer shell of the cluster; one simple way to resolve these conflicts is to remove symmetrically one of the atoms which has a neighbor at short distance (Fig. 2.8).

μ -ZnMgY and MgZn₂-Laves

The Zn-Mg-RE (RE=Gd, Tb, Dy, Ho, Er and Y) quasicrystals form a new type of quasicrystals. Their discovery [Ohashi and Spaepen (1987), Niikura et al (1994)] raised great interest because these alloys indicate a new combination of elements without Al and transition metals. Zn-Mg-RE icosahedral phases belong to the Frank-Kasper type of icosahedral crystals, which is characterized by the Bergman cluster formed by dense packing of tetrahedra, relating it to Frank-Kasper phases.

No convincing model has been provided up to now for these quasicrystals. In this case, the investigation of the crystalline phases with similar chemical composition as that of the corresponding quasicrystals can be of great help in the study of the structure and the properties of these quasicrystals. In this section, we use the hexagonal phase μ -MgZnRE [Sugiyama et al (1998), Abe et al (1999a)] as a model to investigate the lattice dynamics, assuming that the results concerning lattice dynamics for the quasicrystals will be similar to some extent, since the phonon spectra are dominated by the short range order [Abe and Tsai (1999b)]. We use

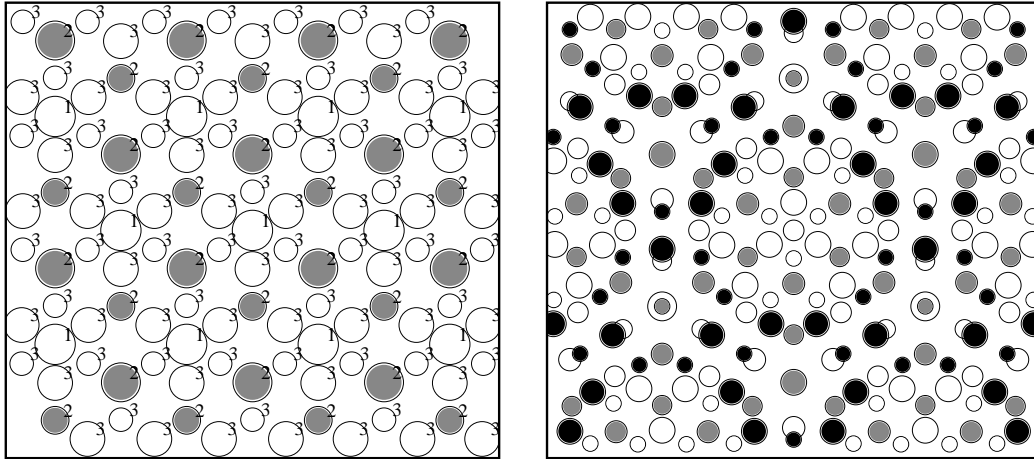


Figure 2.9: The c-axis projection of the structure of (*left*) Zn_2Mg -Laves structure and (*right*) structure model for the $i\text{-ZnMgY}$, open circles indicate Zn, gray ones indicate Mg, and black ones indicate Y. The difference of the circle size indicates different positions on the c-axis. The numbers on the figure of the Zn_2Mg -Laves structure indicate the the Wyckoff positions.

also the cubic phase MgZn_2 -Laves [Sugiyama et al (1998)] for a comparison.

Along the hexagonal c-axis of the $\mu\text{-ZnMgRE}$ structure, the coordination polyhedra around the Zn(7) sites are described as icosahedra with 12 neighbors (one such icosahedron can be seen at the center of Fig.2.9(*right*)). Only these icosahedra are found in the MgZn_2 -Laves phase ($P6_3/mmc$, $a=0.5223\text{nm}$, $c=0.8566\text{nm}$) together with the similar values for the lattice constant of the hexagonal c-axis. In addition, in the μ phase there is another type of icosahedron around Zn(2). In these icosahedra there are 6 Zn, 4 Mg and two RE atoms. Mg and RE sites are surrounded by more than 13 neighbors, and the Mg(10) site shows a weakly distorted Friauf polyhedron [Samson (1958)]. At the origin of the unit cell we find 7 connected icosahedra, there are 6 Zn(2) icosahedra connected to one Zn(7) icosahedron. The same connection is found in MgZn_2 -Laves phases, but there all the icosahedra are of Zn(7) type. There is another highly distorted type of icosahedron around Zn(6) created by the localized distribution of the large RE atoms existing in the center of 6 Zn(2) type icosahedra.

2.4.2 Tuning the force constants

As we have seen before (§2.1), the potential can be expressed in the harmonic approximation by Eq.2.2. To construct a spring model, we have to evaluate the force constants.

We start by giving arbitrary values to the force constants depending on the interaction type (between different chemical elements) and depending on the distance between atoms. The GVDOS is then calculated using the direct diagonalization of the dynamical matrix as explained in §2.1. By tuning the force constants we improve the fit of the experimental GVDOS. In this work, we tune these force constants in a way to have a convincing agreement between the theoretical GVDOS (calculated using the spring model), and the experimentally measured GVDOS. The improvement of the fit with variable parameters of the two GVDOS is achieved by trial and error by varying 36 parameters for ZnMgY model, 9 parameters for $o\text{-Al}_{13}\text{Co}_4$ model and 12 parameters for both $d\text{-AlNiCo}$ and MgZn_2 -Laves models.

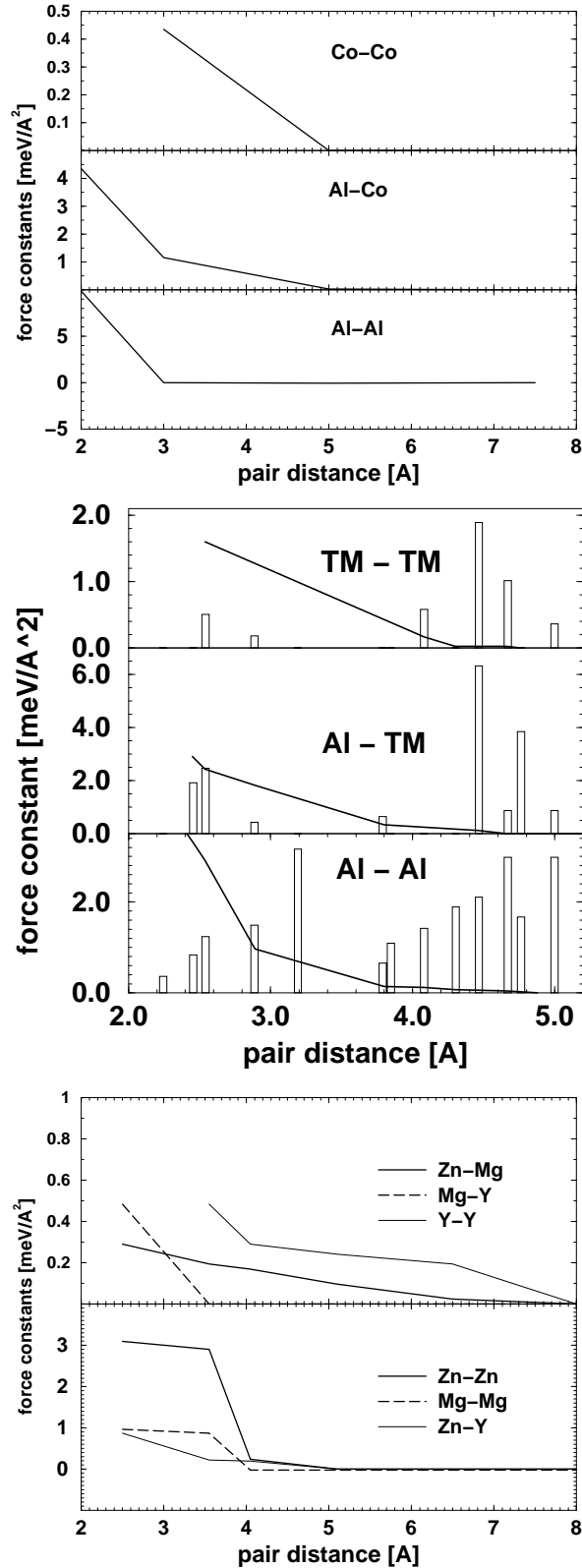


Figure 2.10: top: o-Al₁₃Co₄ spring model: the interaction Co-Co is not important in this model (notice the small values for the Co-Co force constants) this is mainly due to the small number of the Co-Co first neighbors. For Al-Al and Al-Co interactions, the force constants have higher values but vanish rapidly, especially for Al-Al where the force constants have non zero values only up to 0.3 nm. middle: d-AlNiCo spring model: like for the Al₁₃Co₄ case, the Al-Al and Al-TM force constants vanish rapidly, the particularity for the d-ANC spring model is the high TM-TM force constants. For this structure, there are more TM-TM first neighbors than the Co-Co neighbors in the o-Al₁₃Co₄ structure. bottom: ZnMgY spring model: The Zn-Zn interactions dominate up to ~ 0.4 nm, while the much weaker Y-Y interaction do not vanish up to ~ 0.8 nm

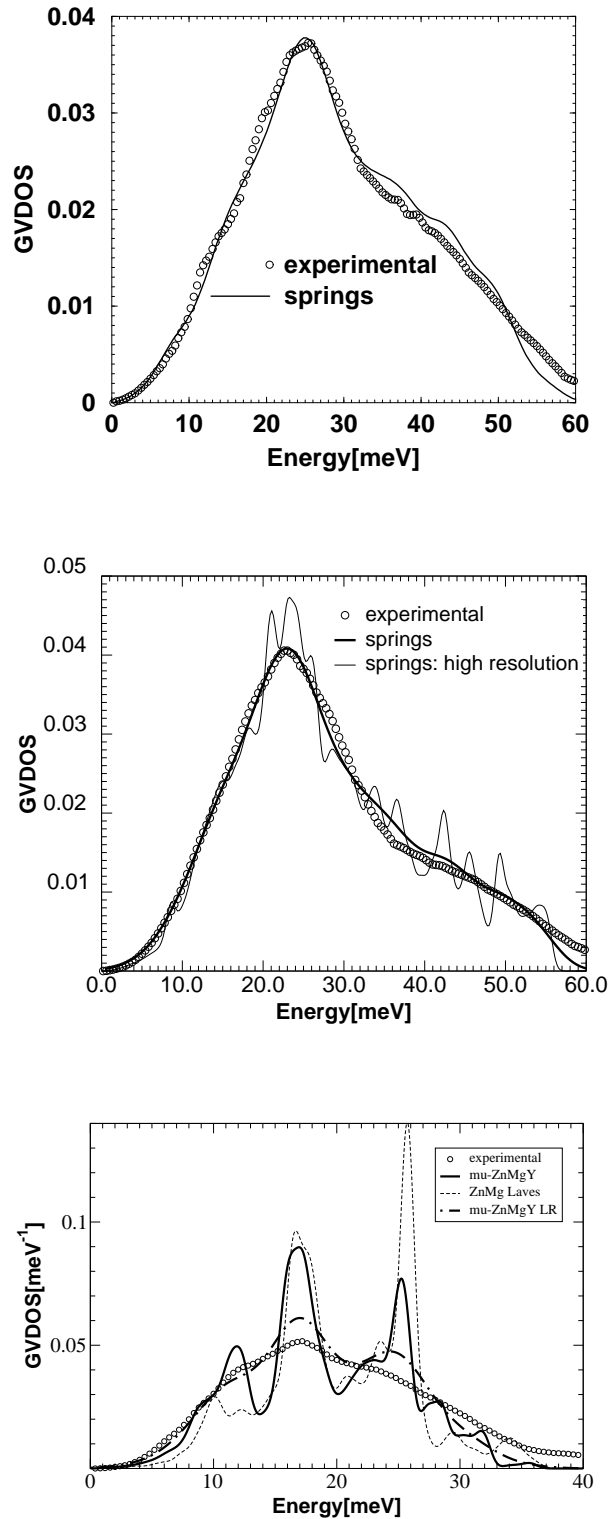


Figure 2.11: top: the experimental and calculated GVDOS of $\alpha\text{-Al}_{13}\text{Co}_4$. The experimental GVDOS is characterized by the maximum at $\hbar\omega \sim 25$ meV, and a broad band up to 60 meV. middle: the calculated GVDOS of $d\text{-AlNiCo}$ (with two different resolutions), compared to the experimental one. There are two main features: a peak at ~ 23 meV, and a broad band up to 60 meV. bottom: the experimental GVDOS of the $i\text{-ZnMgY}$ phase up to 40 meV, together with the calculated GVDOS for $\mu\text{-ZnMgY}$ phase with a high and a low resolutions (LR)

Two main factors control the energy range and the shape of the GVDOS: (i) the mass of elements, and (ii) the strength of the forces on atoms. Atoms with low masses move faster and participate in general to modes with higher frequencies. Heavy atoms move in general slower and not too far from their equilibrium positions. So we expect that the partial VDOS of light atoms will be found at higher frequencies, while the partial VDOS of heavy atoms will be found at lower frequencies. Likewise, strong forces on atoms give rise to a shift of the partial DOS to higher frequencies.

For o-Al₁₃Co₄ and d-ANC we use three types of interactions : Al-Al, Al-TM, and TM-TM, with TM=Co in o-Al₁₃Co₄ and a mixture of Co and Ni in d-ANC. For μ -ZnMgY we use six types of interactions: Zn-Zn, Zn-Mg, Zn-Y, Mg-Mg, Mg-Y, and Y-Y. And again we use three types of interactions for MgZn₂-Laves: Zn-Zn, Zn-Mg, and Mg-Mg. We allow the atoms to interact with neighbors within a radius of 0.5nm for o-Al₁₃Co₄ and d-ANC, and a radius of 0.8 nm for μ -ZnMgY and MgZn₂-Laves.

2.4.3 GVDOS and partial VDOS

The experimental GVDOS of o-Al₁₃Co₄ and d-ANC are characterized by two features: a broad energy range up to 60 meV. And a peak at about 25 meV for o-Al₁₃Co₄ and at 23 meV for d-ANC. Fig. 2.11 shows the calculated GVDOS which gives the best fits for these two structures. The main features of the experimental GVDOS are reproduced: the peak at 25 meV (23 meV) and the broad band. The spring models which gives this fit is shown in Fig. 2.10.

For o-Al₁₃Co₄ we remark the strong slope of the force constant as a function of the interatomic distance for the Al-Al interaction, while the Co-Co interactions are weak and have non vanishing values only for the second set of neighbors.

For d-ANC the Al-Al and Al-Co interaction are strong for the first neighbors but rapidly decreasing like in the Al₁₃Co₄ spring model. The difference to the Al₁₃Co₄ model is in the TM-TM interactions. Here, unlike the Al₁₃Co₄ model, we have strong TM-TM first neighbors interactions. This seems to be a consequence of the fact that in d-AlNiCo structure, the TM atoms have more TM neighbors compared to Al₁₃Co₄.

The GVDOS of i-ZnMgY at room temperature is characterized by a small energy range as compared to the Al₁₃Co₄ and d-ANC GVDOS. This is a consequence of the higher element masses in this alloy. The spring model which gives the best fit to the experimental i-ZnMgY GVDOS up to 40 meV using the μ -ZnMgY structure is presented in Fig. 2.10 We have a strong and constant first neighbors Zn-Zn interactions, for Zn-Zn interatomic distances higher than ~ 0.51 nm, the force constants vanish. We have also strong first neighbors Mg-Mg interactions and for interatomic distances higher than ~ 0.51 nm the force constants are negative. There is no Y-Y neighbors at distances lower than ~ 0.48 nm, we therefore set the force constants to zero below this limit. Beyond this limit, they are rather weak and decrease with increasing interatomic distance. The Zn-Y interactions are stronger than the Zn-Mg ones for first neighbors, while the Mg-Y interactions are weak and decrease from interatomic distance ~ 0.24 nm up to 0.355 nm and are zero after this limit.

The calculated GVDOS reproduces the three peaks of the experimental GVDOS of i-ZnMgY at 12, 17, and 25.5 meV using both structures: μ -ZnMgY and MgZn₂-Laves. However there are some differences between the two GVDOS. The peak at 12 meV is less pronounced for the MgZn₂-Laves structure, while the peak at 25.5 meV is stronger for this phase. There are also

more states at low frequency for the μ -ZnMgY structure.

Using the spring model, we calculate the eigenvalues and the eigenvectors of the dynamical matrix as explained in §2.1. From these values, we can deduce the total vibrational density of states (VDOS) and the partial VDOS of the different elements. The total VDOS is different from the GVDOS since the latter is also weighted by the coupling factors of the elements to the neutron. If the partial VDOS g_α of the different elements α are known, the total VDOS can be defined by:

$$g(\omega) = \sum_{\alpha} c_{\alpha} g_{\alpha}(\omega) \quad (2.9)$$

where M_{α} and c_{α} are respectively the mass and the concentration of the element α . Instead of the GVDOS which is given by Eq. 1.3, the VDOS is used to calculate physical properties like heat capacity and vibrational entropy.

Fig. 2.12 shows the partial VDOS of Al and TM atoms and the total VDOS for o-Al₁₃Co₄ and d-ANC. The partials of Al and TM demonstrate that the maximum in the GVDOS of both o-Al₁₃Co₄ and d-ANC is due mainly to the vibrations of TM atoms and the Al atoms in the Al-TM interactions because of the high Al concentration. The shoulder up to 60 meV is essentially due to the vibrations of Al atoms. It is also interesting to mention the spiky character of the Al partials, while the Co partial DOS is rather smooth. This spiky character of the partial Co DOS persists even when we used more than hundred thousand points in the Brillouin zone.

The partials VDOS of the μ -ZnMgY and MgZn₂-Laves shown in Fig. 2.12, demonstrate that the peaks at ~ 17 meV and 25.5 meV are mainly due to vibrations of Zn atoms (and some Mg atoms). While the peak at ~ 12.0 meV is due to vibrations of Y. This explains why this peak is missing in the calculated GVDOS of the MgZn₂-Laves structure where there are no Y atoms. The partial VDOS of Mg shows that the Mg vibrations cover the full energy scale of the GVDOS covered here.

2.4.4 Local VDOS

For a detailed investigation of the vibrational properties, we discuss the contribution of the different symmetry positions (or Wyckoff positions) to the DOS. There are 38 different Wyckoff positions for o-Al₁₃Co₄ (10 Co and 28 Al). For d-AlNiCo, the different Wyckoff positions are shown and labeled in Fig. 2.8. There are 3 TM and 8 Al positions.

For μ -ZnMgY, there are 2 Mg, 2 Y and 7 Zn positions. And finally, for MgZn₂-Laves, there are 3 Wyckoff positions. 2 Zn and 1 Mg.

For every position one can determine a ‘‘local vibrational density of state’’ (LVDOS) which is the projection of the DOS on these sites. Here, these LVDOS are discussed for d-ANC, μ -ZnMgY, and MgZn₂.

Fig. 2.14 shows the different LVDOS for the d-AlNiCo phase model. We notice that for TM positions with more TM-TM neighbours, the LVDOS is more broadened (TM1: 2TM-TM neighbours, TM7: 1 TM-TM neighbour, TM3: 0 TM-TM neighbours).

For Al positions, we notice that when the TM-Al interactions dominate, the intensity of the LVDOS is higher at low frequencies (Al(2), Al(5), Al(9) and Al(11)), while when the Al-Al

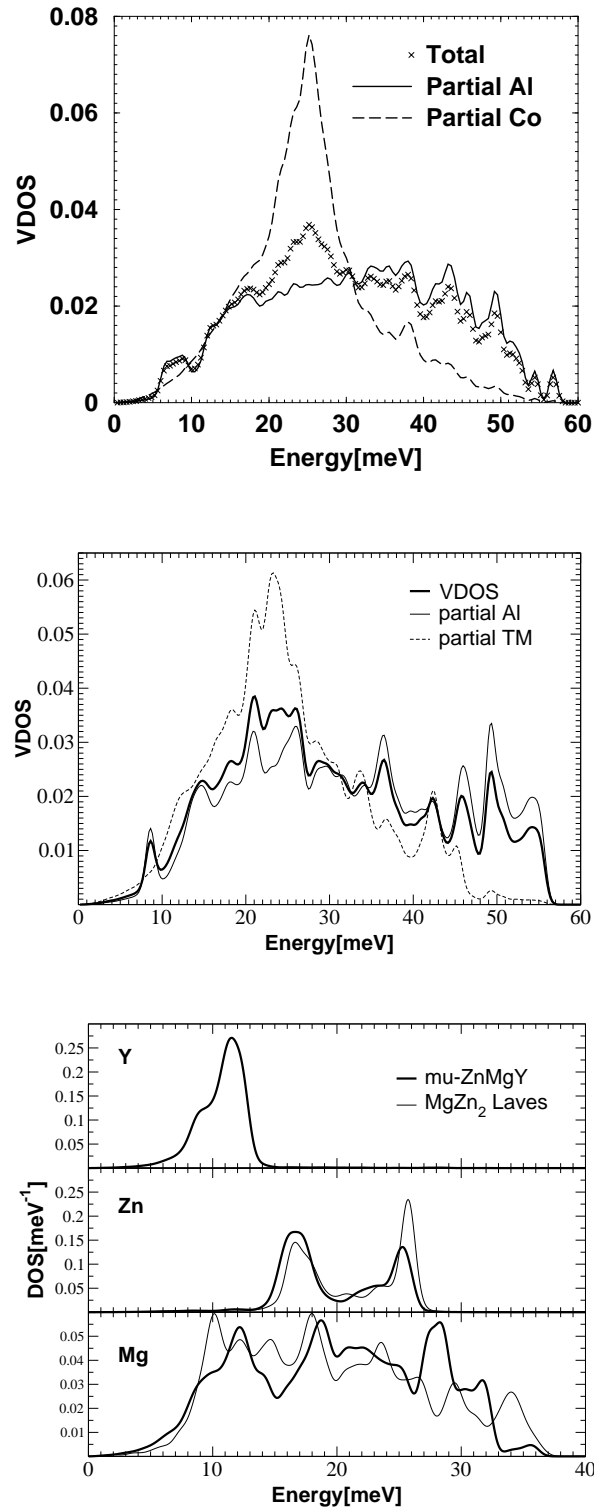


Figure 2.12: Top: total and partial VDOS of $\text{Al}_{13}\text{Co}_4$. The partial Al is broad and spiky, while the partial Co smooth except at high frequencies where it is slightly spiky, and has a maximum at $\hbar\omega \sim 25 \text{ meV}$ which is also the maximum of the $\text{Al}_{13}\text{Co}_4$ GVDOS Middle: the calculated VDOS and the partial DOS of d-AlNiCo. The peak in the GVDOS is due to TM vibrations, while the broad band is due to Al. Bottom: Partial VDOS of the $\mu\text{-ZnMgY}$ and Zn_2Mg structures.

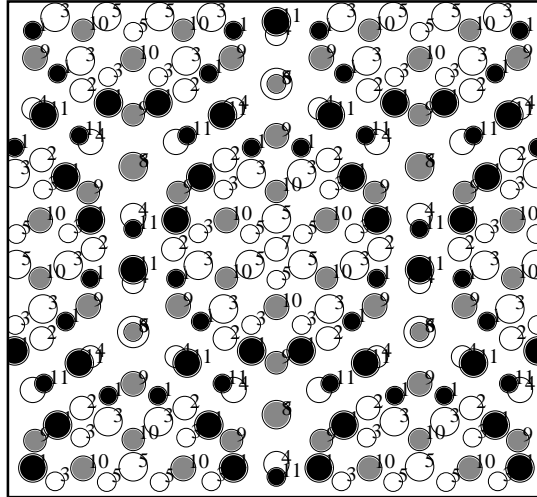


Figure 2.13: Wykoff positions for the μ -ZnMgY model

interaction dominate, the LVDOS intensity is higher at high energies (Al(4), Al(6), and Al(10)). Notice also the peak in the LVDOS of Al(8) which sits at the center of a decagon.

In Fig. 2.15 we show the different LVDOS of μ -ZnMgY and MgZn₂-Laves. The general feature of the Zn LVDOS is their broadness as compared to the Y or Mg LVDOS. The MgZn₂-Laves phase LVDOS are labeled with capital letters, while those of μ -ZnMgY are labeled with small letters. We notice the similarities between the following LVDOS: (mg2, Mg(10)), (zn1, Zn(7)), and (zn3, Zn(5)). Fig. 2.9 shows that the Zn(7) icosahedron in μ -ZnMgY structure is similar to the Zn(1) icosahedron in MgZn₂-Laves structure. And the positions Zn(1), Mg(2), and Zn(3) in MgZn₂-Laves are respectively similar to the positions Zn(7), Mg(10), and Zn(5) in μ -ZnMgY structure which results in the noticed similarities in their vibrational properties.

In the case of the μ -ZnMgY phase, we notice first that the Zn(6) is at the center of a distorted icosahedron with 3 Y neighbors. The corresponding LVDOS to Zn(6) has a pronounced peak at $\hbar\omega \sim 12$ meV. While the LVDOS is rather broad for the Zn(7) atoms which are at the centers of icosahedra with 6 Zn and 6 Mg neighbors. Finally, there is a strong peak at ~ 28 meV for Zn(4) which has a close Y neighbor. There are two different Mg sites: Mg(9) with Mg, Zn and Y neighbors, and Mg(10) with only Mg and Zn neighbors. The Mg(9) LVDOS is dominated by a peak at ~ 17 meV clearly emphasized by the Mg-Y interactions. While for Mg(10) LVDOS (which looks similar to mg2), the peak at ~ 26 meV is higher. Finally, there is a split in the Y(11) LVDOS which has in addition to Mg and Y neighbors as for Y(8) also Zn neighbors. The difference between Y(11) and Y(8) LVDOS can be compared to the difference between TM(1) and TM(3) LVDOS in the d-AlNiCo structure.

In conclusion, the density of states is dominated by the short range order: Atomic environment determines the shape, energy range and the positions of maxima. This property can be used to compare between structural models for quasicrystals where the atomic ordering is not sufficiently understood. For the i-ZnMgY phase, an enhancement of the low frequency GVDOS is expected by the addition of Y atoms. This effect is already present for the μ -ZnMgY cal-

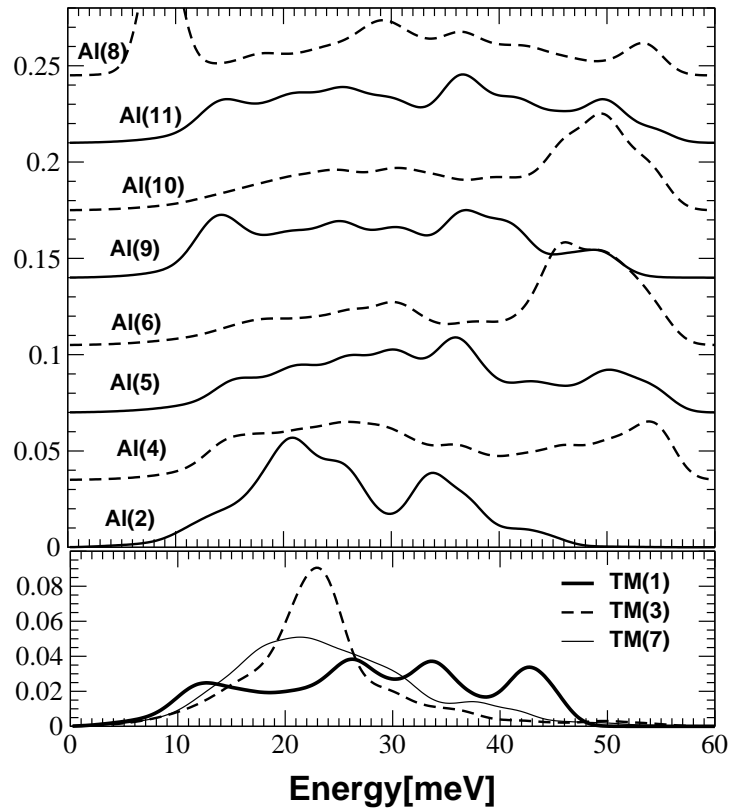


Figure 2.14: The local VDOS for d-AlNiCo, There are 3 TM and 8 for Al corresponding to the inequivalent positions of these elements in the model.

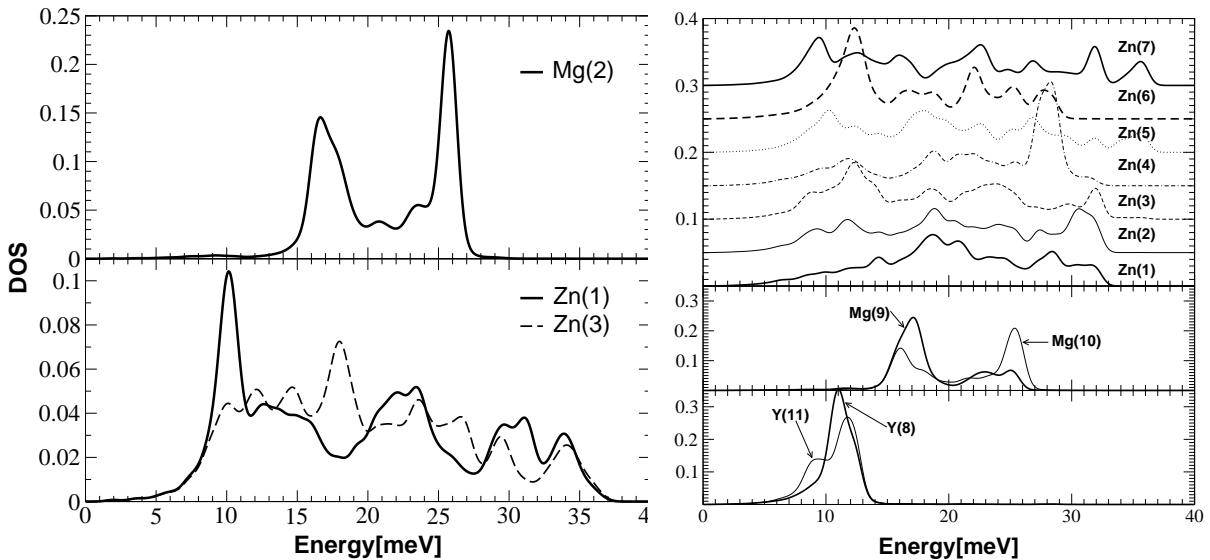


Figure 2.15: Local VDOS for the Wyckoff sites for (left): MgZn_2 -Laves, and (right): μ -ZnMgY. Notice the Zn(6) partial (right). The Zn(6) atoms sit at the center of distorted icosahedra with more Y neighbors.

culated GVDOS as compared to the MgZn₂-Laves ones. This can be seen in Fig. 2.11, where the experimental GVDOS of i-ZnMgY is higher than those of the μ -ZnMgY and MgZn₂-Laves phases at low frequencies, while the peaks at ~ 17 meV and 26 meV are less intense for the i-ZnMgY GVDOS.

2.4.5 Character of the modes

Harmonic normal modes of vibrations can be rigorously classified as extended, critical or localized. We can roughly define extended modes as vibrational modes with participation ratio close to 1 due to the strong interactions that exist between the constituent atoms. Localized modes are modes with small participation ratio. In metallic solids, which tend to crystallize in close-packed structures, local modes are exceedingly rare. When present, local modes are usually associated with weakly bound atoms. Finally, critical modes are neither extended nor exponentially localized.

In perfect periodic crystals all modes are extended, while in disordered materials, there are often *localized* modes. The localization in disordered materials usually occurs at high frequencies, while at low frequencies there are always acoustic modes which are extended by definition. There may occur also 'localized' modes at low frequencies. These modes interact with the low frequency extended modes, losing the strictly local nature but conserving some localized characters like their participation ratio [Allen et al (1999)]. These modes are called resonant or *quasi-localized* and are very important for the low temperature properties of these materials.

The participation ratio cannot distinguish between localized and quasi-localized modes since both of them have small participation ratio. Because the localized modes result from some structural configurations which are not repeated periodically, they are outside the lattice frequency continuum, and they cannot couple to the lattice modes and their eigenvectors magnitudes decay exponentially:

$$|\vec{e}_i(\vec{R}_n)| \propto \exp\left(-\frac{|\vec{R}_n - \vec{R}_0|}{\zeta_i}\right) \quad (2.10)$$

ζ_i is the localization length of the i -th normal mode, if the mode is localized. $\vec{e}_i(\vec{R}_n)$ is the amplitude of the eigenvector of atom n at the i -th normal mode. To illustrate this effect, we show in Fig. 2.16 three selected modes from the d-ANC spectrum: an extended mode (crosses, $\hbar\omega \approx 3.10$ meV, $P \approx 1.0$), a quasi-localized mode (empty circles, $\hbar\omega \approx 8.40$ meV, $P \approx 0.23$ (mode 3 in Fig. 2.17)) and a localized mode (filled triangles, $\hbar\omega \approx 54.40$ meV, $P \approx 0.065$ (mode 1 in Fig. 2.17)). For each mode i of those modes, the atom with the largest $|\vec{e}|^2$ is located, and taken as origin. The figure shows values of $|e(\vec{R}_n)|^2$ averaged over spherical shells of $|\vec{R}_n|$ of width $\delta R = 0.02$ nm. Fig. 2.16 shows the decrease of $|\vec{e}|^2$ for the localized mode at high energy, while for the mode at $\hbar\omega \approx 8.40$ meV $|\vec{e}|^2$ does not decrease even if the participation is small, this mode is called a quasi-localized mode.

orthorhombic Al₁₃Co₄

For Al₁₃Co₄, we find that the participation ratio is scattered (see Fig. 2.17). Modes with a low participation ratio are found at low energies but these modes are quasi-localized. There are two

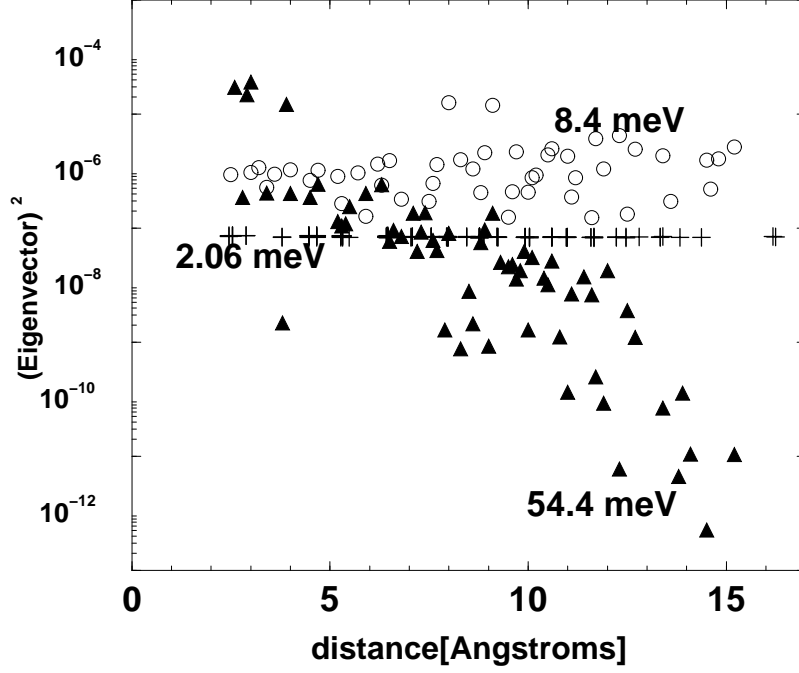


Figure 2.16: Typical behavior of $|\vec{e}|^2$ with distance. Here are presented three modes from the d-AlNiCo spectrum. An extended mode (crosses, $\hbar\omega \approx 2.06$ meV), a “quasi-localized mode” (empty circles, $\hbar\omega \approx 8.4$ meV), and a localized mode (dark circles, $\hbar\omega \approx 54.4$ meV) with localized length $\zeta \approx 0.207$ nm.

groups of quasi-localized modes, one at $\hbar\omega < 10$ meV and the other is at $\hbar\omega \sim 12$ meV coinciding with energies where there are marked maxima in the Al partial VDOS. At high energies, most of the modes have participation ratio between 0.2 and 0.7, except at some intermediate energies where we have a sudden decrease of the participation ratio, coinciding also with the maxima in the total VDOS. True localized states are found at energies in the range $\hbar\omega > 50$ meV. The participation ratio presents a local maximum at $\hbar\omega \sim 25$ meV which corresponds to the maximum in the GVDOS and the peak in the Co partial VDOS. The distribution of states per participation ratio shows a maximum at $P \sim 0.7$ (see Fig. 2.18) which reflects the character of the participation ratio.

decagonal AlNiCo

The calculated participation ratio of the actual model shows some similarities with the participation ratio of $\text{Al}_{13}\text{Co}_4$. In fact, as we can expect, there are many modes with a participation ratio between ~ 0.2 and ~ 0.7 , but in the case of d-AlNiCo, the participation ratio tends to be lower as we can see when we compare the two distributions of the participation ratio g . In the case of d-AlNiCo, g has high values in comparison with $\text{Al}_{13}\text{Co}_4$ at low participation ratio, while in the case of $\text{Al}_{13}\text{Co}_4$ it has rather a narrow and pronounced maximum between ~ 0.5 and 0.7 . The participation ratio of d-AlNiCo is also scattered, and the features in the participation ratio corresponds to the features in the GVDOS. We find modes with low participation ratio at the two extremes of the energy region covered: at high energy these modes are localized as the eigenvectors decrease exponentially with distance. While at low energy the

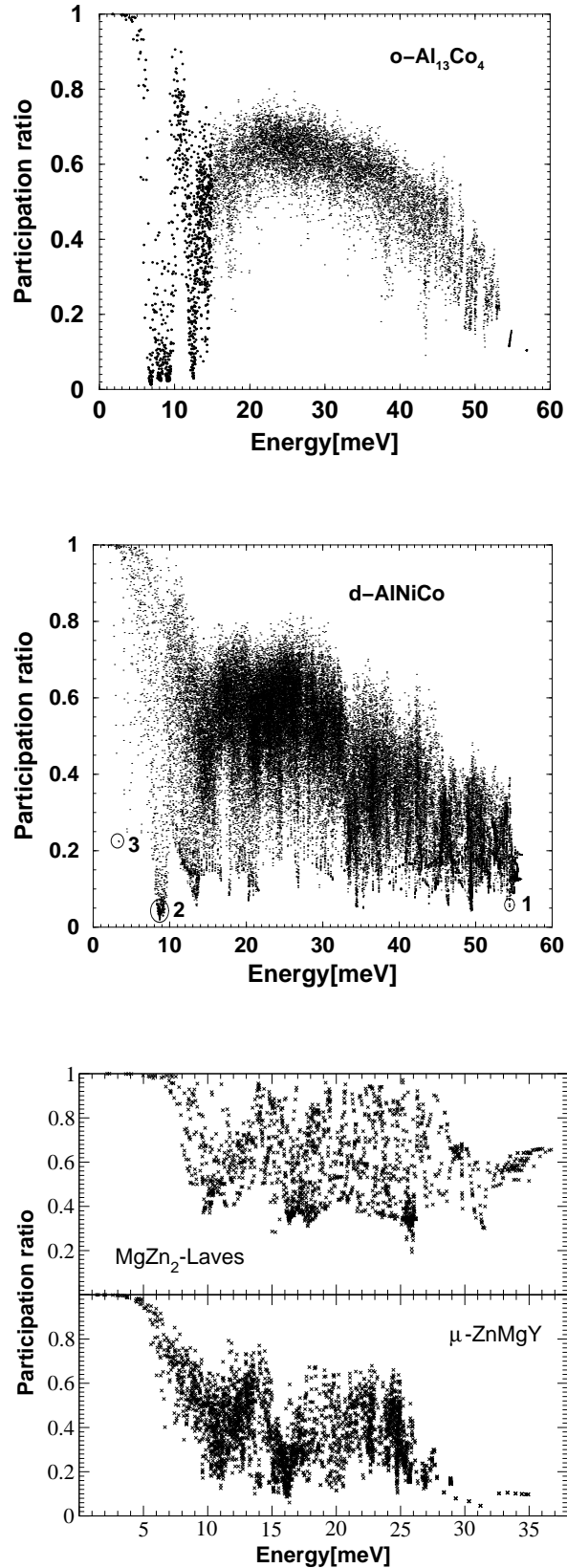


Figure 2.17: Top: participation ratio of the full occupancy model of $\text{Al}_{13}\text{Co}_4$, there are low frequency localized modes at the positions where we have maxima in the Al partial VDOS. The participation ratio has a scattered character Middle: the participation ratio of $d\text{-AlNiCo}$. Most of the modes have a participation ratio with values between ~ 0.2 and 0.7 . At low frequencies, there are modes with very low participation ratio. Bottom: the participation ratio of the $\text{MgZn}_2\text{-Laves}$ and $\mu\text{-ZnMgY}$: notice the three groups of modes in the $\mu\text{-ZnMgY}$ participation ratio figure, the positions of these modes coincide with the positions of the three peaks in the GVDOS of this structure.

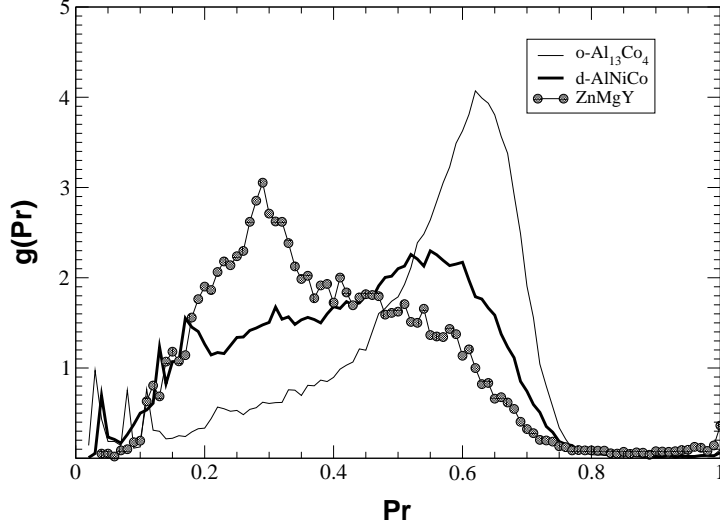


Figure 2.18: distribution of the participation ratio

modes are quasi-localized (Fig. 2.16). Fig. 2.19 show the plot of the eigenvectors of one of the modes numbered 3 for d-AlNiCoNi in Fig. 2.17 . This figure shows that this quasilocalized mode originates in vibration of the two inner rings (TM1 and Al2) along the pseudoperiodic axis.

MgZn₂-Laves and μ -ZnMgY

Both the participation ratio of MgZn₂ and μ -ZnMgY have a scattered character with more modes with low values for some of the states at energies of local maxima in the GVDOS (Fig. 2.17). There are more modes with low values of participation ratio in the case of μ -ZnMgY, and at high energy, we observe a branch of localized modes for μ -ZnMgY, while for MgZn₂-Laves phase a branch appears with modes which tend to be more extended. As for Al₁₃Co₄ and for d-AlNiCo, there are many modes with intermediates values of participation ratio for μ -ZnMgY. At lower energies we also have quasi-localized modes for μ -ZnMgY. The participation distribution function (Fig. 2.18) shows more states with low participation ratio for ZnMgY than for d-AlNiCo with a peak at $P \approx 0.25$.

2.4.6 Specific heat

The phonon DOS ($g(\omega)$) provides in the harmonic approximation the vibrational contribution to the heat capacity by:

$$C_{ph} = \frac{\partial E}{\partial T} = \int g(\omega) k_B \frac{(\frac{\hbar\omega}{k_B T})^2 \exp(\frac{\hbar\omega}{k_B T})}{[\exp(\frac{\hbar\omega}{k_B T}) - 1]^2} d\omega \quad (2.11)$$

At low temperatures, the phonon heat capacity C_{ph} should have in principle a Debye-like behavior and have the same values as the Debye heat capacity C_D defined by:

$$C_D = \left[\frac{2\pi^2 k_B^4 M}{5\hbar^3 v_s^3 \rho} \right] T^3 \quad (2.12)$$

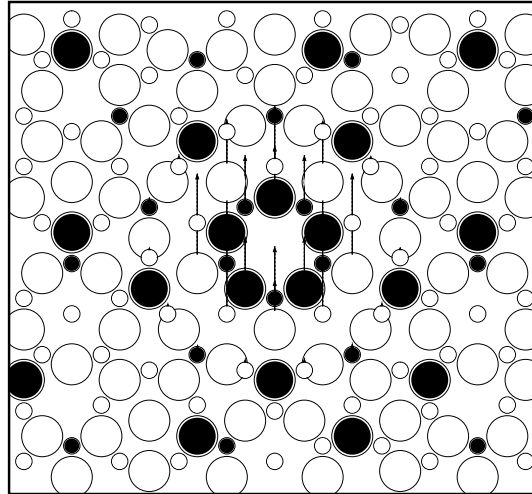


Figure 2.19: modes (3) in Fig. 2.17, ($\hbar\omega \sim 4$ meV, $P \sim 0.32$), vibration of TM only along the pseudo-decagonal axis.

where the term between brackets is constant, ρ is the mass density, M the mass of one gram-atom and v_s is the mean sound velocity defined as:

$$\frac{3}{v_s^3} = \frac{2}{v_t^3} + \frac{1}{v_l^3} \quad (2.13)$$

v_t and v_l are respectively the transverse and the longitudinal sound velocities. In this section, the phonon heat capacity is calculated for o-Al₁₃Co₄ and d-AlNiCo. The sound velocity was calculated for o-Al₁₃Co₄ by diagonalizing the dynamical matrix at q-points $Q = \Gamma + dQ$. The three smallest eigenvalues give the longitudinal and the two transverse sound velocities giving $v_s \approx 4000 \text{ m s}^{-1}$. For d-AlNiCo, the experimental sound velocity $v_s \approx 4900 \text{ m s}^{-1}$ [Dugain et al (1999)] was used.

Fig. 2.20 shows the temperature dependence of $\frac{C_{ph}}{T^3}$ respectively for o-Al₁₃Co₄ and d-AlNiCo. A clear deviation from the Debye heat capacity (dashed line in both figures) is observed at low temperatures for the two systems

These results are in agreement with experimental measurements [Chernikov et al (1998)] of the heat capacity of some quasicrystals (i-AlPdMn, i-ZnMgY). In order to have agreement between the two heat capacities for o-Al₁₃Co₄, $v_s = 3500 \text{ m s}^{-1}$ was required in Eq. 2.12. This indicates that the observed excess heat capacity is closely related to an excess phonon DOS at low frequencies. In fact Fig. 2.21 where the integrand in Eq. 2.11 for a set of temperatures shows that the main contribution to the heat capacity at low temperatures originates in the low frequency modes. To conclude, it is legitimate in this case to claim that this excess heat capacity is due to the low frequency quasilocalized modes shown in the previous sections.

2.5 Conclusion

The use of spring models allowed us to investigate the lattice dynamics in d-AlNiCo model, o-Al₁₃Co₄ and Zn₂Mg-Laves structures, and μ -ZnMgY model.

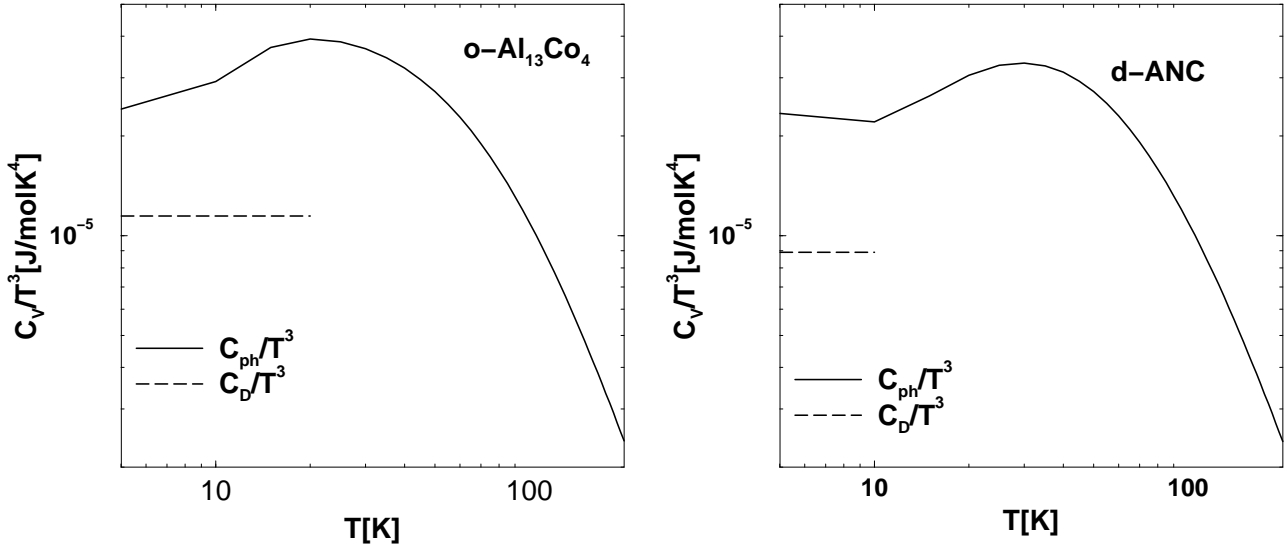


Figure 2.20: $\frac{C_{ph}}{T^3}$ and $\frac{C_D}{T^3}$ versus T for $\text{Al}_{13}\text{Co}_4$ (left) and $d\text{-AlNiCo}$ approximant(right). Notice the extra C_{ph} relatively to C_D observed in both cases. This extra heat capacity is a consequence of the low energy extra VDOS.

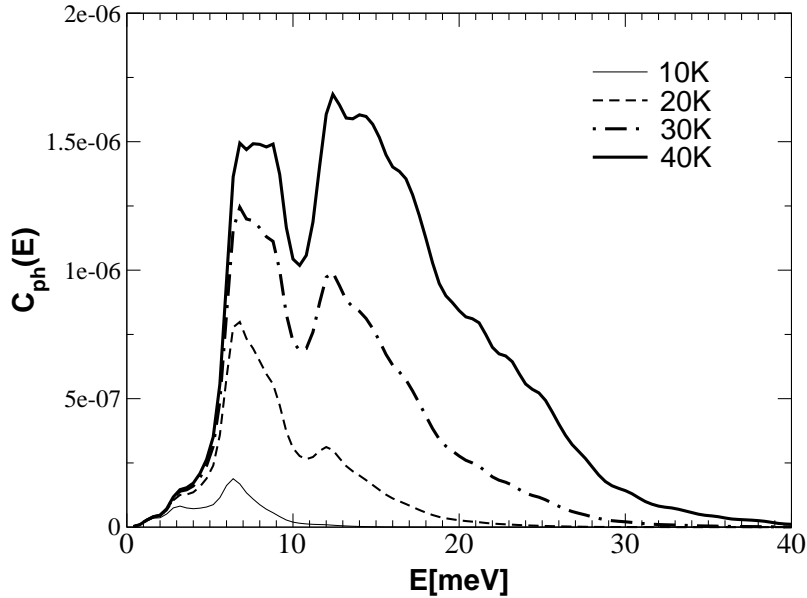


Figure 2.21: The major contribution to lattice heat capacity C_{ph} at low temperatures comes from low energy excitation.

The calculation of the partials VDOS provided some explanations of the shape of the experimentally measured GVDOS, while the local VDOS gave more detailed informations.

The participation ratio of the d-AlNiCo model and o-Al₁₃Co₄ structure shows more localized modes at low energy compared to the μ -ZnMgY model one. The analysis of these modes shows that they are quasi-localized. While at high energy there are more localized modes for the μ -ZnMgY model.

Chapter 3

Atomic dynamics via realistic pair potentials

This chapter summarizes the work published in [Mihalkovič, Elhor and Suck (2001)]. Realistic Al–Co pair potentials [Phillips et al (1994), Moriarty and Widom (1997)] are used to investigate the lattice dynamics in the $\text{Al}_{1-x}\text{TM}_x$ crystalline structures with $x \leq 0.3$. We study complex crystalline structures related to quasicrystals ($\text{Al}_9\text{Co}_2\text{Ni}$, $\text{o-Al}_{13}\text{Co}_4$) and a model of the approximant of decagonal d-AlNiCo, as well as simple structures (Al_3Ni , Al_5Co_2) within the harmonic approximation to assess the impact of the structural complexity on the phonon density of states, the sound velocity, the Debye–Waller factor, and on the character of the phonon states at low energies.

3.1 Introduction

Both decagonal and icosahedral quasicrystal phases exist in Al-rich aluminides. Two representative phases are the icosahedral phase i-AlPdMn [Beeli et al (1991)] and the decagonal phase d-AlNiCo [Yamamoto et al (1990)]. Both phases were extensively studied experimentally and a considerable progress was achieved in the structure determination, providing a legitimate motivation for theoretical investigations. Moreover, some of these phases are thermodynamically stable and rather perfect monocrystals can be obtained. One way of understanding why quasicrystals exist is to compare the energies of these phases with periodic crystals with similar composition. More realistic interaction models than springs are needed to achieve such a task. This is now possible in Al–TM systems since a big progress was achieved in modelling their pair potentials. Semi-empirical pair potentials have been designed and tested for Al–Mn [Mihalkovič (1996b)] and Al–Co systems [Phillips et al (1994)], and pair potentials calculated via ab-initio generalized pseudopotential theory (GPT) have been determined for a range of Al–TM systems [Moriarty and Widom (1997)]. The latter potentials were applied successfully in a study of the Al–Ni and the Al–Co binary phase diagrams [Widom and Moriarty (1998)].

Here we go a step further in investigating various aspects of the lattice dynamics and the impact of the structure on dynamical properties. One reason of choosing to carry out our study in the Al–Ni–Co systems is the variety of phases present, especially in the range $x=0.2$ – 0.3 where also the decagonal phases is situated. For the comparison there are rather simple crystalline structures like Al_3Ni and Al_5Co_2 in contrast to $\text{Al}_9\text{Co}_2\text{Ni}$ and $\text{o-Al}_{13}\text{Co}_4$ structures

of which the latter have a close relationship to the decagonal quasicrystals near $\text{Al}_{70}(\text{Ni},\text{Co})_{30}$ composition.

3.2 Structural models

The structural models for d-AlNiCo phase and for o- $\text{Al}_{13}\text{Co}_4$ were already discussed in the previous chapter. In order to assess the impact of the structural and chemical variation on the dynamical properties of the Al-Co system near the composition of the decagonal quasicrystal, we choose from the Al-(Ni,Co) phase diagram three other crystalline phases: Al_3Ni , and $\text{Al}_9\text{Co}_2\text{Ni}$ with the TM content $x \sim 0.25$, and Al_5Co_2 at $x \sim 0.29$. The pair interactions are in principle sensitive to the variation of x and of the atomic density (see §3.3). This fact constrains us to compare only *the differences* in the dynamical properties when these two parameters are fixed: this is nearly exactly the case for the Al_3Ni vs. $\text{Al}_9\text{Co}_2\text{Ni}$ at $x=0.25$, and approximately for our d-ANC approximant model vs the Al_5Co_2 structure near $x=0.29$. The o- $\text{Al}_{13}\text{Co}_4$ structure is closely related to both $\text{Al}_9\text{Co}_2\text{Ni}$ and d-ANC. The basic structural data of these phases are compiled in the Tab. 3.1, and the projected structures are shown in Fig. 3.1(1- 6).

The relationship between o- $\text{Al}_{13}\text{Co}_4$ and $\text{Al}_9\text{Co}_2\text{Ni}$ is illustrated in Fig. 3.1(3,4), showing the structures projected along the pseudodecagonal axis. Perpendicular to this axis, the atoms in o- $\text{Al}_{13}\text{Co}_4$ are arranged in flat (F) (smaller circles in the figure) layers, alternating with puckered (P) (larger circles) layers, and with mirror planes on the F -layers. Connecting nearest Co atoms in the P layer leads to a tiling of pentagons and skinny rhombi with $\sim 36^\circ$ acute angle (solid lines in the figure). The $\text{Al}_9\text{Co}_2\text{Ni}$ repeats a sequence of *six* pseudodecagonal layers: $PP'F'PF$. The TM atoms in P layers are again located on vertices of the skinny rhombi, but there is only $3/5$ fraction of the pentagon tile. Up to the positions of certain Al atoms, this structure may be viewed as a twinned fragment of the o- $\text{Al}_{13}\text{Co}_4$ unit cell motif.

On the other hand, the Co atoms in the F layer of the o- $\text{Al}_{13}\text{Co}_4$ structure are located approximately at vertex positions of a tiling of squashed hexagons with an edge length of $\sim 6.5\text{\AA}$. The squashed hexagon tile has been proposed as one of the three building units (hexagon, boat, star) for models of the decagonal AlCo and AlCuCo phases [Cockayne and Widom (1998a, 1998b)].

The o- $\text{Al}_{13}\text{Co}_4$ phase has no fractional occupancies reported from the diffraction data: however, the presence of a few very short Al-Al bonds ($\sim 2.3\text{\AA}$), some large refined Al Debye-Waller factors as well as energetic considerations [Widom et Moriarty (1998)] suggest that some Al sites might be partially occupied. The phenomenon of partial occupancy and its impact on the vibrational properties deserves special attention and later a comparison of the full-occupancy o- $\text{Al}_{13}\text{Co}_4$ model with variant models with fractional occupancy of some Al sites will be given.

As this study is entirely based on isotropic pair potentials, the differences between the structures are conveniently represented by the pair distribution functions (PDF) $g(r)$. In Fig. 3.2, we compare the $g(r)$ of Al_3Ni with that of $\text{Al}_9\text{Co}_2\text{Ni}$ (*a*), and Al_5Co_2 with the model of the d-AlNiCo approximant (*b*).

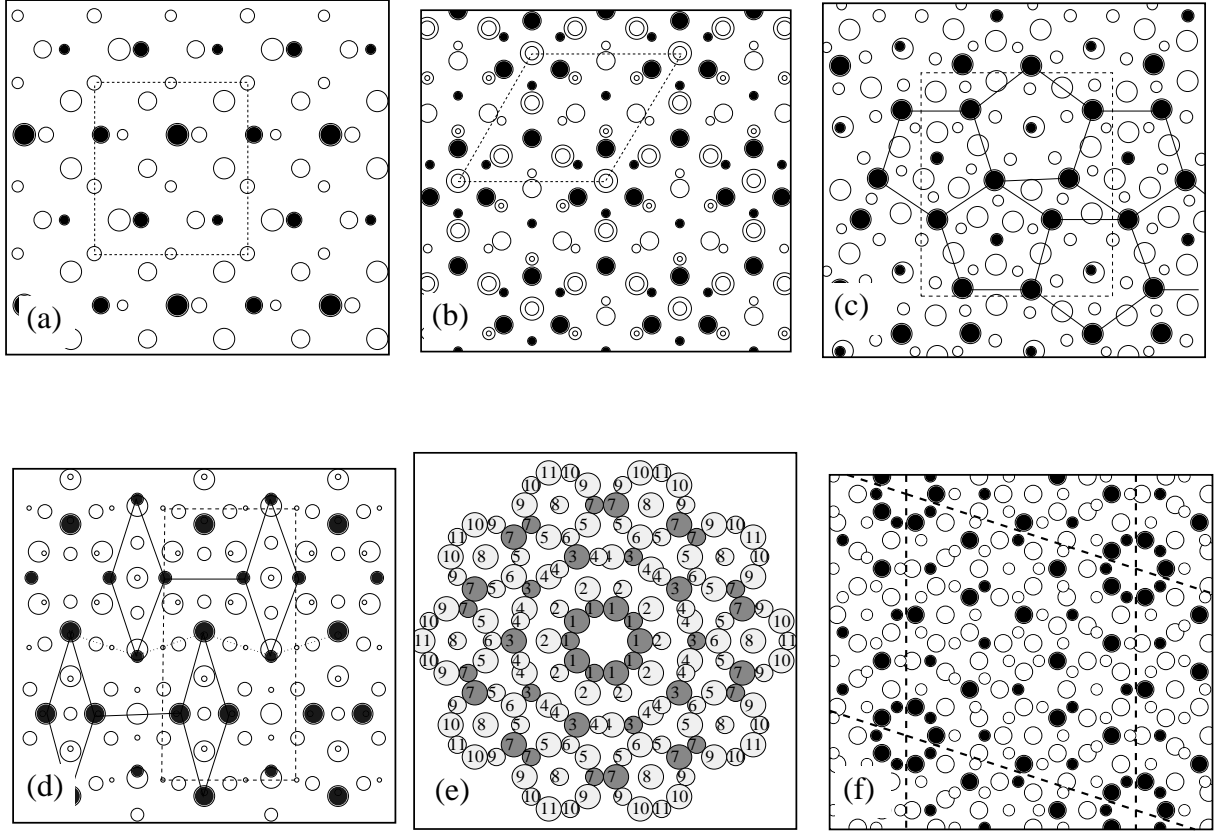


Figure 3.1: Structure of Al_3Ni (projection along z -axis) (a), Al_5Co_2 (projection along 3-fold axis) (b), $o\text{-Al}_{13}\text{Co}_4$ (pseudodecagonal axis) (c), $\text{Al}_9\text{Co}_2\text{Ni}$ (pseudodecagonal axis) (d), decagonal cluster in the model of d-ANC approximant (e), the approximant model of the d-ANC (pseudodecagonal axis) (f). Dark circles are TM atoms, open circles Al. The radius of the circles scale with the atomic coordinate perpendicular to the plane.

Table 3.1: TM content x , the reference x_{ref} , atomic density ρ_{at} , relative volume Ω/Ω_{ref} (Ω is the atomic volume used for the calculation, Ω_{ref} is the volume at x_{ref} , see §. 3.3) and valence electron density ρ_{el} , assuming 1.8 valence electrons per TM atom (TM \equiv Co) for selected Al(Ni,Co) structures used in this study.

structure	x	x_{ref}	ρ_{at} [\AA^{-3}]	Ω/Ω_{ref}	ρ_{el} [\AA^{-3}]	Pearson symbol
Al	0.000	0.000	0.0602	1.000	0.181	$cF4$
$o\text{-Al}_{13}\text{Co}_4$	0.235	0.250	0.0701	0.956	0.191	$oP102$
$\text{Al}_9\text{Co}_2\text{Ni}$	0.250	0.250	0.0686	0.984	0.185	$oI96$
Al_3Ni	0.250	0.250	0.0687	0.982	0.186	$oP16$
Al_5Co_2	0.286	0.286	0.0726	1.000	0.193	$hP28$
d-ANC	0.291	0.286	0.0724	1.005	0.191	$mP110$

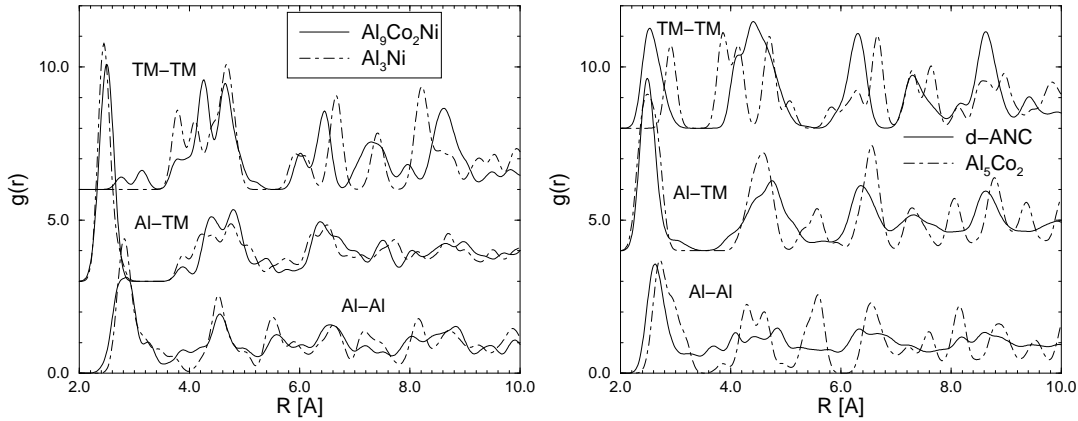


Figure 3.2: Comparison of radial distribution functions at $x=0.25$ ($\text{Al}_9\text{Co}_2\text{Ni}$ and Al_3Ni structures, left) and at $x \approx 0.30$ ($d\text{-AlNiCo}$ model and Al_5Co_2 , right). In the case of $d\text{-AlNiCo}$, the PDF was taken from the model relaxed under the SE potentials, in the other cases the structures are unrelaxed. In all cases they are convolved with a gaussian with $\sigma = 0.01$.

3.3 Pair Potentials

A significant progress was made in the evaluation of the interatomic interactions in the Al-TM alloys. The first step in this direction was achieved by Phillips et al [Phillips et al (1994)] by a set of semiempirical pair potentials for Al-Co systems (Fig. 3.3). These potentials depend on a set of parameters that were determined either from experimental data or from ab initio calculations, therefore they are called semi empirical (**SE**). The Phillips SE pair potentials neglect the direct d-d interactions (although the d-d interactions mediated by the electron sea are included), and they are supposed to be valid at constant valence electron density of *fcc* Al.

Moriarty and Widom developed recently a full GPT interatomic interaction for Al-TM alloys. These potentials include all *sp*, *sp-d* and *d-d* interactions within the density-functional theory and the local density approximation. There is a deep minimum of the Co-Co GPT potential not observed by Phillips et al because of the neglect of the d-d interactions. The introduction of the *sp-d* hybridization and screening interaction in the GPT treatment is responsible in part of the strong oscillation of these potentials (Fig. 3.3).

For a transition-metal content of $x \approx 0.3$, the energetics appears to be correctly described by the potentials truncated at the pair-potential level. However, preferred stability of Al_5Co_2 over Al_5Fe_2 structure in Al-Co system required the inclusion of the many-body terms in the pair potential expansion.

In the present study, only the *pair* potential term in the expansion of the total energy is considered:

$$E_p(\mathbf{R}_1, \dots, \mathbf{R}_N) = \sum_{\mathbf{n}} \sum_{i < j} v_2^{\alpha\beta}(|\mathbf{R}_j - \mathbf{R}_i - \mathbf{n}|; \Omega, x), \quad (3.1)$$

which depends explicitly on the atomic volume Ω and the TM concentration x . Here, \mathbf{n} denotes lattice translation vectors, and $\mathbf{R}_1 \dots \mathbf{R}_N$ are the positions of the N atoms within the unit cell, where $\alpha\beta$ stands for the Al-Al, Al-TM or TM-TM pairs correlations. It turns out that for the sequence of atomic volumes experimentally observed in stable Al-Co phases with $x \approx 0.3$,

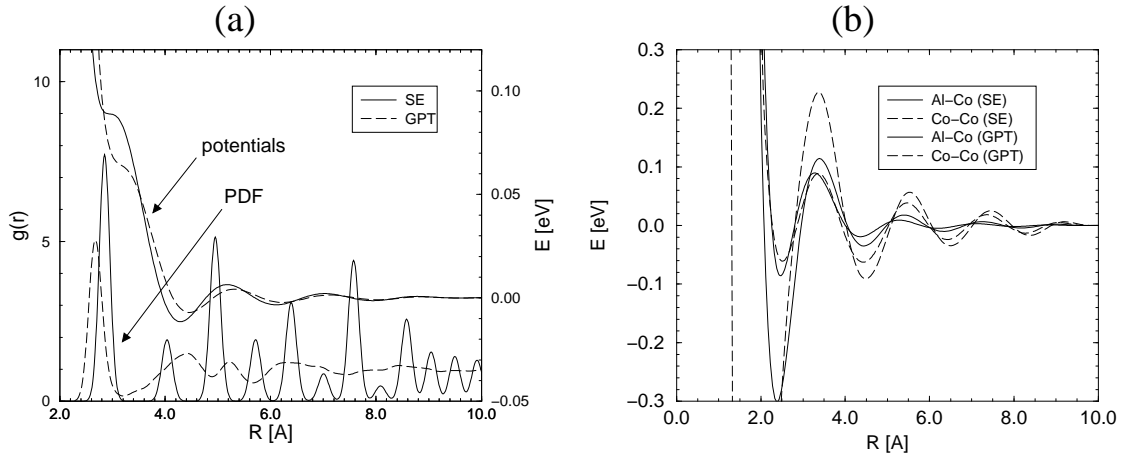


Figure 3.3: (a):Radial distribution functions (convolved with gaussian with half-width $\sigma=0.01$ nm) and two sets of Al–Al pair potentials. The energy scale for the potentials is displayed on the right side. For the GPT potential, the structure is *fcc* Al, for the SE potential it is an amorphous phase resulting from MD annealing. (b) SE and GPT Al–Co and Co–Co pair potentials.

the x and the Ω dependence nearly accurately cancel each other, so that the pair potentials have no apparent dependence on x (while the cohesive energies are significantly shifted by the volume–energy term which *is* strongly x –dependent). Thus, for the limited set of compositions x_{ref} and atomic volumes Ω_{ref} at which the GPT potentials were evaluated, it is plausible to use a single set of $x = 0$ potentials, at the reference volumes and TM concentrations. We show the $x = 0$ set of the potentials from [Moriarty and Widom (1997)] in Fig. 3.3.

The calculations are done at $x=0.25$ and $x \sim 0.29$, while the *experimental* atomic volumes Ω determined from the diffraction data are used. Only in the case of the full occupancy model of the *o*-Al₁₃Co₄, Ω departs appreciably from Ω_{ref} (see the fifth column in the Tab. 3.1) in which case additional calculations were performed to investigate the dependence of the vibrational properties on the atomic volume via an Al/vacancy substitution or rescaling of the lattice parameters. Two structures in our list (full-occupancy *o*-Al₁₃Co₄ and *d*-AlNiCo model) occurred at $x \neq x_{ref}$; in these cases, we evaluated Ω_{ref} assuming valence electron density $\rho_{el}(x_{ref})$, and $Z_{TM}=1.8$.

The truncation of the GPT potentials at the pair–potential level causes a deep well in the Co–Co potential at an unphysically short 1.8\AA separation, as a result of the direct $d-d$ interaction between Co atoms. This spurious feature was attributed to the lack of the many–body terms in the potential energy expansion [Widom and Moriarty (1998)]. While the GPT potentials is still used for Al₅Co₂, in which case the neighboring Co atoms do not move unphysically close to each other upon relaxation of their positions under action of the GPT potentials, in the *d*-AlNiCo case the spurious Co–Co well has a fatal impact on the rings of neighboring Co atoms, and *d*-AlNiCo was excluded from the list of structures studied under the GPT potentials.

In the calculations, we truncated the GPT potentials using an interaction cutoff radius $r_{cut}=1.0$ nm. With the same interaction cutoff the SE potentials exhibit a strong tendency towards phonon instability. The stability was significantly improved when we reduced the cutoff radius to $r_{cut}=7\text{\AA}$ in this case, and we adopted this cutoff radius for the SE potentials.

3.4 Stability

Before diagonalizing the dynamical matrix, the structure must be relaxed to its equilibrium state under the interatomic forces. The mechanical stability of simple structures with few atoms per unit cell is robust with respect to the variation of the interatomic forces, while complex structures are sensitive to the detailed shape of the interatomic potentials and to their oscillating tails.

After the relaxation of the structures studied here, equilibration of the atomic forces using relaxation at $T=0$ K introduced small atomic displacements, but did not disturb the topological ordering of atoms. A main role in stabilization is played by the rigidity of the subnetwork of Co atoms, arising from (i) their uniform distribution in Al matrix. At the same time, the Al–Co pair potential has a deep minimum at the nearest neighbor distance. (ii) Co–Co potential exhibits a strongly oscillating tail, correlating Co atom positions far beyond the second–neighbor shells. All structures listed in Table 3.1 achieved mechanical stability such that the atomic positions corresponded to the minimum of $E_p(R_1\dots R_N)$ within the machine precision.

In the case of the SE potentials, despite their mechanical stability, two structures (Al_5Co_2 and d-ANC) exhibited few imaginary eigenfrequencies. Additional relaxation procedures were needed to avoid the instability: we took supercells containing few images of the unit cell (see column “note” in the Tab.3.2), and performed MD annealing at finite temperature followed by a conjugate gradient relaxation of the atomic positions. This treatment introduced additional displacive modulation due to the breaking of the translational symmetry, and decreased the pair potential energy marginally by 0.2 meV/atom for Al_5Co_2 structure, and appreciably by ~ 10 meV/atom per atom for d-ANC. Thus such a displacive modulation may become a non-negligible factor favouring the complex structures.

3.5 Pure Aluminum limit

In the limit of $x=0$, ie pure fcc Al, , a fundamental deviation of the SE Al–Al potential from the expected behaviour is observed. Due to its high symmetry, the *fcc* Al structure does not exhibit any relaxation displacements at $T=0$ K. But an MD annealing at finite temperature of a supercell model with 256 atoms in the supercell leads to a phase transformation to an *amorphous phase*, with a decrease of the structural energy by ~ 60 meV/atom relative to *fcc* Al. In Fig. 3.3, we plot the Al–Al potential together with the *fcc* Al pair–distance histogram and the pair distribution function of the relaxed supercell model.

Comparison of the two sets of potentials at the nearest–neighbor distance shows that in the case of the GPT potentials the interaction is strongly repulsive, while in the SE case the interaction is almost neutral, due to the shelf–like feature in the potential, the potential well near 4.5\AA is filled by distorting the bonds at 4.05\AA and 4.96\AA , at the price of shrinking the nearest–neighbor bond at 2.86\AA . (A realistic phonon spectrum is obtained only when we scale the *fcc* Al unit cell volume by a factor of $0.96^3 \sim 0.89$.) Part of the reason for the improved stability at higher x –content is the fact that the pair potentials remain approximately invariant, while the volume per atom shrinks as x increases. Consequently, the nearest–neighbor Al–Al

bonds accidentally fall on the repulsive shoulder of the potential, constraining the motion of the Al atom.

3.6 Phonon DOS and atomic structure

By diagonalizing the complex dynamical matrix on a mesh of points inside the Brillouin zone, we obtain the corresponding number of eigenvalues and eigenvectors for each structure. Fig. 3.4 shows the calculated phonon densities of states (VDOS) of Al_5Co_2 , d-AlNiCo, and pure Al limit for two sets of interactions (SE and GPT). The sound velocities are evaluated (Table 3.2) from the three smallest eigenvalues of the dynamical matrix near the Γ -point of the Brillouin zone where the dispersion curves are still linear, and averaging over the three directions. We assign the two smallest eigenvalues to the transverse modes, and the third to the longitudinal. In the long wavelength (acoustic) limit, the phonon DOS $g(\omega)$ is related to the mean sound velocity v_s via the equation:

$$\rho g(\omega) = \frac{\omega^2}{2\pi^2 v_s^3} + \beta \omega^4 + \dots \quad (3.2)$$

where ρ is the atomic number density, and the coefficient β reflects the cubic nonlinearity of the dispersion relation.

The sound velocity is calculated by fitting the phonon DOS to Eq. 3.2. The list of calculated sound velocities is given in Table 3.2, and in Table 3.3 we show a list of calculated Debye–Waller factors which we calculated using Eq. 1.4. For comparison, we compiled the Debye–Waller factors for some Al–rich aluminides available in literature in Table 3.4.

3.6.1 Al_3Ni , o- $\text{Al}_{13}\text{Co}_4$, and $\text{Al}_9\text{Co}_2\text{Ni}$

The structure of $\text{Al}_9\text{Co}_2\text{Ni}$ and o- $\text{Al}_{13}\text{Co}_4$ are very different compared to the structure of Al_3Ni due to their complexity. The VDOS of $\text{Al}_9\text{Co}_2\text{Ni}$ and o- $\text{Al}_{13}\text{Co}_4$ show excess intensity in the DOS both at low and at high energies. The excess (non-acoustic) low–energy states result in higher values of the Debye–Waller factor (due to the $\frac{1}{\omega}$ factor in Eq.1.4). The character of these low–energy states is discussed in §. 3.7. There is no marked difference between the spectra of o- $\text{Al}_{13}\text{Co}_4$ and of $\text{Al}_9\text{Co}_2\text{Ni}$, except that the latter is more structured, as expected due to the higher symmetry of the structure.

3.6.2 Al_5Co_2 , and d-ANC

A similar comparison between Al_5Co_2 and d-ANC at higher x content is hampered by anomalous dynamical properties of Al_5Co_2 for both sets of potentials. For the SE potentials with short interaction cutoff radius $r_{cut}=7\text{\AA}$, the DOS exhibits a soft transverse mode (a bump near 9 meV in Fig. 3.4a) that develops into an instability at $r_{cut}=10\text{\AA}$. For GPT potentials at $r_{cut}=10\text{\AA}$, the sound velocities also exhibit a strong anisotropy and soft modes, indicating the neighborhood of the instability (the smallest transverse sound velocity was only 1290 ms^{-1}).

Table 3.2: Transverse, longitudinal and mean sound velocities for the selected Al(Co,Ni) structures in $\text{ms}^{-1} \times 10^3$, using SE and GPT pair potentials. The anisotropy is reported as $\pm(v_{max}-v_{min})/2$. Symbol “UC \times ” in the column “note” indicates the number of the images of the unit cell in a supercell used for calculation. Alternatively, the column reports variant Al occupation models relative to the full occupancy models (the case of o-Al₁₃Co₄).

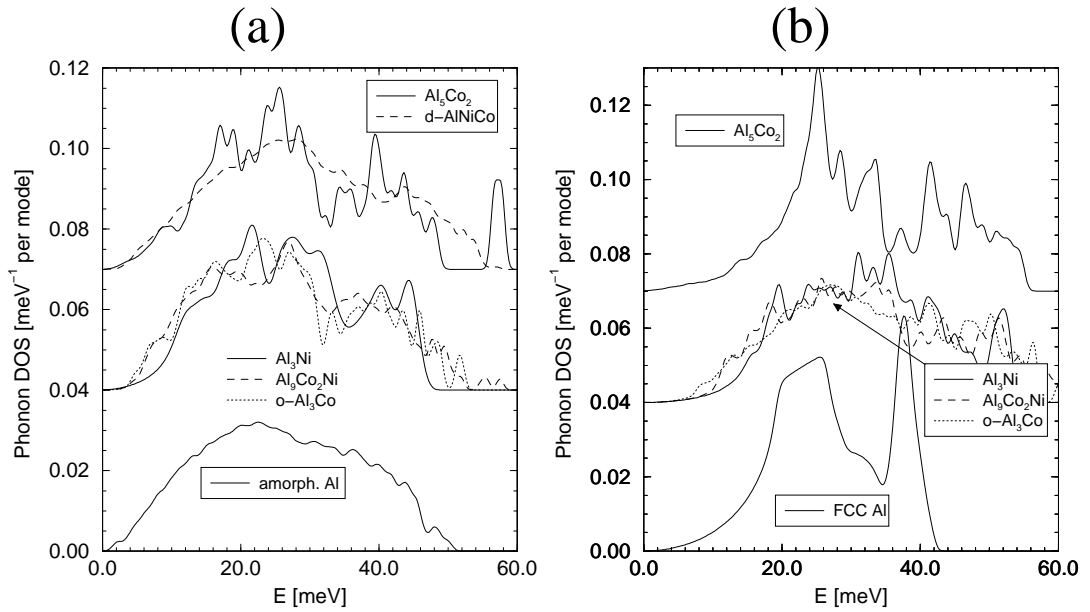
	v_T	v_L	v_s	note	Ω/Ω_{ref}
SE:					
amorph. Al	2.36 \pm 0.28	5.59 \pm 0.11	2.66	UC \times 64	
o-Al ₁₃ Co ₄	3.57 \pm 0.13	6.28 \pm 0.07	3.97		0.956
	3.47 \pm 0.15	6.12 \pm 0.39	3.86	-6 Al	1.023
	3.87 \pm 0.30	7.17 \pm 0.26	4.32		0.914
Al ₉ Co ₂ Ni	3.62 \pm 0.23	6.07 \pm 0.33	4.01		
Al ₃ Ni	3.48 \pm 1.39	5.64 \pm 1.57	3.84		
Al ₅ Co ₂	3.35 \pm 0.36	4.92 \pm 0.47	3.65	UC \times 8	
d-ANC	3.80 \pm 0.23	6.57 \pm 0.25	4.21	UC \times 4	
GPT:					
<i>fcc</i> Al	3.64 \pm 0.15	6.89 \pm 0.10	4.06		
o-Al ₁₃ Co ₄	4.21 \pm 0.20	7.96 \pm 0.74	4.96		0.956
	4.19 \pm 0.26	7.86 \pm 0.60	4.69	-6 Al	1.023
	3.56 \pm 0.21	6.42 \pm 0.21	3.96	-6 Al	1.048
Al ₉ Co ₂ Ni	4.77 \pm 0.65	8.20 \pm 0.35	5.14		
Al ₃ Ni	4.98 \pm 0.35	7.67 \pm 1.17	5.41		
Al ₅ Co ₂	3.67 \pm 1.92	6.57 \pm 2.30	4.08		

Table 3.3: Isotropic Debye-Waller factors B of Al and TM in \AA^2 , calculated from Eq. 1.6 under the SE and GPT potentials.

structure	note	SE	SE	GPT	GPT
		B_{Al}	B_{TM}	B_{Al}	B_{TM}
Al		2.47	–	0.69	–
o-Al ₁₃ Co ₄		1.05	0.46	0.54	0.32
	-6Al	1.03	0.50	0.54	0.32
	adjusted	0.78	0.39	0.64	0.42
Al ₉ Co ₂ Ni		1.01	0.44	0.54	0.28
Al ₃ Ni		0.78	0.48	0.49	0.27
Al ₅ Co ₂		0.95	0.47	0.54	0.38
d-ANC		0.92	0.42	–	–

Table 3.4: Isotropic crystallographic Debye-Waller factors for some aluminides at room temperature from diffraction refinements (we averaged Wyckoff site B factors over atomic species).

structure	$B_{Al}[\text{\AA}^2]$	$B_{TM}[\text{\AA}^2]$	source
$\alpha\text{-Al}_{13}\text{Co}_4$	1.21	0.88	[Grin et al (1994)]
$\text{Al}_9\text{Co}_2\text{Ni}$	1.41	1.03	[Grin et al (1998)]
$\text{Al}_{10}\text{Mn}_3$	1.01	0.67	[Yamamoto et al (1999)]
Al_5Co_2	0.71	0.43	[Yamamoto et al (1999)]
$\text{Al}_{13}\text{Fe}_4$	0.94	0.75	[Grin et al (1994)]
$\text{Al}_{13}(\text{CoRh})_4$	1.0	0.62	[Gotzmann (1998)]
fcc Al	0.90	–	[McDonald (1966)]

Figure 3.4: Phonon DOS of the Al_5Co_2 , Al_3Ni , $\text{Al}_9\text{Co}_2\text{Ni}$, $\alpha\text{-Al}_{13}\text{Co}_4$ and of the d-ANC model for the two sets of potentials: SE (a), and GPT (b).

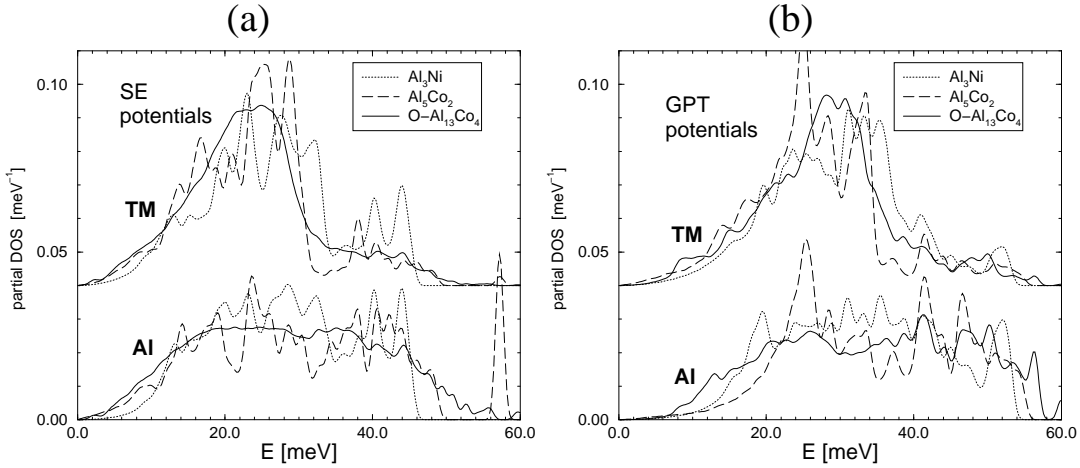


Figure 3.5: Partial Aluminum and TM phonon DOS: SE potentials (a) and GPT potentials (b).

3.6.3 Sound velocity and Debye-Waller factors

The sound velocities were experimentally determined for decagonal AlNiCo from the phonon dispersion [Dugain et al (1999)] and from acoustic spectroscopy [Chernikov et al (1998)], yielding consistently $v_T \sim 4100\text{-}4600 \text{ ms}^{-1}$, and $v_L \sim 7000 \text{ ms}^{-1}$. As can be seen in Table 3.2, these numbers are overestimated by the GPT potentials (particularly the longitudinal sound), and underestimated by SE potentials. A separate confirmation of this trend for the two sets of potentials is provided by the comparison of the Debye-Waller factors at $T=300 \text{ K}$ calculated from the dynamical matrix (Table 3.3), and obtained from the diffraction refinements (Table 3.4): the GPT potentials underestimate both the Al and TM Debye-Waller factors, while SE potentials appear to slightly overestimate B_{Al} , and underestimate B_{TM} . However, we point out that the B factors fitted from the diffraction data should be considered, at least for the complex structures, as an *upper bound* estimate, due to the coupling between partial occupancy and the thermal vibration of an atom about the equilibrium position in the diffraction-data fits. On the other hand, the B factors evaluated here are more likely the *lower bound*, since we (i) allow only for a limited relaxations of the complex structures (see the discussion of the stability in §. 3.4), and (ii) we use the phonon spectrum calculated at $T=0 \text{ K}$ with the $T=300 \text{ K}$ thermal occupation factor. In fact, the room-temperature molecular dynamics simulation discussed in §. 3.8 leads to an increased partial B_{Al} factors, while the B_{TM} is consistent with the dynamical-matrix calculation.

3.6.4 Partial Al and TM phonon DOS.

The gross features of the partial Al and Co densities of states are the same (Fig.3.5) for the two sets of pair potentials and for all investigated structures:

the Al band is broad and extends up to about 60 meV, while the TM band exhibits a rather sharp maximum below 30 meV. This leads to a GVDOS that correctly explains the difference between the experimentally determined phonon GVDOS of the d-ANC and o- $\text{Al}_{13}\text{Co}_4$ (see §. 3.6.5).

There is one apparent difference between the Al and TM partial DOS for Al_3Ni and for

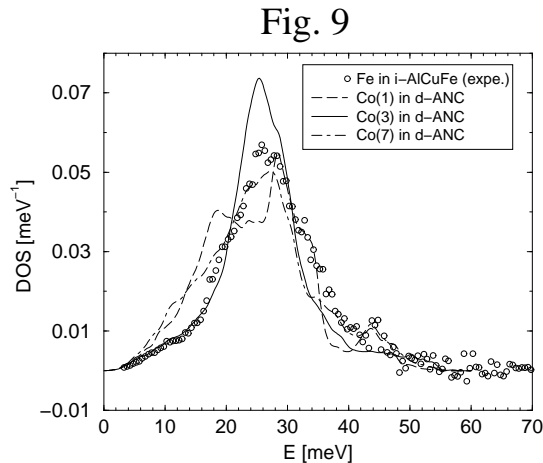


Figure 3.6: Partial Fe phonon DOS in i-AlCuFe determined experimentally [Brand et al (2000)], and local phonon DOS on three different Co sites in d-ANC model. The labels of the Co sites are explained in Fig. 3.1(e).

α -Al₁₃Co₄: while in the former case the partial DOS share many details in common (features appearing in Al partial occur also in TM partial DOS at the same energy), the wiggles in the Al and TM partial DOS lose most of the correlation in the case of α -Al₁₃Co₄. This difference is due to the fundamentally different character of the phonon eigenstates in the simple and in the complex structures (see discussion in §. 3.7): they are extended throughout the energy spectrum in Al₃Ni, and more localized in d-ANC, with enhanced localization near both the low- and the high-energy ends of the spectrum.

The calculated TM partial phonon DOS may be qualitatively compared to the recently measured partial DOS of Fe in i-AlCuFe [Brand et al (2000)]. Albeit the decagonal and icosahedral structures are different, we conjecture that due to the localization, the shape of the TM partial DOS is well described as an average over the *local* DOS on the Fe atoms, and therefore is not sensitive to the detailed structure. Secondly, the GPT theory predicts that Al-TM interactions are very similar for Co, Ni and Fe (Fig. 8 in [Moriarty and Widom (1997)]). Fig. 3.6 shows the partial Fe DOS compared to the local DOS on the three TM sites occurring in our d-ANC model. These are labeled Co(1) (atoms in the central column of the decagonal cluster, each having two neighboring TM atoms), Co(3) (with *no* TM neighbors) and Co(7) with a single TM neighbor. The effect of the neighboring TM atom is apparent: for a single neighbor, the DOS broadens (Co(7)), for two neighbors it further broadens and clearly splits. The Debye-Waller factor B is lowest for the Co(2) site ($\sim 0.37 \text{ \AA}^2$), and by some 15% higher for the other two Co sites ($\sim 0.43 \text{ \AA}^2$). The Fe partial exhibits striking resemblance to the Co(3) DOS in d-ANC with no TM neighbors. This is plausible in view of the low Fe content in i-AlCuFe ($\sim 12\%$). We speculate, that the Cu atom is acting approximately as an average Al/Co atom, as suggested by the successful Mock-ternary model of d-AlCuCo [Cockayne and Widom (1998b)].

3.6.5 Comparison with experimental GVDOS

The experimental GVDOS of decagonal Al₇₀Co₁₅Ni₁₅ [Mihalkovič et al (1996)] and the calculated (using SE potentials) GVDOS of d-ANC approximant are compared in Fig. 3.7(a). The

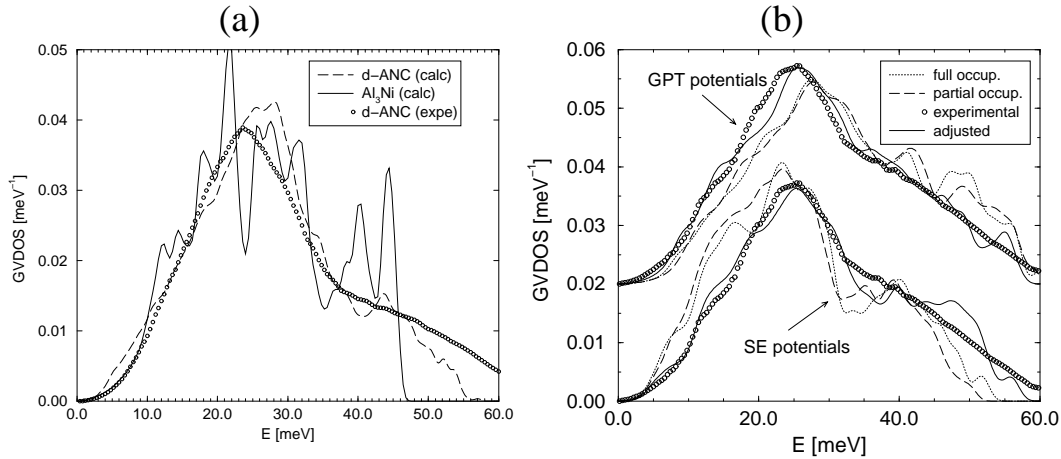


Figure 3.7: (a): Experimentally determined GVDOS of $\text{Al}_{70}\text{Ni}_{15}\text{Co}_{15}$ and calculated GVDOS of d-ANC approximant model and Al_3Ni crystal (SE potentials). (b): GVDOS of $o\text{-Al}_{13}\text{Co}_4$ with full occupancy (102 atoms in the unit cell) and with 6 Al \rightarrow vacancy substitutions for the two sets of the potentials. The data are compared to the experimentally determined phonon GVDOS of $o\text{-Al}_{13}\text{Co}_4$ at $T=300$ K. The “adjusted” GVDOS was calculated at variant atomic volume for 102-atom model (SE potentials) and 96-atom model (GPT).

character of the calculated GVDOS is determined by a broad structure-less Al band extending up to 60 meV, and by a much sharper TM band peaking at about 29 meV. The coupling to the neutrons overweights the TM contribution in the GVDOS, and, as we have seen for springs, the position of the main peak in the experimental spectrum can be clearly attributed to the TM partial DOS [Mihalkovič et al (1996)]. This peak is located at about 24 meV in the experimental GVDOS.

In the low-energy part of the spectrum, the calculated GVDOS is higher than the experimental one despite the fact, that even the experimental GVDOS has a significant excess of states in this part of the spectrum (the discussion will follow in §. 3.7) over the expected acoustic contribution derived from the experimental mean sound velocity. In both spectra, this excess is due to the localized low-energy modes.

In the figure is also superimposed the calculated GVDOS of the Al_3Ni structure (SE potentials). Surprisingly, the experimental GVDOS of d-ANC and the calculated GVDOS of Al_3Ni are in a good agreement up to at ~ 9 meV. This indirectly suggests, that the *amount* of the low-energy modes in quasicrystals – with prevalence of the localized modes over acoustic – somehow corresponds to soft modes occurring in crystalline systems with similar composition. The soft mode in Al_3Ni occurs for \mathbf{k} along (1,1,0) direction with $v_T(1,1,0)=1720 \text{ ms}^{-1}$, while for the stiffest transverse mode $v_T(0,1,0)=4360 \text{ ms}^{-1}$.

Fig. 3.7(b) shows the experimental and calculated GVDOS of $o\text{-Al}_{13}\text{Co}_4$ for the two sets of atomic interactions. We considered two variant structural models, both at the experimental volume: a full-occupancy 102-atom model, and a 96-atom model with six Al sites vacant. In the former case, the atomic volume is shrunk by a factor of 0.956 relative to the required volume at which the potentials were evaluated; in the 96 atom model, the atomic volume is expanded by factor 1.023 (see Tab. 3.1). Apparently, this $\sim 7\%$ variation of the atomic volume

does not change much the GVDOS, calculated at the fixed dimensions of the unit cell.

We also attempted to match the experimental GVDOS by varying the unit cell dimensions (and considering the full or fractional occupancy models). The results are shown in the same figure as a solid line, and denoted as “adjusted”. For the SE potentials, we used the model with full-occupancy and scaled the unit cell uniformly by a factor of 0.985³. For the GPT potentials, the best fit was obtained using the 96-atom model, with anisotropic scaling factor (0.97,1.02,1.035), for the “periodic” and the two pseudo-decagonal unit cell dimensions respectively. Here it was essential to shrink the “periodic” direction lattice parameter c in order to maintain the stability at increased lattice parameters a and b in the pseudodecagonal plane. The effect of these variations on the sound velocity is summarized in Table 3.2; for both SE and GPT interactions, they approach closer the experimentally measured values in d-ANC.

The effect of scaling the volume of the unit cell vs variation of the fractional occupancy can be most readily deduced from the SE potential data in the Table 3.2 (for the GPT potentials we scaled the unit cell volume anisotropically to avoid instability). Removing 6 Al atoms increases the relative atomic volume Ω/Ω_{ref} by nearly 7%, while the mean sound velocity softens by only 3%. On the other hand, when the unit cell is uniformly shrunk for the full occupancy model by 4.5%, the mean sound velocity hardens by nearly 9%.

One apparent difference between the calculated and experimental GVDOS is that the former exhibits many details in the curvature of the DOS, and the latter is rather smooth. While we chose to present the calculated data in a uniform way with constant resolution of 0.5 meV, the experimental resolution function rapidly increases at high energies. Secondly, our data show the spectrum of a single sample with strictly periodic boundary conditions, ignoring the disorder phenomena (fractional occupancy and related relaxations of the atomic positions). These are specifically important in the low-energy part of the spectrum.

3.7 Character of the modes

The experimental search for the vibrational properties generic or specific to quasicrystals has in the past focused on the character of the acoustic branches [Boudard et al (1995)]; Dugain et al, 1999). However, it is only recently that there is increasing evidence for non-acoustic low-energy states, that show up in the phonon DOS [Brand et al (2000), Mihalkovič et al (2000)], in excess heat capacity [Bianchi et al (1997)], or in atypical low-temperature variation of the sound velocity [Vernier et al (1993), Bert et al (2000), Sterzel et al (2000)]. The microscopic nature of such states, commonly occurring in the disordered systems, remains unclear in the quasicrystals with highly perfect long-range topological order.

The aim of the section is to demonstrate how the character of an eigenstate depends on the structure, with focus on the low-energy part of the spectrum. As an illustrative example, a comparison between the d-ANC model and the Al₃Ni structure (SE potentials), will be presented.

3.7.1 The participation ratio

The appropriate quantity revealing the character of eigenmodes is the participation ratio P_i defined for each eigenmode ω_i (Eq.2.8). For the (relatively) simple structure of Al₃Ni, the

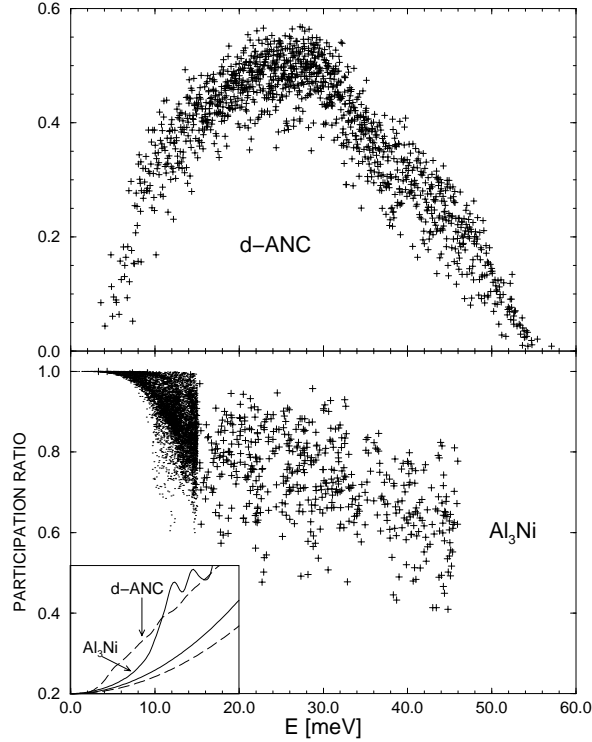


Figure 3.8: Participation ratio of d-ANC model and Al_3Ni structure (SE potentials). For clarity, $P(\omega)$ is calculated for Γ -point only (d-ANC) and for 12 k -points (Al_3Ni) (plus symbols). For the low-energy part of Al_3Ni , $P(\omega)$ is shown as dots for a densely sampled Brillouin zone. The inset shows the corresponding phonon DOS. The parabolas below the DOS curves marked by arrows are the corresponding “Debye DOS” calculated from the sound velocities v_s .

modes are purely extended up to about 5 meV, then they start to localize gradually, with the mean $P(\omega)$ decreasing approximately linearly down to ~ 0.6 near the high-energy end of the spectrum (Fig. 3.8, bottom panel). A completely different picture emerges for the model of d-ANC structure (Fig. 3.8, top panel): $P(\omega)$ falls off very quickly down to extremely low values already near 3-4 meV, then the mean $P(\omega)$ starts to increase again to its local maximum near the center of the spectrum ($P(\omega) \sim 0.5$), to fall off again down to nearly zero at the high-energy end of the spectrum. However, a feature common to both models is that the $P(\omega)$ actually behaves like a function: although there is always a spread among the P_i 's at a given ω , this spread is so small that there is never more than one characteristic $P(\omega)$. This indicates, that the DOS $D(\omega)$ corresponds to “mixed” states with more-less unique $P(\omega)$, rather than to a superposition of purely extended and purely localized modes. A similar trend is found for the phase quotient $Q(\omega)$ (Fig. 3.9) defined by:

$$Q_i = \frac{\sum_{jj'} \mathbf{u}_{ij} \cdot \mathbf{u}_{ij'}}{\sum_{jj'} |\mathbf{u}_{ij} \cdot \mathbf{u}_{ij'}|}. \quad (3.3)$$

where the sum jj' denotes all nearest-neighbour interatomic bonds, and the \mathbf{u}_{ij} refer to the displacements of the individual atom j in the eigenmode i . $Q_i \rightarrow 1$ for the acoustic modes, and $Q_i \rightarrow -1$ for optic modes with a phase shift of π on the neighbouring atoms.

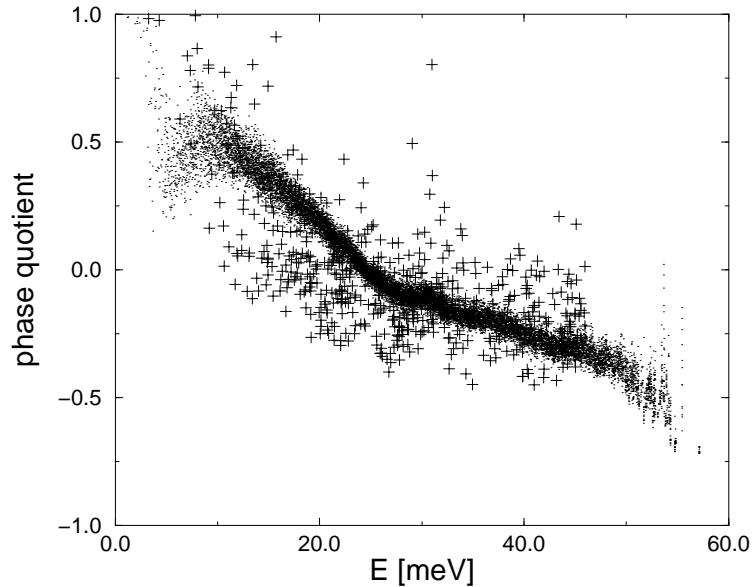


Figure 3.9: Phase quotient of d-ANC model (dots) and Al_3Ni structure (plus symbols) for SE potentials.

The phase quotient has been first proposed to characterize correlation between eigenvectors of the neighboring atoms for disordered materials [Bell and Hibbins-Butler (1975)]. For both d-ANC and Al_3Ni , there is a threshold energy of about 25 meV for the phases; below this energy, the neighboring atoms tend to vibrate in phase, above with opposite phase, with extreme values of $Q(\omega)$ at both ends of the energy spectrum. Apart from the anomaly in the case of d-ANC at low energies which can apparently be related to the low-energy localized states, the ω dependence of Q is surprisingly regular; more precisely, it appears there are two well defined slopes, above and below the threshold energy.

The localized low energy excitations provide a tentative explanation of the discrepancy between the neutron GVDOS [Mihalkovič et al (1996)] and dispersion-relation measurements [Dugain et al (1999)] in d-AlNiCo. The mean sound velocity v_s defined in Eq.(2.13) gives rise to the acoustic contribution to the phonon DOS in the long-wavelength limit (Eq. 3.2). From the phonon dispersion [Dugain et al (1999)], one obtains $v_s \sim 4.9 \times 10^3 \text{ m.s}^{-1}$; however, fitting the experimental GVDOS to Eq.3.2, results in $v_s \sim 3.1 \times 10^3 \text{ m.s}^{-1}$ (we find that at low energies, the difference between GVDOS and DOS is at most 10%) and $\beta = 2.25 \times 10^{-7}$. Thus the experimentally determined GVDOS contains a considerable excess intensity at the low energies in addition to the acoustic modes measured when determining the dispersion relation [Dugain et al (1999)].

The inset of the Fig. 3.8 (bottom panel) compares the Debye DOS calculated via Eq.3.2 with the total phonon DOS for the Al_3Ni and d-ANC structures. However, our calculation does not reproduce the ω dependence of the amount of the localized modes: as mentioned above, the GVDOS scales approximately with ω^2 , which is apparently not true in our calculation with the SE potentials. Secondly, while the acoustic signal can be clearly followed experimentally up to $E > 10 \text{ meV}$ [Dugain et al (1999)], in our calculation *all* modes rapidly localize above

~ 3 meV.

3.8 Molecular dynamics simulation

The occurrence of the phonon instability that we encountered especially with the SE potentials motivated a series of molecular dynamics cooling runs performed between the temperatures of $T=300\text{--}50$ K. An easily accessible quantity not particularly sensitive to the equilibration times is the Debye–Waller factor B^{md} defined in Eq.3.4 below and calculated via molecular dynamics simulation (MDS). This is directly comparable to the classical high–temperature approximation (Eq.3.5) of the “harmonic” Debye–Waller factor (Eq.1.6), the temperature dependence of which arises from the thermal occupation of the $T = 0$ K phonon states. At $T = 300$ K, the classical approximation to the Debye–Waller factor is by 4–5% smaller than the accurate quantum-mechanics result.

For these calculations, we employed the standard Verlet algorithm in a microcanonical NVT ensemble. Typically, we took supercells with about 400 atoms in the periodic cell, and used two different MD schedules, aimed at different goals.

3.8.1 Temperature dependence of the DW factor.

Cooling was done from $T=300\text{K}$ down to 50K in steps of 50K , with 500 ps equilibration time at each temperature, and consecutive 500 ps measurement time (timestep $\Delta t=10^{-14}\text{s}$). For each individual atom j , we took time-averages $\langle u_{j\nu}^2 \rangle - \langle u_{j\nu} \rangle^2$, where ν denotes Cartesian coordinates. These were then averaged over all atoms of a given type α to obtain the “crystallographic” Debye–Waller factor B_α^{md} by molecular dynamics (md)

$$B_\alpha^{md} = \frac{8\pi^2}{3N_\alpha} \sum_{j=\alpha} \langle u_{j\nu}^2 \rangle - \langle u_{j\nu} \rangle^2 \quad (3.4)$$

where summation j is through atoms α , and the brackets mean the time average. The formula is only valid in the absence of the diffusion. Some large values of the DW factors even at room temperature are due to a subset of Al atoms, for which Eq.3.4 cannot be applied.

The B^{md} can be compared directly with B defined by Eqs. 1.4 and 1.6 in the *classical* high–temperature approximation, in which the occupation factor can be approximated by:

$$n(\omega, T) + \frac{1}{2} \approx \frac{k_B T}{\hbar\omega}. \quad (3.5)$$

It should be noted, that within this light temperature approximation any deviations from the linear T –dependence of $B(T)$ may only be due to anharmonic effects. Moreover, since we keep the volume of the unit cell fixed, these effects are also *not* quasiharmonic, which is usually a leading correction to the harmonic temperature dependence of the Debye–Waller factor.

In Fig.3.10 we show three patterns of the $B_{Al}^{md}(T)$ behaviour for Al atoms (the TM partials turn out to behave normally in all cases): $B_{Al}^{md} \sim B_{Al}$ (classical approximation to B) for Al_3Ni structure, $B_{Al}^{md} < B_{Al}$ for Al_5Co_2 , and $B_{Al}^{md} > B_{Al}$ for d-ANC model. While the Al_3Ni shows no sign of instability from the phonon spectrum calculation and $B_{Al}^{md}(T)$ is accurately described by the classical approximation, MDS (Molecular Dynamic Simulation) annealing together with the supercell model was necessary to avoid the phonon instability in Al_5Co_2 . Interestingly, above

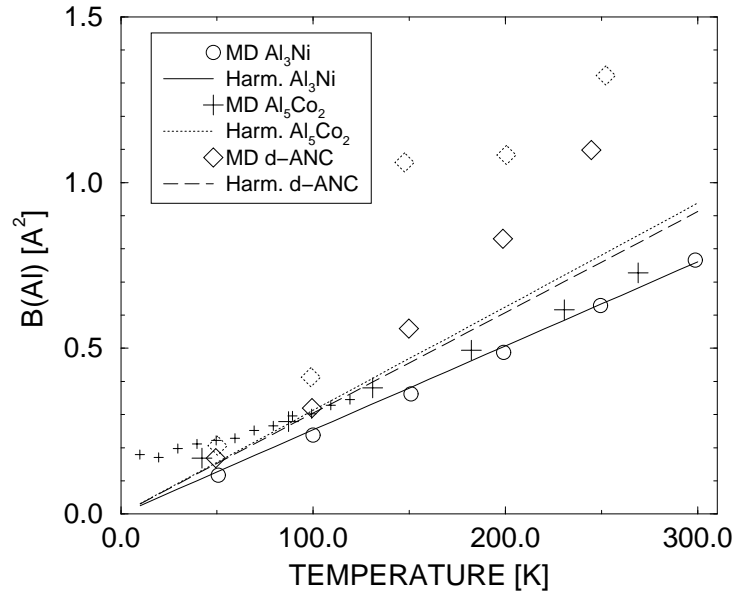


Figure 3.10: Temperature dependence of the partial Al Debye–Waller factor obtained from molecular dynamics cooling runs from $T=300$ K down to 50 K (symbols) (using SE Potentials). The classical harmonic approximation of the phonon Debye–Waller factor is shown as lines.

$T=150$ K the $B_{Al}^{md}(T)$ of Al_5Co_2 is linear and very close to that of Al_3Ni , but below $T=150$ K it exhibits an excess fluctuation of $\langle u^2 \rangle$ (ie, when $E_{kin} = E_p = \frac{3}{2}k_B T > 25$ meV). We conjecture that is due to a peculiar anharmonicity of the potential energy surface near its minimum; this has been confirmed by a longer cooling run from $T=120$ K down to 10 K (smaller plus symbols in the figure). Thus we expect that the B_{Al} value at $T=300$ K reported in Tab. 3.3 for Al_5Co_2 is overestimated.

On the other hand, $B_{Al}^{md}(T)$ of d-ANC shows an excess, increasing with the temperature, compared to the normal harmonic behaviour. This excess is due to the degeneracy of the equilibrium positions of some Al sites, in particular Al(4) (see Fig. 3.1(e,f)) with $B_{Al(4)}^{md} \sim 2.6 \text{ \AA}^2$ at $T=300$ K. These sites form implausibly short bonds of ~ 0.18 nm in the idealized model, and the degeneracy is related to the many energetically nearly equivalent ways of breaking the decagonal symmetry of the cluster as the short bond relaxes under the action of forces. At room temperature, it is difficult to check whether the large calculated B_{Al}^{md} does not already incorporate an excess due to the onset of self-diffusion; a 10 times longer run confirmed that the B_{Al} evolves with time (dotted diamonds in the figure). This matter is further discussed in the following section.

3.8.2 High-temperature stability and atomic configurations.

We reduced the timestep by a factor 2, and after the 100 ps equilibration period we recorded 500 atomic configurations in 1 ps time intervals. The configurations were used to obtain projected density maps.

We performed an additional MD annealing run at $T=1000$ K for the d-ANC model with

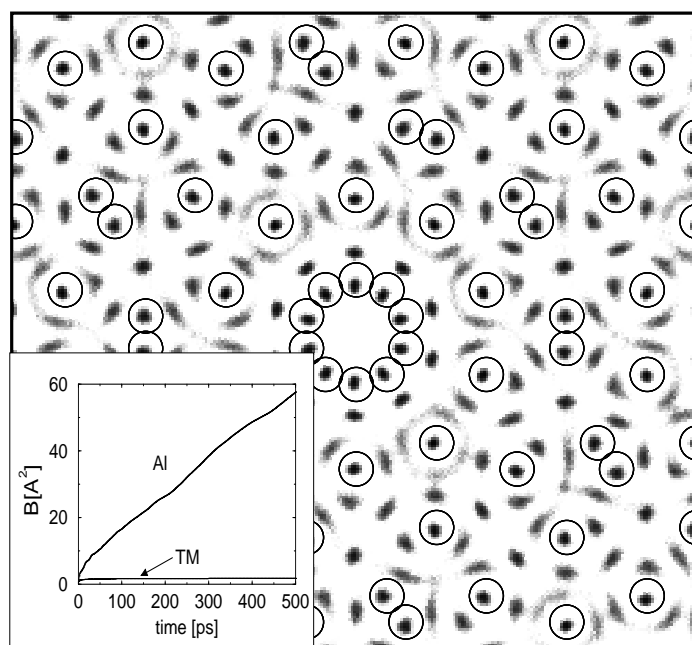


Figure 3.11: Atomic density map of d-ANC model from MD annealing at $T=1000$ K, projected along the pseudodecagonal axis (SE potentials, 500 samples). Large circles mark idealized positions of the Co atoms.

the schedule described in §. 3.8. We recorded the time evolution of $\langle u^2 \rangle$, and projected the atomic configurations into a 250×250 pixels map perpendicular to the “periodic” axis. Figure 3.11 shows a clear evidence that the strongly localized low-energy states found in the $T=0$ K harmonic analysis are not precursors of an instability: the structure is clearly stable due to the rigidity of the network of TM atoms, that can be ascribed to the strong nearest-neighbor interaction between Al-TM pairs. Interestingly, the empty position projected on the center of the columnar cluster, apparently capable of accomodating an atom, remains unoccupied throughout the simulation run, probably due to the strong binding with the Al(2) atoms in the surrounding 10-fold ring.

On the other hand, the typical high-temperature behaviour of Al atoms is represented by Al(2) and Al(4) between the extrema atoms (see Fig. 3.1: Al(2) has a well defined equilibrium position, while Al(4) shows up in the MD map as a streaks). The inset shows the time evolution of the Debye-Waller factor B ; the slope is approximately linear, indicating a self-diffusion of Al.

Chapter 4

Frequency shifts

Experimental investigations showed that the GVDOS of quasicrystalline alloys (d-AlNiCo, d-AlCuCo, and i-AlPdMg, Fig.4.1) shift to lower energies when the temperature is increased. Investigations of the frequency shift using a model of d-AlNiCo and some related crystalline phases are presented in this chapter.

First, a program based on the Monte-Carlo method to calculate the frequency shift due to a change in temperature is introduced assuming that the relationship between the DOS at different temperatures can be expressed in terms of frequency shifts of the phonon modes. Then the analysis of the experimentally measured temperature dependence of the phonon DOS in d-AlNiCo [Dugain et al (1997)] in the range 300–1100K are presented. Finally, the second part of this chapter investigates the relation between the frequency shift and the character of the modes.

4.1 Introduction

From experimental observations and theoretical calculations it turns out that quasicrystals are very close in energy to other structures. However it seems that high temperatures favors the stability of quasicrystals over competing crystalline phases. As the configurational entropy was one of the extensively studied energy stabilization scenarios, these remarks give enough motivation to study the lattice dynamics at high temperature and pick up their role in the stabilization of quasicrystalline phases.

Experimentally, extensive investigations were devoted to the lattice dynamics in quasicrystals, and for two prominent phases (i-AlPdMn: [Suck (1993a, 1997)]; d-AlNiCo: [Mihalkovič et al (1996), Dugain et al (1997)]) the neutron-weighted phonon density of states (GVDOS) was measured up to $T \sim 1100\text{K}$ [Suck et al (1997), Dugain et al (1997)]

With increasing temperature the eigenmodes energies shift systematically to lower values, while the general shape of the GVDOS remains the same in both cases in this range of temperatures (Fig.4.1).

The shift of the GVDOS is equivalent to a shift of the frequencies. It is more interesting to calculate the frequency shift $\frac{\Delta\omega}{\omega}$ since one can deduce from this quantity the *Grüneisen*

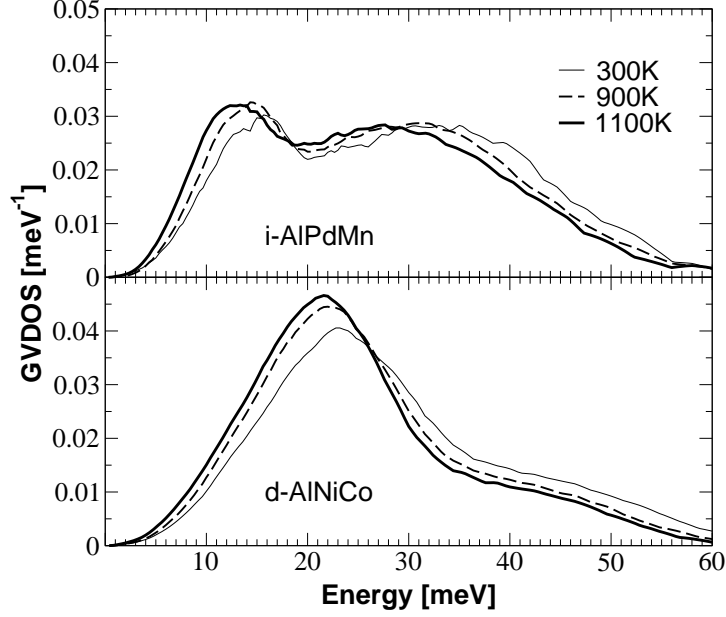


Figure 4.1: Experimental GVDOS at three different temperatures for d-AlNiCo and i-AlPdMn, there is a shift toward low frequencies at high temperatures[Suck et al, 1997; Dugain et al,1997].

parameter, which is defined for an eigenmode i by:

$$\gamma_i = -\frac{\partial \log(\omega_i)}{\partial \log V} \quad (4.1)$$

where V is the volume and ω_i the eigenfrequency of the eigenmode i .

We define also the overall *Grüneisen parameter*:

$$\gamma = \frac{\sum_i \gamma_i c_i}{\sum_i c_i} \quad (4.2)$$

where c_i is the contribution of the mode i to the specific heat.

In general for crystals $\gamma \sim 1$, and it is temperature independent. Large experimental values of averaged *Grüneisen parameter* were reported for glasses at temperatures below 1K [White et al (1975), Saunders et al (1996)], with $|\gamma| > 10$. In parallel theoretical investigations found large values for γ at low frequencies, and observed a large spread of γ in this region, which they claimed to be due to “resonant modes” which are modes with a small participation ratio due to some special structural imperfections at which they have large amplitudes. From these results, it seems that the Grüneisen parameter is sensitive to the details of structure.

4.2 Monte Carlo approach to the reconstruction of the frequency shifts

There is no direct way to derive the frequency shift of an individual eigenmode from the knowledge of the GVDOS at two different temperatures. For the sake of simplicity we assume that the relationship between two GVDOS at two different temperatures can be expressed by the frequency shifts of the phonon modes.

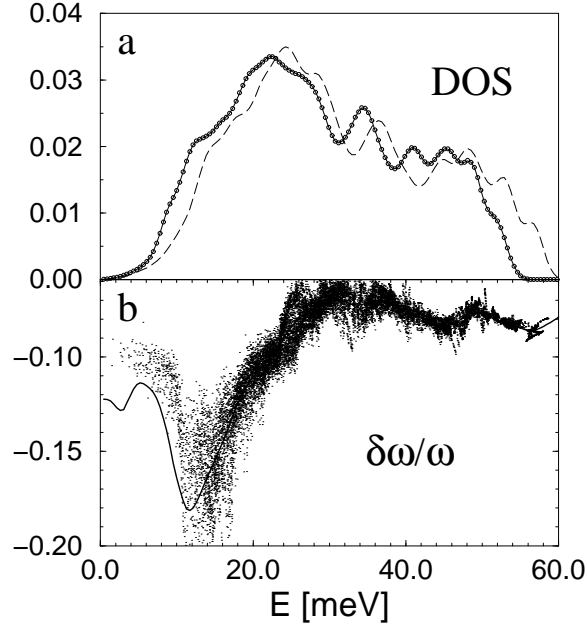


Figure 4.2: Top(a): VDOS of the trial model calculated at two different volumes (solid and dashed line). Bottom(b): frequency shifts calculated for each eigenfrequency at the two volumes (points) and by the Monte Carlo technique (solid line).

For this reason a Monte-Carlo method was developed to extract the frequency shift $\Delta\omega(\omega)$ from the GVDOS at two different temperatures G_{T_0} and G_T . A statistical relation between the two densities of states was employed via:

$$D_{T_0}(\omega_j) = \sum_i D_T(\omega_i) \times \epsilon(\omega_j - \omega_i - \Delta\omega_i) \quad (4.3)$$

where $j(i)$ labels the j -th (i -th) ω -bin of the D_{T_0} (D_T) and ϵ is a resolution function. The above equation embodies the essential assumption that all eigenmodes contributing to the interval ω_i shift uniformly. The shifts $\Delta\omega_i$ are fitted by the Metropolis Monte Carlo (MMC) method: initializing $\Delta\omega_i = 0$ for all i , a randomly selected ω_i is shifted by a fixed amount $\delta\omega$ in a randomly chosen direction, thereby modifying $D_{fit}(\omega)$ which substitutes for the $D_{T_0}(\omega_j)$ at the left-hand side of Eq. 4.3. In MMC annealing with a slowly-cooling schedule we minimized the quantity

$$\chi^2 = \sum_j w_j (D_{T_0} - D_{fit})^2 + \lambda (p_j^+ \log p_j^+ + p_j^- \log p_j^-) \quad (4.4)$$

where w_j is an ω -dependent weighting factor, and

$$p_j^\pm = (\omega_{j\pm 1} - \omega_j) / (\omega_{j+1} - \omega_{j-1}). \quad (4.5)$$

The role of the second term in Eq. 4.4 is to balance the accuracy of the fit with the requirement of maximal uniformity of the shift distribution (via the coefficient λ), as in the maximum-entropy approach, successfully used in a wide area of applications. We find that tuning the parameter λ is essential for avoiding local minima in χ^2 which occur easily at a price of sharp and improbable irregularities in the frequency distribution.

In order to test the physical plausibility of the method, we diagonalize the dynamical matrix of the structure model at two different volumes. In Fig.4.2a, we show the resulting phonon DOS at the atomic density $\rho = 70nm^{-3}$ (D_{T_0} , dashed line) and after the volume has been rescaled by factor 1.04^3 (D_T , full line). Small circles correspond to the D_{fit} . The nearly perfect agreement with the D_{T_0} demonstrates the successful convergence of the MMC annealing. This is a reasonable test, because diffraction experiments on $d-AlNiCo$ have shown that the largest part of the change of the GVDOS (if not all) can be attributed to the anharmonic expansion of the alloy with increasing temperature [Dugain et al (1997)]. In Fig.4.2b, we plot the calculated frequency shifts $\delta\omega/\omega$ (thick line), together with the ω -shifts of each eigenmode, obtained by comparing the eigenfrequencies resulting from the diagonalization of the dynamical matrix for the two volumes. Albeit there is an apparent spread of the actual shifts, the reconstructed uniform distribution of the shifts captures correctly even fine details of the *mean* frequency shift at given ω , perhaps with the exception of the low-energy region. This misfit is due to the preset (Gaussian) convolution of the eigenfrequency distribution, which suppressed sharp feature (an optic mode) near 14meV.

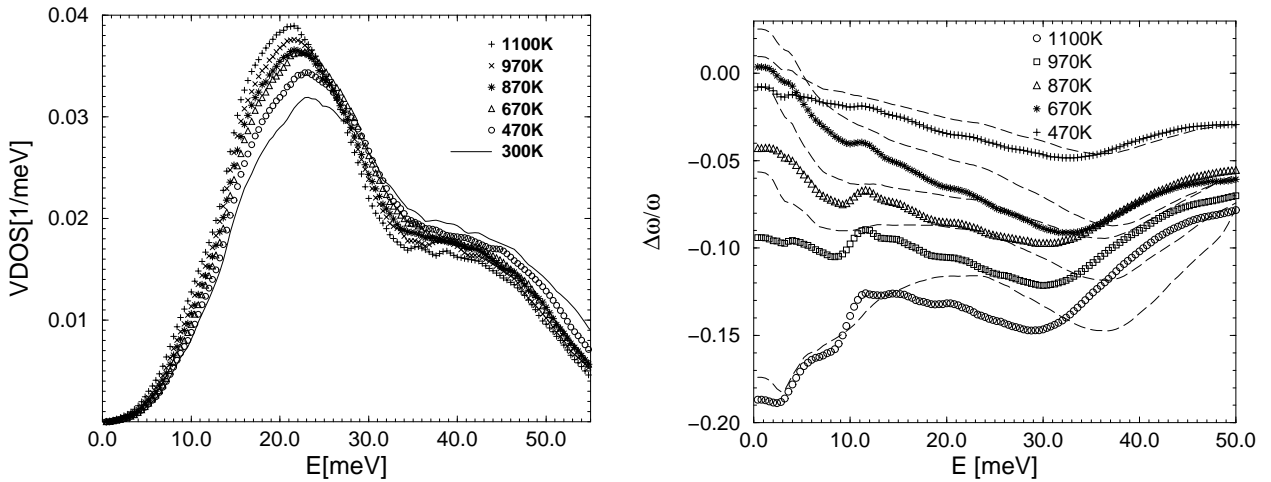


Figure 4.3: (*left*): The reconstructed VDOS as function of temperature. (*right*): The relative frequency shifts.

4.3 Reconstruction of the VDOS and frequency shifts

The experimentally measured temperature dependence of the GVDOS in $d-AlNiCo$ at 6 temperatures (300K, 470K, 670K, 870K, 970K and 1100K) was reported in [Dugain et al (1997)] (see Fig.4.1). Here, we go beyond the original work in that we (i) reconstruct the VDOS from the GVDOS using a spring model (the same as in Chap.2) and the atomic structure model described in Chap.2, and (ii) determine the temperature-dependent frequency shifts using the Monte Carlo method described in the previous section.

The GVDOS is implicitly temperature-dependent via the Debye-Waller factor e^{-2W_α} (see Eq.1.3). The room temperature GVDOS, serves as a reference spectrum ($D_{T_0}(\omega)$ in Eq. 4.3). In the MMC simulation, we applied identical frequency shifts to both partials $g_\alpha(\omega)$, and used Eq. 1.3 with $G(\omega)$ substituting for $D(\omega)$ in Eq. 4.3. In each MC step, the new $G(\omega)$ was in fact

calculated iteratively, since the Debye-Waller factor is implicitly dependent on the frequency distribution.

The assumption of the identical frequency shifts for g_{Al} and g_{TM} at a given ω allows us to reconstruct the temperature-dependence of the total VDOS (Fig. 3.4). We think that this assumption is not stronger than the assumption assigning identical frequency shifts to all modes from an interval $\Delta\omega$, embodied in our Monte Carlo method (§.4.2), because the TM atom vibrations do not show any tendency to localization.

4.4 Frequency shift and Grüneisen parameter from the experimental GDVOS

In Fig.4.3, we show the frequency shifts $\delta\omega/\omega$ for the five temperatures 470K–1100K, as determined by the Monte Carlo method and using the experimental GDVOS and the reconstructed VDOS.

Besides the broad minimum near 30meV, the most remarkable feature in the pattern of the frequency shifts is the crossover developing with increasing temperature at about 15meV.

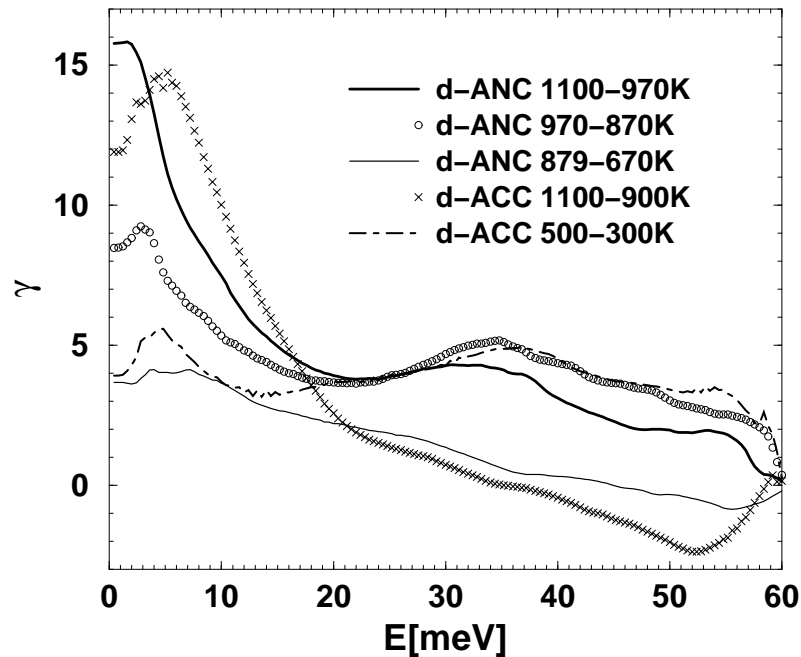


Figure 4.4: Grüneisen parameter calculated from the frequency shifts using the experimental GDVOS for d-AlNiCo and d-AlCuCo.

Using the volume-expansion data [Dugain et al (1997)] obtained by fitting temperature dependent shifts of the diffraction peak positions (for d-AlNiCo the atomic volume expands by about 0.5% at T=470K, and by 3.5% at T=1100K, relative to the T=300K volume), The Grüneisen parameter for a frequency ω_i is:

$$\gamma_i = -\frac{V d\omega_i}{\omega_i dV} \quad (4.6)$$

The *Grüneisen parameter* is shown in Fig. 4.4 for d-AlNiCo and d-AlCuCo by using the relative frequency shifts calculated from experimental GVDOS. For the low energy part we observe a strong temperature dependence of γ for the two alloys varying from ~ 2.0 at low temperature to ~ 16.0 at $T=1100\text{K}$. While this dependence is considerably weaker for high energy edge. Albeit it is difficult to estimate the error bars of the data due to the: (i) self-consistent iterative subtraction of the strongly temperature dependent multi-phonon contribution, (ii) the use of the GVDOS instead of the VDOS, and (iii) the application of same relative frequency shift assigned to all eigenfrequencies from an $\delta\omega=0.4$ meV intervals. one can speculate, that the anomalously large frequency shifts at low frequencies indicates, that a fraction of the modes have non-acoustic character, in agreement with the observation, that the apparent mean sound velocity fitted from the GVDOS is appreciably smaller than the actual mean sound velocity (see previous chapter).

4.5 The Grüneisen parameter for Al_3Ni and $\text{Al}_{13}\text{Co}_4$

The calculated γ for d-AlCoNi is strongly temperature dependent (Fig. 4.4), with a maximum at low frequencies which develops and shifts to lower frequencies with increasing temperature. The calculated mean value is also temperature dependent, at $T\sim 1000\text{K}$ $\gamma\sim 4.3$ and at $T\sim 700\text{K}$, $\gamma\sim 1.7$ which is close to the value calculated using the bulk modulus:

$$\gamma = \frac{3B\alpha}{C_v} \approx 1.60 \quad (4.7)$$

where α is the coefficient of thermal expansion, B the bulk modulus, and C_v the specific heat at constant volume.

In bulk moduli experiment, only long-wavelength modes are considered thus the difference between the value of γ obtained by Eq 4.7 and by the MC method at high temperature is probably due to the contribution of non extended modes to the frequency shifts and hence to the Grüneisen parameter. The main problem we face when we work with quasicrystals is the modeling of the structure. Even if an important progress was achieved in general, many doubts remain concerning the position of the atoms and their chemical ordering. We cannot prevent the effect of these uncertainties, and erroneous results can be obtained. Therefore, in this study, we preferred to use well known structures, where all the atomic positions are precisely defined. We use two crystalline structures: the orthorhombic (Al_3Ni) and the orthorhombic $\text{Al}_{13}\text{Co}_4$ [Grin et al (1994)], which is a complex structure, approximant to the decagonal AlNiCo quasicrystal. For the interactions model we use here the semi empirical pair potentials (SE) derived by Phillips et al [Phillips et al (1994)]. Since these pair potentials are calculated at a fixed composition (here 25 at% transition metal), instead of the 102 atoms per unit cell for $\text{Al}_{13}\text{Co}_4$ which has $\sim 23.53\text{at\%}$ TM, we reduce the number of aluminum atoms to have 25at% TM. This is achieved by relaxing the structure under the pair potentials and removing at each time the aluminum atom with the highest energy until only 96 atoms per unit cell remain. We used also the springs model used in Chap.2 for o- $\text{Al}_{13}\text{Co}_4$ as input for the interaction model, the reason of using this model is to select the structural effect on the frequency shift. To simulate the volume expansion due to the temperature, we make a small change in the volume at two different atomic volumes (V_1 , and V_2), assuming that the main effect of temperature on the

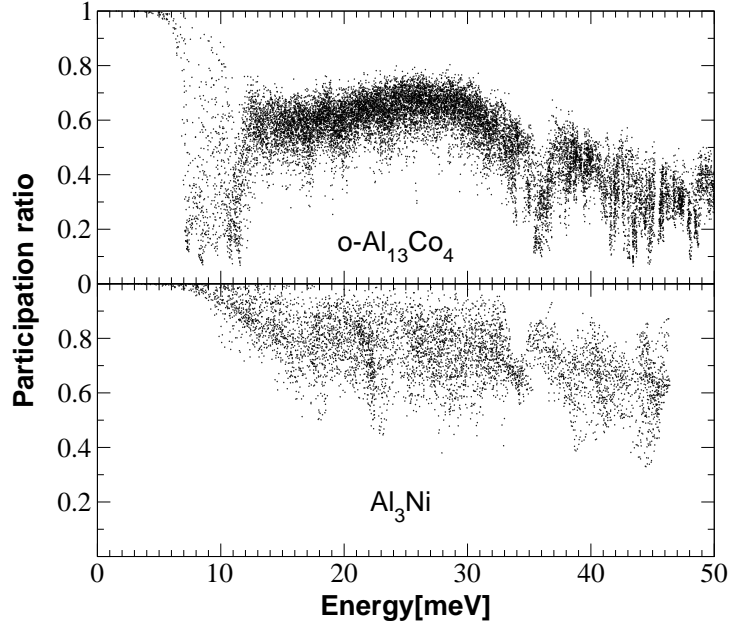


Figure 4.5: Participation ratio of $\text{Al}_{13}\text{Co}_4$ and Al_3Ni at V_1 obtained by using pair potential.

lattice is a change in the interatomic distances. $V_1 = 14.5\text{\AA}^3/\text{atom}$, is the experimental volume at room temperature of Al_3Ni . To simulate a higher temperature, we take $V_2 = 15.0\text{\AA}^3/\text{atom}$. Using the SE pair potentials and the structure models presented in 2.4.1, we calculate the eigenfrequencies and the eigenvectors in the harmonic approximation by direct diagonalization of the dynamical matrix. From the eigenfrequencies, we calculate the frequency shifts, and the *Grüneisen parameter* at the two different volumes.

Fig. 4.6 shows the γ obtained using the pair potentials (top) and the spring model (bottom). For the pair potential, there many negative values at very low energies ($\hbar\omega < 5$ meV). These negative γ indicate the instability of these structures around these volumes (V_1 and V_2), which are most likely due to a shelf-like feature at the typical nearest-neighbor Al-Al distance. The negative values are not present in the case of $\text{o-Al}_{13}\text{Co}_4$ at V_2 . This problem is not seen for the calculations with springs, where the structures are supposed to be stable. At high energies ($\hbar\omega > 15\text{meV}$), γ is almost constant with $\gamma \sim 2.0$ (pair potentials) and ~ 1.5 (springs).

At low energies ($\hbar\omega < 15\text{meV}$), there is a fundamental difference between the two crystal structures. While we notice a spread of γ for both structures and interaction models, and at the two volumes, only the *Grüneisen parameter* for $\text{o-Al}_{13}\text{Co}_4$ reaches a maximum with springs at V_1 (at $\hbar\omega \approx 12$ meV) and V_2 ($\hbar\omega \approx 9$ meV), and using pair potentials at V_2 ($\hbar\omega \approx 8$ meV). This results are in agreement with the experimental results shown at the beginning of this chapter, and indicate a fundamental difference between the behavior of γ for complex structures represented by the $\text{oAl}_{13}\text{Co}_4$ phase, and simple crystalline phases represented by Al_3Ni . Finally at very low energies ($\hbar\omega < 5$ meV) where there are only acoustic modes the *Grüneisen parameter* has higher values than the high energy case, except for Al_3Ni with pair potentials where the structural instability causes negative values of γ .

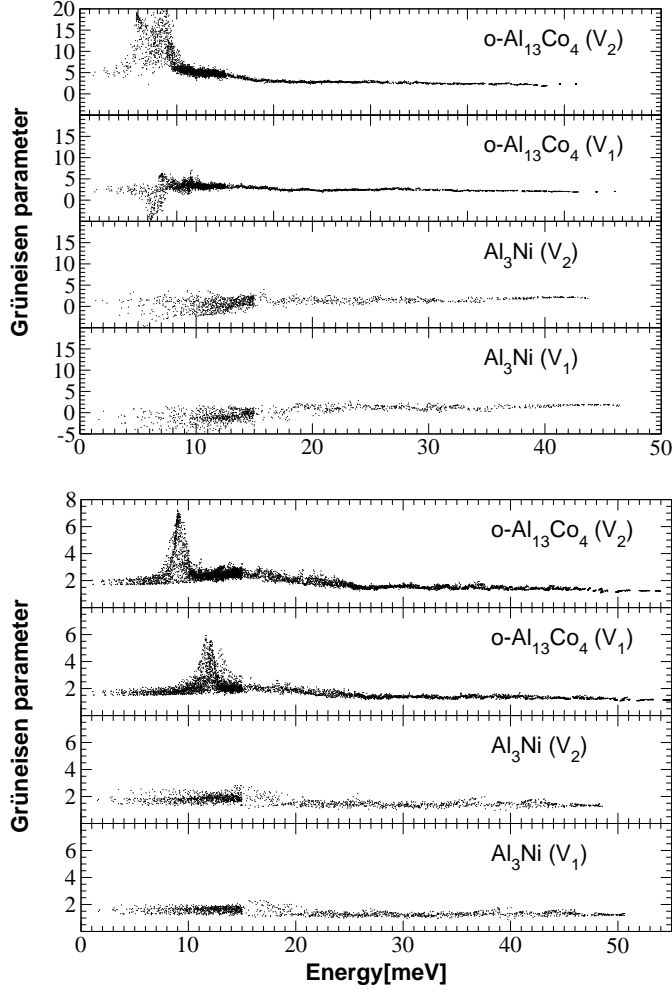


Figure 4.6: top: Grüneisen parameter calculated from the eigenfrequencies using the pair potentials. The negative values observed at V_1 calculations are caused by the structural instability under the pair potentials which is due to the peculiar shape of the Al-Al first neighbors interactions, and could also be due to the non inclusion of the many body terms in the potential energy. bottom: Grüneisen parameter calculated from the eigenfrequencies using a spring model.

4.6 The Grüneisen parameter and the character of the modes

From the discussion above we can distinguish three groups of modes with distinct behavior: *(i)* acoustical modes, they have relatively large values of γ which are weakly volume dependent. *(ii)* High frequency modes, with constant and weakly volume dependent γ . *(iii)* Low frequency modes with large and volume dependent γ . This latter group is present only in the case of $\text{Al}_{13}\text{Co}_4$. To characterize these modes, we use the *participation ratio* P defined by Eq.2.8. For the Al_3Ni , the modes are in general extended, but at high frequencies we find modes with lower participation. For $\text{Al}_{13}\text{Co}_4$, most of the modes are neither localized nor extended. At low frequencies there are acoustic modes which are extended, and a group of modes with very small participation ratio ($P < 0.2$). As have been seen in §2.4.5, we checked the nature of these mode and it was found that these are quasi-localized modes.

In Fig. 4.7 we plot the Grüneisen parameter as function of the participation ratio for Al_3Ni

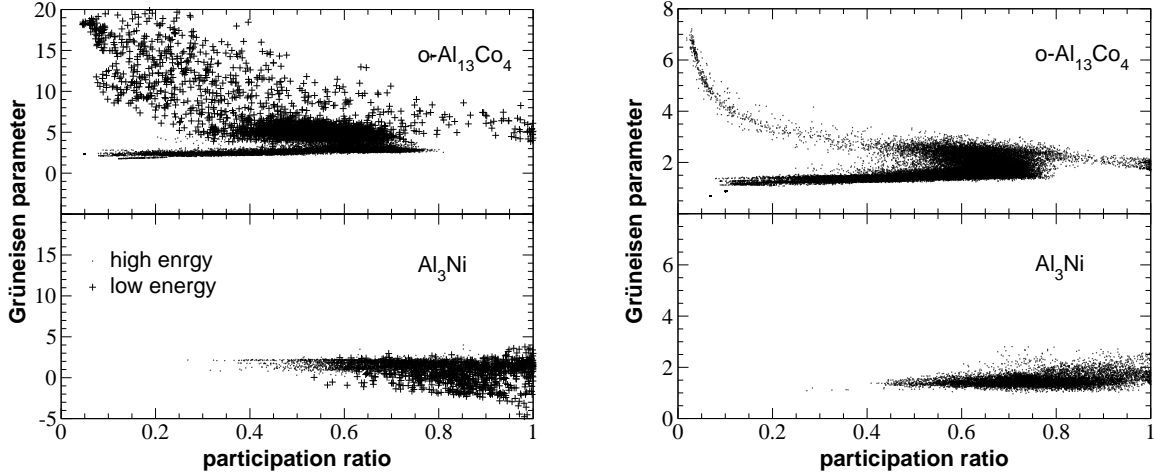


Figure 4.7: left: Grüneisen parameter versus participation ratio calculated from the eigenfrequencies using the pair potentials and at volume V_2 . right: Grüneisen parameter versus participation ratio calculated separately for each eigenmode using the spring model and at the volume V_2 .

and $\text{Al}_{13}\text{Co}_4$ at V_2 respectively using pair potentials and springs. We distinguish between modes with $\hbar\omega < 15$ meV (crosses) and modes with $\hbar\omega > 15$ meV (dots). For both structures the high frequency modes form a separate branch with a constant $\gamma \sim 2.0$ (pair potentials) and ~ 1.5 (springs). For $\text{Al}_{13}\text{Co}_4$, the low frequency modes have a well defined behavior especially for springs. They have larger γ than the high frequency modes, and these values increase as the participation ratio of the modes decreases creating a separate branch of modes, with largest values of γ for the groups of low frequency quasi-localized modes.

4.7 Conclusion

The present study shows that the complex structure $o\text{-Al}_{13}\text{Co}_4$, d-ANC is distinguished by the presence of a group of quasi-localized modes which do have large temperature dependent Grüneisen parameter. These modes are possibly similar to the “resonant modes” in glasses which are also responsible for similar phenomena [Fabian and Allen (1997)] or to the energy modes discovered in glassy alloys [Suck and Rudin (1983), Suck et al (1987)]. The Grüneisen parameter calculated for $o\text{-Al}_{13}\text{Co}_4$ from eigenfrequencies and for d-AlNiCo, i-AlPDMn, and d-AlCuCo using the experimental GVDOS are qualitatively similar. From what preceded, we can argue that these high γ values at high temperatures are due to the low energy “resonant modes”. It has been shown repeatedly that such modes effectively exist in quasicrystal phases [Elhor et al (2000), Brand et al (2000)].

Chapter 5

Vibrational entropy

It has been recognized a long time ago that the vibrational entropy could affect the order-disorder transition [Booth and Rowlinson (1955), Wojtowicz and Kirkwood (1960), Moraitis and Gautier (1977), Bakker (1982), Mathew et al (1983), and Bakker and Tuijn (1986)]. However in the explanation of the thermodynamic stabilities, the vibrational entropy was always neglected relatively to the configurational entropy. Only recently, some studies have been performed to measure [Anthony et al (1993), Nagel et al (1995), Fultz et al (1995), Nagel and Fultz (1997)] or to calculate the difference in the vibrational entropy between different phases [Sanchez et al (1991), Mohri et al (1993), Clark and Ackland (1993), Garbulsky and Ceder (1994)]. It was found for example [Anthony et al (1993)] that the difference of the vibrational entropy between the disordered and ordered Ni₃Al phases at high temperatures is of the order of 0.3k_B/atom. This is comparable to the difference between the configurational entropies (0.56k_B/atom) and large enough to affect substantially the relative thermodynamic stabilities.

In this chapter, the phonon DOS at high temperatures calculated in the Chap. 3 are first used to identify the individual thermal contributions to the vibrational entropy, and precisely, using the spring model for the d-AlNiCo structure, the vibrational entropy due to the shift of the phonon DOS at high temperatures is estimated, which cannot be explained only by the thermal expansion of the volume. In the second part of this chapter, the variety of structures occurring near 25% in the Al-Co phase diagram, and their subtle energetic balance motivates an investigation of the importance of the vibrational entropy for the finite temperature stability.

5.1 Temperature dependence of the vibrational entropy of d-AlNiCo

The vibrational entropy can be provided in the quasiharmonic approximation by the phonon DOS $g_{T_i,V}$ [Eriksson et al (1992), Bogdanoff and Fultz (2001)]:

$$S_{vib}(V, T_i, T_j) = -3k_B \int_0^{\infty} g_{T_i,V}(E) [(n_E + 1) \ln(n_E + 1) - n_E \ln(n_E)] dE \quad (5.1)$$

where n_E is the Bose-Einstein distribution at temperature T_j , and $g_{T_i,V}$ is the phonon DOS at temperature T_i and volume V .

The vibrational entropy $S_{vib}(V, T, T)$ can be written as a sum of a harmonic term S_{har} and an anharmonic term S_{anh} :

$$S_{vib}(V, T, T) = S_{har} + S_{anh} \quad (5.2)$$

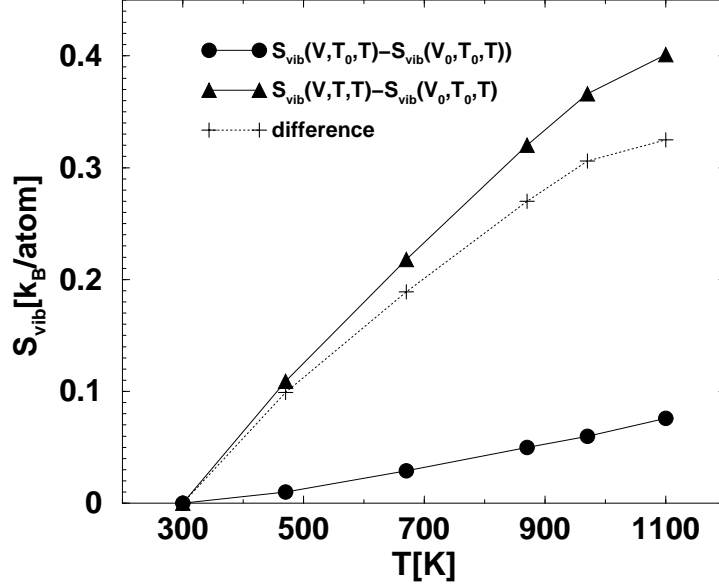


Figure 5.1: Anharmonic entropy contribution. Triangles are the anharmonic entropy contribution calculated using the recovered phonon DOS of the previous chapter. Circles are the anharmonic contribution calculated using the spring model of the d-AlNiCo structure at volumes given by the experimental thermal expansion

S_{har} originates in that part of the phonon DOS, which does not change with temperature:

$$S_{har} = S_{vib}(V_0, T_0, T) \quad (5.3)$$

where V_0 and T_0 are the reference volume and temperature. which are in our case taken at 300K.

S_{anh} is the anharmonic term which originates in the temperature dependence of the phonon DOS, and hence is due to the frequency shift.

$$S_{anh} = S_{vib}(V, T, T) - S_{vib}(V_0, T_0, T) = S_{vib}^{\Delta V, \Delta T} \quad (5.4)$$

In this section, the anharmonic entropy is estimated for d-AlNiCo using the recovered phonon DOS of Chap. 3. S_{anh} is shown in Fig. 5.1 for a set of temperatures (300-1100K). The temperature dependence of S_{anh} is almost linear, and reaches relatively large values at high temperature ($S_{anh} \approx 0.401 k_B/atom$ at $T=1100K$). The figure shows also the vibrational entropic term:

$$S_{vib}^{\Delta V} = S_{vib}(V_1, T_0, T_1) - S_{vib}(V_0, T_0, T_1) \quad (5.5)$$

The entropies on the right hand side were calculated using the spring model of the d-AlNiCo structure discussed in the first chapter, and using atomic volumes given by the experimental thermal expansion (Fig. 5.2), thus the effect from the volume expansion only. The same linear temperature dependence is also observed for $S_{vib}^{\Delta V}$, but this time the values are much lower. The discrepancy between $S_{vib}^{\Delta V, \Delta T}$ and $S_{vib}^{\Delta V}$, indicates the existence of an explicit "temperature" term for the vibrational entropy which is due to a shift of the phonon DOS due only to the temperature and which can not be explained with the thermal expansion.

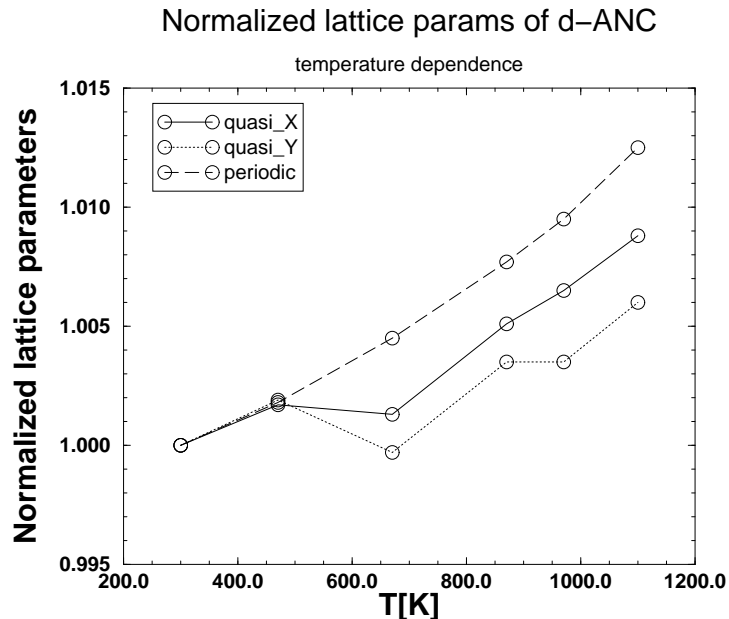


Figure 5.2: The normalized lattice parameters of d-AlNiCo (from F. Dugain et al). The plots show the lattice parameters at temperature $T=300\text{K}$, 470K , 670K , 870K , 970K and 1100K divided by the corresponding lattice parameter at 300K . The quasicrystal expand faster along the periodic direction than in the quasiperiodic plan. Notice the linear dependence for the periodic lattice parameter.

5.2 Vibrational entropy for o-Al-13Co₄, Al₉Co₂Ni and Al₃Ni

5.2.1 Introduction

While the Al-Co phase diagram in the concentration range of $x_{Co} \sim 0.25-0.30$ exhibits a sequence of stable complex phases like o-Al₁₃Co₄, m-Al₁₃Co₄, and Al₁₁Co₄, in the Al-Ni system near this composition there is a single and rather simple stable compound Al₃Ni. Energetic considerations using realistic pair potentials [Widom and Moriarty (1998)] suggest that:(i) the differences in cohesive energy between the simple structures like Al₃Ni, and the Al₁₃Co₄ structure is extremely small (of the order of few tens of a meV), (ii) a fractional occupancy of some Al sites is energetically favored over the full occupancy model, at least in o-Al₁₃Co₄ and its high temperature variant. The reported fractional Al occupancies, as well as the variety of structures occurring near the 25% of TM in Al-Ni and Al-Co phase diagrams and their subtle energetics balance suggests that the vibrational entropy, like for other phase diagrams [Nagel and Fultz (1997)], may play a role in the finite temperature stability. In this chapter, the role of the vibrational entropy in three phases (Al₃Ni, o-Al₁₃Co₄, and Al₉Co₂Ni) is investigated. These phases represent an increasing complexity of the structure. The Al₃Ni phase is a simple crystal with 16 atoms per unit cell, while Al₉Co₂Ni and o-Al₁₃Co₄ are two complex structures, the latter known to be an approximant to the d-AlNiCo quasicrystal. For this study we used the Phillips pair potentials which we truncated as before using an interaction cutoff radius $r_{cut}=7\text{\AA}$.

5.2.2 Energetics

The total energy E_T of a crystal is given by:

$$E_T = E_{coh} + E_{vib} \quad (5.6)$$

where E_{coh} is the cohesive energy, and E_{vib} is the vibrational energy.

Here E_{coh} is the sum over all pairs of the interatomic potentials in the pair potential approximation.

E_{vib} is defined in the harmonic approximation as follow:

$$E_{vib} = \int \hbar \left(e^{\frac{\hbar\omega}{k_B T}} - 1 \right)^{-1} + \frac{1}{2} D(\omega) d\omega \quad (5.7)$$

Where $D(\omega)$ is the vibrational density of states (DOS), and k_B is the Boltzman constant. The vibrational free energy is:

$$F_{vib} = E_{vib} + k_B \int \ln \left[2 \sinh \left[\frac{\hbar\omega}{2k_B T} \right] \right] D(\omega) d\omega \quad (5.8)$$

We calculate the DOS in the harmonic approximation, using the Al-Co pair potentials [Phillips et al (1994)]. Finally, the vibrational entropy is given by Eq.5.1.

5.2.3 Partial $\text{Al}_{13}\text{Co}_4$ occupation

As the pair potentials depend on the concentration x of the TM(Co/Ni), and as $x = 0.25$ in the case of Al_3Ni , and $\text{Al}_9\text{Co}_2\text{Ni}$, six Al atoms are removed in the $\text{Al}_{13}\text{Co}_4$ structure to have $x = 0.25$. To achieve this, the full occupancy structure is relaxed under the pair potential and the Al atom with the highest energy is removed. This procedure is repeated iteratively until we have $x = 0.25$. These calculations use experimental atomic volume calculated using the lattice parameters derived from experimental diffraction data.

5.2.4 Results

In the Table 5.1, we show the total energy E calculated at the experimental atomic volume Ω_{expe} obtained from the diffraction data.

	E[meV/atom]		
	T=0K	T=300K	T=1000K
Al_3Ni	7.28	11.85(4.57)	-301.32(-308.6)
$\text{Al}_9\text{Co}_2\text{Ni}$	15.70	18.07(2.37)	-304.0(-319.7)
$\text{Al}_{13}\text{Co}_4$	2.90	8.89(5.99)	-302.40(-305.3)

Table 5.1: The total energy ($E_{coh}+E_{vib}$) for the three phases, the vibrational contribution (E_{vib}) is shown between brackets.

At Ω_{expe} , the stable structure at room temperature is the partially occupied $\text{Al}_{13}\text{Co}_4$ structure with E by 2.96 meV/atom lower than for the Al_3Ni structure, and by 9.18 meV/atom lower than for the $\text{Al}_9\text{Co}_2\text{Ni}$ structure. However, the $\text{Al}_9\text{Co}_2\text{Ni}$ has the lowest vibrational term, and

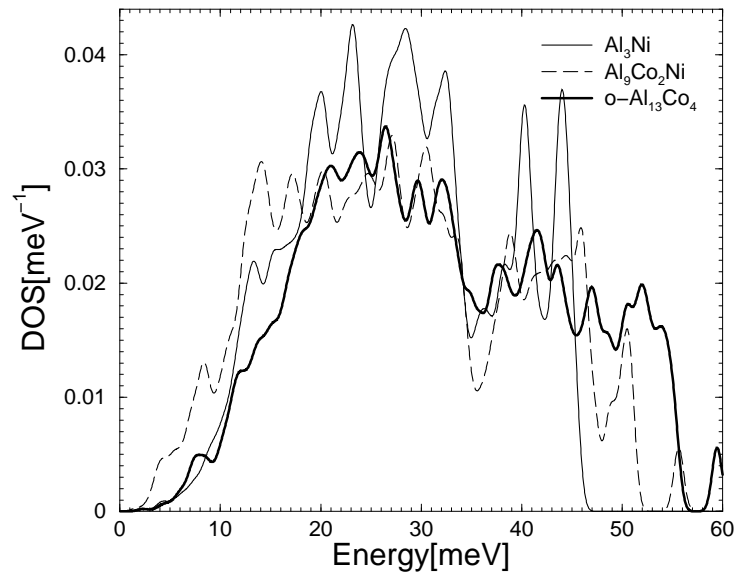


Figure 5.3: The VDOS of the three structures, we observe an excess VDOS at low energy for $\text{Al}_9\text{Co}_2\text{Ni}$.

at $T=1000\text{K}$, it becomes stable. Remarkably, in reality the binary variant of the $\text{Al}_9\text{Co}_2\text{Ni}$ structure – monoclinic $\text{Al}_{13}\text{Co}_4$ with the $\text{Al}_{13}\text{Os}_4$ type of structure - is a high-temperature metastable phase. Fig.5.3 shows the phonon DOS of the three phases. The $\text{Al}_9\text{Co}_2\text{Ni}$ DOS is higher at low frequencies. This plays an important role in the stability of this phase at high temperature against the two other phases, since the low frequencies have more weight in the formal expression of the vibrational entropy. These low frequency excess modes in the DOS can be explained by the presence of more localized states in this phase. Fig. 5.4 shows the three participation ratio. This figure shows that the excess phonon DOS of $\text{Al}_9\text{Co}_2\text{Ni}$ at low frequencies originates from low frequency modes with small participation ratio. These modes are rather quasilocalized modes according to the results of §2.4.5.

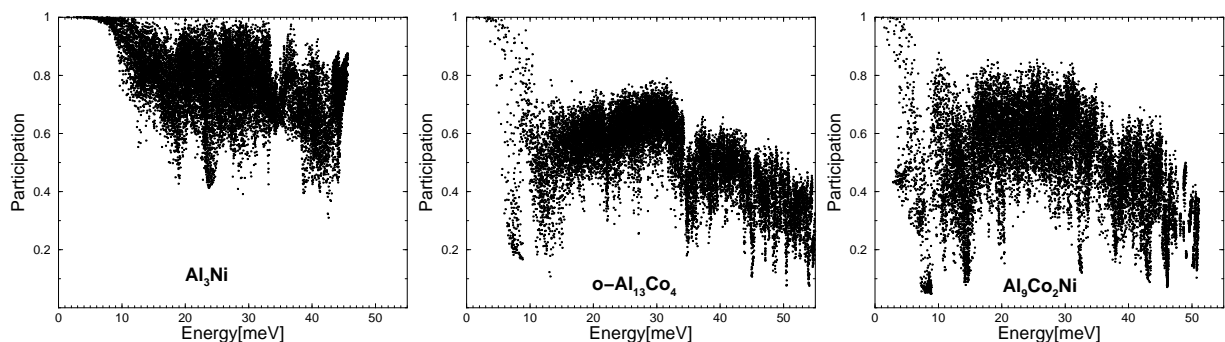


Figure 5.4: The participation ratio of the three structures. There are more states at low energy for $\text{Al}_9\text{Co}_2\text{Ni}$.

5.3 Conclusion

The vibrational contribution to the entropy was investigated in this chapter. We found an important anharmonic contribution for the d-AlNiCo system at high temperatures reaching $\approx 0.4k_B/\text{atom}$ at 1100K. We found also that this anharmonic behavior cannot be explained only by the thermal expansion, since there is a big discrepancy between the two relative vibrational entropies. Finally, we found that the vibrational entropy is responsible in our calculations for the stabilization of the $\text{Al}_9\text{Co}_2\text{Ni}$ over $\text{Al}_{13}\text{Co}_4$ and Al_3Ni at high temperature and this stabilization originates from the low frequency quasilocalized modes.

Chapter 6

Conclusion

The purpose of this work was to investigate the lattice dynamics in quasicrystals and its temperature dependence. This was achieved by using both, spring models and ab-initio pair potentials. The spring model proved to be a useful mean for such studies owing to its simplicity, and to the fact that it overcomes the instability problems introduced by realistic pair potentials. The spring model proved also to be useful as a link between the atomic structure and the significant features of the measured phonon DOS and for providing reliable partial phonon DOS. It was also more convenient to use the spring model for our frequency shift calculations owing to the imaginary eigenvectors caused by the instability problem encountered with pair potentials for some phases.

The generalized vibrational DOS (GVDOS) of d-ANC approximant model structure and o- $\text{Al}_{13}\text{Co}_4$ calculated using both sets of pair potentials and spring model explain the gross features of the experimentally determined GVDOS of the two phases: in particular, the maximum occurring between 25-30 meV is due to the partial DOS of the TM atom, while the broad Al band extends up to 60 meV. While for the μ -ZnMgY phase, the GVDOS calculated using a spring model reproduced the general features observed experimentally on the GVDOS of the icosahedral ZnMgY phase. The partial vibrational DOS showed that the peak at ≈ 17 meV and the small bumps at ≈ 24 meV are due to the vibrations of the Zn atoms, and the peak at ≈ 12 meV is due to the vibrations of the Y atoms. The broad Mg band extends up to 40 meV.

A comparison between the lattice dynamics in simple and complex structures showed that for simple crystalline structures, the phonon DOS exhibits a pronounced band-like structure, but the features are well resolved and at least few meV wide, due to the predominantly extended character of the eigenmodes. In contrast, the phonon DOS of the complex structures is dominated by broad features.

The structural complexity gives rise to localized states at the high energy limit of the phonon energy spectrum; but there are also some states with small participation ratio at low energies. For these modes, the displacement vector amplitudes do not decrease exponentially with the distance which shows that these modes are not localized, and we called them *quasi-localized* by analogy to the similar modes in glasses. These states at unusually low energies appear to be a distinct signature of the dynamics in the complex Al-Co (and presumably Al-TM) structures with a relationship to the quasicrystals. In the long-wavelength limit, the experimentally determined GVDOS of d-AlNiCo exhibits an excess phonon DOS, compared to

the Debye DOS calculated from the experimentally measured sound velocities in d-AlNiCo. We tentatively attribute the excess states to the aforementioned quasi-localized excitations.

In Chap.3, we developed a novel approach to the determination of the frequency shifts from the change in the phonon DOS as a function of the temperature. This method proved to be very accurate and provided us with the frequency shifts for a variety of quasicrystals which were used to derive the *Grüneisen parameter*.

The complex structures exhibit anomalously large and temperature dependent *Grüneisen parameter* at low frequencies. We showed in Chap.3 that this is due to the quasi-localized modes, which perform large shifts as a function of the temperature. The shifts of the quasi-localized modes give the main contribution to the anharmonic part of the vibrational entropy and as shown in Chap.4, would favor the stabilization of quasicrystals and related complex phases at high temperatures. This is in agreement with the experimental observation that quasicrystals are more stable at high temperatures.

Bibliography

- [1] Abe E, H. Takakura, A. Singh, and A.P. Tsai, *J. Alloys. and COmpounds* 283, 169(1999a)
- [2] Abe E, and A.P. Tsai, *Phys. Rev. Lett* 83, 4(1999b)753.
- [3] Ackerman D.A, A.C. Anderson, E.J. Cotts, J.N. Dobbs, W.M. MacDonald, and F.J. Walker, *Phys. Rev. B* 29,966 (1984)
- [4] Al-Lehyani I.H and M. Widom, accepted in *Mat. Sci. Eng. A*.
- [5] Allen P.B, Feldman J.L, Fabian J, and Wooten F, *Phil. Mag. B* 79, 1715 (1999)
- [6] Anthony L, Okamoto J.K and Fultz B, *Phys.Rev.Lett.* 70,1128(1993)
- [7] Ashraff J.A, J.M. Luck, and R.B. Stinchcombe, *Phys. Rev. B* 41, 4314(1990).
- [8] Bakker H, *Philos. Mag.* A45,213(1982)
- [9] Bakker H and Tuijn C, *J. Phys. C*19,5585(1986)
- [10] Beeli C, Nissen H.U and Robadey J, *Phil. Mag. Lett.* 63(1991)87.
- [11] Bell R.J and Hibbins-Butler D.C, *J. Phys. C* 8, 787(1975).
- [12] Bert F, Bellessa G, Quivy A, and Calvayrac Y, *Phys. Rev. B* 61, 32(2000).
- [13] de Boissieu M, Boudard M, Bellisent R, Quilichini M, Hennion B, Currat R, Goldman A.I, and Janot C, *J. Phys.:Condens. Matt.* 5, 4945(1991).
- [14] de Boissieu M, Boudard M, Kycia S, Goldman A.I, Hennion B, Bellissent R, Quilichini M, Currat R and Janot C, in C. Janot and R. Mossery(eds.), *Proc. 5th Int. Conf. Quasicrystals*, (World Scientific, Singapore, 1995), p. 577.
- [15] Bianchi A.D, Felder E, Kenzelmann M, Chernikov A.D, and Ott H.R, in *Proceedings of the 6th Int. Conf. on Quasicrystals*, edited by S. Takeuchi and T. Fujiwara (World Scientific, Singapore, 1997), p. 471.
- [16] Bogdanoff P.D and Fultz B, *Phil. Mag. B* 79, 753(1999).
- [17] Bogdanoff P.D and Fultz B, *Phys. Rev: B* 65,(2002)
- [18] Booth C and Rowlinson J. S. *Trans. faraday Soc.* 51, 463(1955)
- [19] Boudard M, de Boissieu M, Kycia S, Goldman A.I, Hennion B, Bellisent R, Quilichini M, Currat R, and Janot C, *J. Phys: Cond. Matt.* 7, 7299(1995).
- [20] Brand R.A, Dianoux A.J, and Calvayrac Y, *Phys. Rev. B.* 62, 8849(2000)
- [21] Chernikov M. A, H.R. Ott, A. Bianchi, A. Migliori, and T.W. Darling, *Phys. Rev. Lett.* 80, 321(1998).
- [22] Chernikov A.A, Felder E, Bianchi A.D, Wälti C, Kenzelmann M, Ott H.R, Edagawa K, de Boissieu M, Janot C, Feuerbacher M, Tamura N and Urban K in *Proceedings of the 6th Int. Conf. on Quasicrystals*, edited by S. Takeuchi and T. Fujiwara (World Scientific, Singapore, 1997), p. 451.
- [23] Clark S.J and Ackland G.J, *Phys. Rev. B* 48, 10 899(1993)
- [24] Cockayne E and Widom M, *Phil. Mag. A* 77, 593(1998a).
- [25] Cockayne E and Widom M, *Phys. Rev. Lett.* 81, 598(1998b).
- [26] Döblinger M, Wittmann R, Gerthsen D, and Grushko B, *Mater. Sci. Engn. A* 294, 131 (2001)
- [27] Dugain F, Mihalkovič M, and Suck J.B, *Mat Sci and Eng A*226-228(1997)967.
- [28] Dugain F, de Boissieu M, Shibata K, Currat R, Sato T.J, Kortan A.R, Suck J.B, Hradil K, Frey F, and Tsai A.P, *Eur. Phys. J. B* 7, 513(1999).
- [29] Dugain F, private communication.
- [30] Ebalard S and Spaepen F, *J. Mater Res.* 5(1990)62.

- [31] Edagawa K, Ichihara M, Suzuki K, and Takeuchi S, *Phil. Mag. Lett.* 66, 19-25(1992)
- [32] Edagawa K and Suzuki K, *Phys. Rev. Lett* 85(8), 1674(2000)
- [33] Elhor H, Mihalkovič M, and Suck J.B, *J. Mater.Science&Engineer.* 294-296(2000)658
- [34] Elhor H, unpublished(1999).
- [35] Eriksson O, Wills J.M, and Wallace D.C, *Phys. Rev. B* 46,5221(1992) Fabian J, and Allen P.B, *Phys. Rev. Lett* 79,1885(1997)
- [36] Fultz B, Anthony L, Nagel L.J, *Phys. Rev. B.* 52,3315(1995)
- [37] Garbulski G.D and Ceder G, *Phys. Rev. B* 49, 6327(1994)
- [38] Goldman A.I, Stassis C, Bellissent R, Moudden H, Pyka N, and Gayle F.W, *Phys. Rev. B* 43, 8763(1991).
- [39] Goldman A.I, Stassis C, de Boissieu M, Currat R, Janot C, R. Bellissent, H. Moudden, and F.W. Gayle, *Phys. Rev. B* 45, 10280(1992).
- [40] Gotzmann, Strukturelle Untersuchungen aluminiumhaltiger Phasen mit pentagonalen und ikosaedrischen Clustern, Ph.D. thesis, Institut für Metallkunde der Universität Stuttgart, Max-Planck-Institut für Metallforschung Stuttgart, Stuttgart, Germany(1998).
- [41] Grin J, Burkhardt U, and Ellner M, *Zeitschrift für Kristallographie* 209, 479(1994).
- [42] Grin J, Burkhardt U, Ellner M and Peters K, *Journal of Alloys and Compounds* 206, 243(1994).
- [43] Grin Y, Peters P, Burkhardt U, Gotzmann K, and Ellner M, *Z. Kristallogr.* 213, 364(1998). Hafner J, and Krajc, J. *Phys.:Condens. Matter* 5,2489(1993a) Hafner J, and Krajc, *Europhys. Lett.* 21(1),31(1993b) Hafner J, Krajci M, and Mihalkovič, *Phys. Rev. Lett.* 76,2738(1996) Hafner J, Krajci M, Windisch M, J. N. *Cryst. Solids.* 192&193(1995)212
- [44] He L.X, Wu Y.K and Kuo K.H, *J. Mater. Sci. Lett.* 7(1988)1284.
- [45] Henly C.L, in *Quasicrystals: The state of the art*, edited by D.P. Di Vincenzo and P.J. Steinhardt (World Scientific, Singapore, 1991), p. 111.
- [46] Hiraga K, Lincoln F.J, and Sun W, *Mater. Trans.* 32, 308(1991)
- [47] Hiraga K, Sun W, and Yamamoto A, *Mater. Trans. Jpn Inst. Metals* 35, 657(1994).
- [48] Idziak S.H.J and Heiney P.A, *Phil. Mag.* A61(1990)819.
- [49] Janot C, and Dubois J.M, *J. Phys. F: Met. Phys.* 18 2303-2343(1988)
- [50] Janot C, *Quasicrystals. A Primer*(Clarendon Press, Oxford)(1992).
- [51] Janssen T, *Acta Crystallogr.* A42, 261-71(1986)
- [52] Janssen T, *Phys. Rep.* 168(1988)55-113
- [53] Janssen T, in *Quasicrystalline Materials*, edited by C. Janot and J.M. Dubois (World Scientific, Singapore, 1988), p.327.
- [54] Kittel C, *Introduction to Solid State Physics*, 6th ed. (Wiley, New York, 1986).
- [55] Krajčí M and Hafner J, *J. Non-Cryst. Sol.* 192 & 193, 338(1995).
- [56] Levine D, and Steinhardt P.J, *Phys. Rev. Lett.* 53, 2477(1984)
- [57] Levine D, and Steinhardt P.J, *Phys. Rev. B.* 34, 596-616(1986)
- [58] Li X.Z and Kuo K.H, *Phil. Mag. Lett.* 58(1988)167.
- [59] Li X.Z and Kuo K.H, in: *Proc. China-Japan Seminars on Quasicrystals*, eds. Kuo K.H, and Ninomiya T,(World Scientific, Singapore, 1991).
- [60] Liu Z, Zhang Z, Jiang Q, and Tian D, *J. Phys.: Condens. Matt.* 4, 6343(1992).
- [61] Los J, Janssen T, and Gähler F, *Int. J. Mod. Phys. B* 7, 1505(1993).
- [62] Los J, Janssen T, and Gähler F, *J. Phys. I (Paris)* 3, 107(1993).
- [63] Los J, Janssen T, and Gähler F, *J. Phys. I (Paris)* 3, 1431(1993).
- [64] Lubensky T.C, Ramaswamy S, and Toner J. *Phys. Rev. B* 32, 7444(1985)
- [65] K.G. Lyon, G.L. Salinger, and C.A. Swenson, *Phys. Rev. B* 19, 4231(1979)
- [66] Mathew A.D, Jones R.E and Dwyer V.M, *J. Phys. F*13, 581(1983)
- [67] McDonald D.L, *Acta Crystallogr.* 23, 185(1966).
- [68] Mihalkovič M, Dugain F, and Suck J.B, *J. Non-Cryst. Sol.* 205-207, 701(1996).
- [69] Mihalkovič M, Zhu W.J, Henley C.L, and Phillips R, *Phys. Rev. B* 53, 9021(1996b).

- [70] Mihalkovič M, Elhor H, and Suck J.B, *J.Mater.Science&Engineer.* 294-296(2000)654
- [71] Mihalkovič M, Elhor H, and Suck J.B, *Phys. Rev. B*, 2001, 63, 214301/1-214301/14.
- [72] Mohri T, Takizawa S and K.Terakura, *J. Phys. Condens. Matter* 5,1473(1993)
- [73] Moraitis G and Gautier F, *J. Phys F7*, 1421(1977)
- [74] Morgan G.J, White G.K, and Collins J.G, *Phil. Mag. B* 43, 1039(1981)
- [75] Moriarty J.A and Widom M, *Phys. Rev. B* 56, 7905(1997).
- [76] Nagel L.J, Anthony L and Fultz B, *Phil.Mag.Lett.* 72,421(1995)
- [77] Nagel L.J and Fultz B, *Phys. Rev. B*, 55, 2903(1997)
- [78] Niikura A, Tsai A.P, Inoue A, and Masumoto T, *Phil. Mag. Lett*, 69, 351(1994).
- [79] Niizeki K, *J. Phys. A:Math. Gen.* 22, 205(1997)
- [80] Odagaki T, and Nguyen D, *Phys. Rev. B* 33, 2184(1986)
- [81] Ohashi W, and Spaepen F, *Nature*, 330, 555(1987).
- [82] Pavlovitch A, and Kleman M, *J. Phys. A:Math. Gen.* 20, 687-702(1987).
- [83] Villars P, and Calvert L.D, *Pearson's Handbook of Crystallographic Data for Intermetallic Phases* (American Society for Metals, Materials Park, OH, 1991).
- [84] Penrose R. *Bull. Inst. Appl. Math.* 10 266(1974)
- [85] Phillips R, Zou J, Carlsson A.E, and Widom M, *Phys. Rev. B* 49, 9322(1994).
- [86] Quilichini M and Janssen T, *Rev. Mod. Phys.* 69, 227(1997).
- [87] Quilichini M, Heger G, Hennion B, Lefebvre S, and Qiuuy A, *J. Phys. (Paris)* 51, 1785(1990).
- [88] Ranganathan S, and Chattopadhyay K, *Phase Trans.* 16(1989)67.
- [89] Rabson D.A, Mermin N.D, Rokhsar D.S and Wright D.C, *Rev. Mod. Phys.* 63(1991)699. Rouija M, private communication.
- [90] Sanchez J.M, Stark J.P and Moruzzi L, *Phys. Rev. B* 44, 5411(1991)
- [91] Saunders G.A, Metcalfe R.D, Cutroni M, Frederico M, and Piccolo A, *Phys. Rev. B* 53, 5287(1996)
- [92] Shechtman D, Blech I, Gratias D, and Cahn J W. *Phys. Rev. Lett.* 53 1951(1984)
- [93] Socolar J.E.S, Lubensky T.C and Steinhardt P.J, *Phys. Rev. B* 34, 3345(1986)
- [94] Steinhardt P.J, Jeong H.C, Saitoh K, Tanaka M, Abe E, and Tsai A.P, *Nature* 396, 55 (1998).
- [95] Sterzel R, Hinkel C, Haas A, Langsdorf A, Bruls G, and Assmus W, *Europhys. Lett.* 49, 742(2000).
- [96] Steurer W and Kuo K.H, *Acta Crystallogr. B*46(1990)703.
- [97] Steurer W, *J. Phys.:Condens. Mater* 3 (1991)3397.
- [98] Steurer W, Haibach T, Zhang B, Kek S, and Lück R, *Acta Cryst. B* 49, 661(1993).
- [99] Suck J.B and Rudin H, *Topic in Applied Phys.* 53(ed: H. Beck and H.J. GüntherodtSpringer, Heidelberg 1983)p.216
- [100] Suck J.B et al, *Phys. Rev. Lett* 59(1987)102
- [101] Suck J.B, in in *Quasicrystalline Materials*, edited by C. Janot and J.M. Dubois (World Scientific, Singapore, 1986), p.337.
- [102] Suck J.B, in Hunklinger, W. Ludwig and G. Weis (eds.), *Phonons* 89, (World Scientific, Singapore, 1990), p. 397.
- [103] Suck J.B, *J. Non-Cryst. Solids*, 153-154(1993a) 573.
- [104] Suck J.B, *J. Non-Cryst. Solids*, 156-158(1993b) 872.
- [105] Suck J.B, in *Rapidly Quenched and Metastable Materials (supplement)*, edited by P. Duhaj, P. Mrafko, and P. Švec (Elsevier, Amsterdam, The Netherlands, 1997), p. 410.
- [106] Sugiyama K, Yasuda K, Ohsuna T, and Hiraga K, *Z. Kristallogr.* 213, 537(1998).
- [107] Tendeloo G. Van, Menon J, Singh A and Ranganathan S, *Phase Trans.* 16(1989)59.
- [108] Tsai A.P in: *Physical Properties of Quasicrystals*, Ed, Z. Stadnik, Springer Series in Solid-State Science 126,(Springer-Verlag Berlin Heidelberg,1999)p 5.
- [109] N. Vernier, G. Bellessa, B. Perrin, A. Zarembowitch, and M. de Boissieu, *Europhys. Lett.* 22, 187(1993).
- [110] White G.K, *Phys. Rev. Lett.* 34,204(1975)
- [111] White G.K, Collocott S.J, and Cook J.S, *Phys. Rev. B* 29, 4778(1984)

- [112] Widom M and Moriarty J.A, Phys. Rev. B 58, 8967(1998).
- [113] Windisch M, Hafner J, Krajčí M, and Mihalkovič M, Phys. Rev. B 49, 8701(1994).
- [114] Wojtowitz P.J and Kirkwood J.G, J. Chem. Phys. 33, 1299(1960)
- [115] Yamamoto A, and Isihara K.N, Acta Crystallogr. A44(1988)707.
- [116] Yamamoto A, Kato K, Shibuya T, and Takeuchi S, Phys. rev. Lett. 65(1990)1603.
- [117] Yamamoto K, Jono M, and Matsuo Y, J. Phys.: Condens. Matter 11,1015(1999).

List of Figures

1.1	example of the Penrose tiling.	3
1.2	The experimental GVDOS of d-AlNiCo measured at 300K, 670K, 970K and 1100K. The GVDOS shifts to the low energies at high temperatures.	5
2.1	(up):The rectangle-triangle (RT) model, a RT tiling decorated by atoms of the same type on all the vertices. (down): The defect model consisting on RT tiling in which some vacancies defects were introduced (black circles show atoms).	10
2.2	The VDOS of the two models: the two VDOS show a band like structure, with a gap for the defect model GVDOS at $\sim 22-23$ a.u. There is an extra intensity in the VDOS for the defect model at low frequencies (window at the top left).	11
2.3	The participation ratio of the two models, there are modes with low participation ratio at low energies for the defect model, while we find for this model a group of extended modes at high energy not present for the RT model.	11
2.4	top: two low energy modes for the RT model with $E \approx 5.63$ a.u and participation ratio $\approx 0.24-0.24$. Notice the rotations of the pentagons at the center of the decagons (the arrows show eigenvectors). bottom:Low energy mode ($E \approx 2.01$ a.u and the participation ratio ≈ 0.585) for the defect model. The atoms around the empty spaces introduced by the defects tend to the fill these spaces. Notice the tendency to rotate the pentagons	12
2.5	The participation ration of bigger approximant for the defect model. The participation of the extended modes at high energy observed in Fig. 2.3 decreases.	13
2.6	The distribution of the participation ratio: there are more localized modes for the RT model, this is due to the high frequency localized modes.	14
2.7	(left): Structure model for $Al_{13}Co_4$, projection on the XY plan with two layers (small circles present the atoms on the lower layer) separated by $\sim 0.4nm$. (right): Pentagonal bipyramidal cluster containing 16 aluminium and 7 Co atoms.	15
2.8	Left: model for the 2 nm diameter columnar cluster. The labels design the Wyckoff cites, there are 3 TM inequivalent positions, and 8 Al inequivalent positions. Right: a structural model for the d-AlNiCo phase, this model was produced by decorating the vertices of a golden rhombi with acute angles of $\gamma=72^\circ$ and an edge length of $a=198,0nm$, by columnar clusters.	16
2.9	The c-axis projection of the structure of (left) Zn_2Mg -Laves structure and (right) structure model for the i-ZnMgY, open circles indicate Zn, gray ones indicate Mg, and black ones indicate Y. The difference of the circle size indicates different positions on the c-axis. The numbers on the figure of the Zn_2Mg -Laves structure indicate the the Wyckoff positions.	17
2.10	top: o- $Al_{13}Co_4$ spring model: the interaction Co-Co is not important in this model (notice the small values for the Co-Co force constants) this is mainly due to the small number of the Co-Co first neighbors. For Al-Al and Al-Co interactions, the force constants have higher values but vanish rapidly, especially for Al-Al where the force constants have non zero values only up to 0.3 nm. middle: d-AlNiCo spring model: like for the $Al_{13}Co_4$ case, the Al-Al and Al-TM force constants vanish rapidly, the particularity for the d-ANC spring model is the high TM-TM force constants. For this structure, there are more TM-TM first neighbors than the Co-Co neighbors in the o- $Al_{13}Co_4$ structure. bottom: ZnMgY spring model: The Zn-Zn interactions dominate up to ~ 0.4 nm, while the much weaker Y-Y interaction do not vanish up to ~ 0.8 nm	18

2.11	top: the experimental and calculated GVDOS of o-Al ₁₃ Co ₄ . The experimental GVDOS is characterized by the maximum at $\hbar\omega \sim 25$ meV, and a broad band up to 60 meV. middle: the calculated GVDOS of d-AlNiCo (with two different resolutions), compared to the experimental one. There are two main features: a peak at ~ 23 meV, and a broad band up to 60 meV. bottom: the experimental GVDOS of the i-ZnMgY phase up to 40 meV, together with the calculated GVDOS for μ -ZnMgY phase with a high and a low resolutions (LR)	19
2.12	Top: total and partial VDOS of Al ₁₃ Co ₄ . The partial Al is broad and spiky, while the partial Co smooth except at high frequencies where it is slightly spiky, and has a maximum at $\hbar\omega \sim 25$ meV which is also the maximum of the Al ₁₃ Co ₄ GVDOS Middle: the calculated VDOS and the partial DOS of d-AlNiCo. The peak in the GVDOS is due to TM vibrations, while the broad band is due to Al. Bottom: Partial VDOS of the μ -ZnMgY and Zn ₂ Mg structures.	22
2.13	Wyckoff positions for the μ -ZnMgY model	23
2.14	The local VDOS for d-AlNiCo, There are 3 TM and 8 for Al corresponding to the inequivalent positions of these elements in the model.	24
2.15	Local VDOS for the Wyckoff sites for (left): MgZn ₂ -Laves, and (right): μ -ZnMgY. Notice the Zn(6) partial (right). The Zn(6) atoms sit at the center of distorted icosahedra with more Y neighbors.	24
2.16	Typical behavior of $ \vec{e} ^2$ with distance. Here are presented three modes from the d-AlNiCo spectrum. An extended mode (crosses, $\hbar\omega \approx 2.06$ meV), a “quasi-localized mode” (empty circles, $\hbar\omega \approx 8.4$ meV), and a localized mode (dark circles, $\hbar\omega \approx 54.4$ meV) with localized length $\zeta \approx 0.207nm$	26
2.17	Top: participation ratio of the full occupancy model of Al ₁₃ Co ₄ , there are low frequency localized modes at the positions where we have maxima in the Al partial VDOS. The participation ratio has a scattered character Middle: the participation ratio of d-AlCoNi. Most of the modes have a participation ratio with values between ~ 0.2 and 0.7 . At low frequencies, there are modes with very low participation ratio. Bottom: the participation ratio of the MgZn ₂ -Laves and μ -ZnMgY: notice the three groups of modes in the μ ZnMgY participation ratio figure, the positions of these modes coincide with the positions of the three peaks in the GVDOS of this structure.	27
2.18	distribution of the participation ratio	28
2.19	modes (3) in Fig. 2.17, ($\hbar\omega \sim 4$ meV, $P \sim 0.32$), vibration of TM only along the pseudodecagonal axis.	29
2.20	$\frac{C_{ph}}{T^3}$ and $\frac{C_D}{T^3}$ versus T for Al ₁₃ Co ₄ (left) and d-AlNiCo approximant(right). Notice teh extra C_{ph} relatively to C_D observed in both cases. This extra heat capacity is a consequence of the low energy extra VDOS.	30
2.21	The major contribution to lattice heat capacity C_{ph} at low temperatures comes from low energy excitation.	30
3.1	Structure of Al ₃ Ni (projection along z-axis) (a), Al ₅ Co ₂ (projection along 3-fold axis) (b), o-Al ₁₃ Co ₄ (pseudodecagonal axis) (c), Al ₉ Co ₂ Ni (pseudodecagonal axis) (d), decagonal cluster in the model of d-ANC approximant (e), the approximant model of the d-ANC (pseudodecagonal axis) (f). Dark circles are TM atoms, open circles Al. The radius of the circles scale with the atomic coordinate perpendicular to the plane.	35
3.2	Comparison of radial distribution functions at $x=0.25$ (Al ₉ Co ₂ Ni and Al ₃ Ni structures, left) and at $x \approx 0.30$ (d-AlNiCo model and Al ₅ Co ₂ , right). In the case of d-AlNiCo, the PDF was taken from the model relaxed under the SE potentials, in the other cases the structures are unrelaxed. In all cases they are convolved with a gaussian with $\sigma = 0.01$	36
3.3	(a):Radial distribution functions (convolved with gaussian with half-width $\sigma=0.01$ nm) and two sets of Al–Al pair potentials. The energy scale for the potentials is displayed on the right side. For the GPT potential, the structure is <i>fcc</i> Al, for the SE potential it is an amorphous phase resulting from MD annealing. (b) SE and GPT Al–Co and Co–Co pair potentials.	37
3.4	Phonon DOS of the Al ₅ Co ₂ , Al ₃ Ni, Al ₉ Co ₂ Ni, o-Al ₁₃ Co ₄ and of the d-ANC model for the two sets of potentials: SE (a), and GPT (b).	41
3.5	Partial Aluminum and TM phonon DOS: SE potentials (a) and GPT potentials (b).	42
3.6	Partial Fe phonon DOS in i-AiCuFe determined experimentally [Brand et al (2000)], and local phonon DOS on three different Co sites in d-ANC model. The labels of the Co sites are explained in Fig. 3.1(e).	43
3.7	(a):Experimentally determined GVDOS of Al ₇₀ Ni ₁₅ Co ₁₅ and calculated GVDOS of d-ANC approximant model and Al ₃ Ni crystal (SE potentials).(b):GVDOS of o-Al ₁₃ Co ₄ with full occupancy (102 atoms in the unit cell) and with 6 Al→vacancy substitutions for the two sets of the potentials. The data are compared to the experimentally determined phonon GVDOS of o-Al ₁₃ Co ₄ at $T=300$ K. The “adjusted” GVDOS was calculated at variant atomic volume for 102-atom model (SE potentials) and 96-atom model (GPT).	44

3.8	Participation ratio of d-ANC model and Al ₃ Ni structure (SE potentials). For clarity, $P(\omega)$ is calculated for Γ -point only (d-ANC) and for 12 k -points (Al ₃ Ni) (plus symbols). For the low-energy part of Al ₃ Ni, $P(\omega)$ is shown as dots for a densely sampled Brillouin zone. The inset shows the corresponding phonon DOS. The parabolas below the DOS curves marked by arrows are the corresponding “Debye DOS” calculated from the sound velocities v_s	46
3.9	Phase quotient of d-ANC model (dots) and Al ₃ Ni structure (plus symbols) for SE potentials.	47
3.10	Temperature dependence of the partial Al debye–Waller factor obtained from molecular dynamics cooling runs from T=300.K down to 50 K(symblos)(using SE Potentials). The classical harmonic approximation of the phonon Debye–Waller factor is shown as lines.	49
3.11	Atomic density map of d-ANC model from MD annealing at $T=1000$ K, projected along the pseudo-decagonal axis (SE potentials, 500 samples). Large circles mark idealized positions of the Co atoms.	50
4.1	Experimental GVDOS at three different temperatures for d-AlNiCo and i-AlPdMn, there is a shift toward low frequencies at high temperatures[Suck et al, 1997; Dugain et al,1997].	54
4.2	Top(a): VDOS of the trial model calculated at two different volumes (solid and dashed line). Bottom(b): frequency shifts calculated for each eigenfrequency at the two volumes(points) and by the Monte Carlo technique(solid line).	55
4.3	(left): The reconstructed VDOS as function of temperature. (right): The relative frequency shifts.	56
4.4	Grüneisen parameter calculated from the frequency shifts using the experimental GVDOS for d-AlNiCo and d-AlCuCo.	57
4.5	Participation ratio of Al ₁₃ Co ₄ and Al ₃ Ni at V_1 obtained by using pair potential.	59
4.6	top: Grüneisen parameter calculated from the eigenfrequencies using the pair potentials. The negative values observed at V_1 calculations are caused by the structural instability under the pair potentials which is due to the peculiar shape of the Al-Al first neighbors interactions, and could also be due to the non inclusion of the many body terms in the potential energy. bottom: Grüneisen parameter calculated from the eigenfrequencies using a spring model.	60
4.7	left: Grüneisen parameter versus participation ration calculated from the eigenfrequencies using the pair potentials and at volume V_2 . right: Grüneisen parameter versus participation ratio calculated separately for each eigenmode using the spring model and at the volume V_2	61
5.1	Anharmonic entropy contribution. Triangles are the anharmonic entropy contribution calculated using the recovered phonon DOS of the previous chapter. Circles are the anharmonic contribution calculated using the spring model of the d-AlNiCo structure at volumes given by the experimental thermal expansion	64
5.2	The normalized lattice parameters of d-AlNiCo (from F. Dugain et al). The plots show the lattice parameters at temperature T=300K, 470K, 670K, 870K, 970K and 1100K divided by the corresponding lattice parameter at 300K. The quasicrystal expand faster along the periodic direction than in the quasiperiodic plan. Notice the linear dependence for the periodic lattice parameter.	65
5.3	The VDOS of the three structures, we observe an excess VDOS at low energy for Al ₉ Co ₂ Ni.	67
5.4	The participation ratio of the three structures. There are more states at low energy for Al ₉ Co ₂ Ni.	67

Curriculum Vitae

Personal data

First name: Hamid
 Family name: El hor
 Date of birth: Mars 16, 1968
 Place of birth: Rabat (Morocco)
 Nationality: Moroccan
 Marital status: Single

Education

1996-1997	Master of Science (Theoretical physics).	University of Rennes (France)
1995-1996	Maitrise en physiques,	University of Strasbourg (France)
1994-1995	Maitrise in physiques,	University of Agadir (Morocco)
1990-1992	DEUG en physiques-Chemie,	University of Agadir (Morocco)

Experience and skills

since Oct 2002	postdoctorate at the institute of theoretical physics (Non Linear dynamics), Münster/Germany
since Sep 2001	postdoctorate at the institute of theoretical physics (Non Linear dynamics), Augsburg/Germany
Feb 1998-July 2001	PhD student at the institute of physics (Materials research and liquids), Chemnitz/Germany
Apr-July 1997	Training at the Departement of atomic and molecular physics, Rennes/France
Feb-April 1996	Training at the Nuclear center Of Research of Strasbourg, Strasbourg/France

Publications

H. Elhor, M. Mihalkovič, and J.B. Suck:
Temperature dependence of the Phonon DOS in decagonal AlCoNi.
 Mater.Science&Engineer. 294-296(2000)658

M. Mihalkovič, H. Elhor, and J.B. Suck:
Low energy phonon excitations in decagonal quasicrystals AlCoNi and crystalline Al₁₃Co₄.
 J.Mater.Science&Engineer. 294-296(2000)654

M. Mihalkovič, H. Elhor, and J.B. Suck:
Lattice dynamics in Al-TM alloys via ab-initio pair potentials
 Phys. Rev. B, 2001, 63, 214301/1-214301/14.

Selbständigkeitserklärung

Hiermit erkläre ich, dass ich diese Arbeit selbstständig und nur mit angegeben Hilfsmitteln durchgeführt habe.

Chemnitz, im 1 September 2002